UNIVERSITÀ
DEGLI STUDI
DI PADOVA

DIPARTIMENTO
DI INGEGNERIA
DELL'INFORMAZIONE

DIPARTIMENTO DI INGEGNERIA DELL'INFORMAZIONE

CORSO DI LAUREA IN
BIOINGEGNERIA INDUSTRIALE

"FORMABILITY IMPROVEMENT OF 316 STAINLESS STEEL SHEETS BY SUB-ZERO MANUFACTURING"

Relatrice: Professoressa Stefania Bruschi

Laureando: Francesco Rocca (2018758)

Correlatrice: Ing. Rachele Bertolini
Correlatore: Ing. Enrico Simonetto

ANNO ACCADEMICO 2021–2022

Data di laurea 18/10/2022

Abstract

Austenitic Stainless steels such as AISI 316 are widely used for a great variety of applications that span from automotive to biomedical, to aerospace, to even the nuclear field. The importance to improve the formability of such materials, while maintaining at the same time low costs, can be very important in a lot of industrial settings. From these premises the work presented in this thesis starts.

The main goal of this dissertation is to evaluate the formability of AISI 316 stainless steel sheets by sub-zero manufacturing. AISI 316 is a type of stainless steel widely used in corrosive environments, largely utilized in the biomedical field, characterized by a low content of Carbon, high content of Chromium and Nickel, and by a presence of Manganese, Silicon, Phosphorus, Nitrogen, and Molybdenum.

Formability improvement was observed by sub-zero manufacturing, this was mainly evaluated by uniaxial tensile tests carried at different temperatures with the aid of an electricity generator, a climate chamber, and liquid nitrogen. The range of temperatures at which the samples were studied is 700°C, 300°C, 25°C, -50°C, and -100°C.

Subsequently, XRD evaluation was carried out to quantify the amount of the content of different phases of austenite and induced martensite by plastic deformation.

Then, corrosion tests were made to evaluate the corrosion resistance of the deformed stainless sheets to assess whether and how the temperature could have influenced this specific aspect of the material, which highly characterizes its uses.

Evaluations of the material crystalline structure were conducted by optical microscopy and SEM (Scanning Electron Microscope), both of which highlighted a biphasic crystalline structure with the presence of a martensitic phase in the sub-zero specimens.

With the aid of SEM, surface fractures of the specimen brought to failure at different temperatures were examined, highlighting differences.

Ultimately, a finite element model was introduced with LS-DYNA software in order to predict computationally the behavior of the material.

Gli acciai inossidabili austenitici come l'AISI 316 sono ampiamente utilizzati per una grande varietà di applicazioni che vanno dall'automotive al biomedico, all'aerospaziale, fino al campo nucleare. L'importanza di migliorare la formabilità di tali materiali, mantenendo allo stesso tempo costi contenuti, può essere molto importante in molti contesti industriali. Da queste premesse parte il lavoro presentato in questa tesi.
L'obiettivo principale di questa tesi è valutare la formabilità delle lamiere di acciaio inossidabile AISI 316 mediante lavorazioni sotto zero. L'AISI 316 è un tipo di acciaio inossidabile ampiamente utilizzato in ambienti corrosivi, largamente utilizzato in campo biomedico, caratterizzato da un basso contenuto di Carbonio, alto contenuto di Cromo e Nichel, e da una presenza di Manganese, Silicio, Fosforo, Azoto e Molibdeno.

Il miglioramento della formabilità è stata osservata post deformazione a temperature sotto zero, valutata principalmente da prove di trazione uniassiali eseguite a diverse temperature con l'ausilio di un generatore di elettricità, una camera climatica e azoto liquido. L'intervallo di temperature a cui sono stati studiati i campioni è 700°C, 300°C, 25°C, -50°C e -100°C.

Successivamente è stata effettuata una valutazione XRD per quantificare la quantità di contenuto delle diverse fasi di austenite e martensite indotta dalla deformazione plastica.
Successivamente sono state effettuate prove di corrosione per valutare la resistenza alla corrosione del materiale deformato per valutare se e come la temperatura possa aver influenzato questo specifico aspetto del materiale, che ne caratterizza fortemente gli impieghi.

Le valutazioni della struttura cristallina del materiale sono state condotte mediante microscopia ottica e SEM (Scanning Electron Microscope), entrambi i quali hanno evidenziato una struttura cristallina bifasica con presenza di una fase martensitica nei campioni sotto lo zero.
Con l'ausilio del SEM sono state esaminate le superfici di frattura del provino portato a rottura a diverse temperature, evidenziandone le differenze.

Infine, è stato introdotto un modello agli elementi finiti con il software LS-DYNA per prevedere computazionalmente il comportamento del materiale.

Index

....1
Abstract..3
1. State of the art – AISI 316..14
  1.1. Austenitic Stainless Steel..14
  1.2. AISI 316 – Properties & Applications..18
    1.2.1. AISI 316 in the biomedical field..21
    1.2.2. AISI 316 – Other applications..24
  1.3. Warm forming & Cold forming..25
  1.4. TRIP effect..28
  1.5. Stacking Fault Energy and its Correlation with Austenitic Stainless Steels..31
  1.6. Uniaxial Tensile Tests..34
  1.7. Objectives of the Thesis..39
Bibliography and Sitography..40
2. Instrumental Equipment..44
  2.1. MTS – 322..44
  2.2. Climate Chamber..46
    2.2.1. Liquid Nitrogen..47
    2.2.2. Electricity Generator..48
  2.3. Optical Microscope..52
  2.4. Electrolytic Equipment..53
  2.5. SEM..55
  2.6. XRD..56
  2.7. Vickers Hardness..56
  Bibliography and Sitography..59
3. Numerical Model..61
  3.1. LS-DYNA Software..61
  3.2. Specimen's Geometry and Mesh..63
  3.3. Structure of the Numerical Model..65
    3.3.1. Material Used..66
    3.3.2. Boundary Conditions..67
  3.4. Outputs..68
  Bibliography and Sitography..69
4. Uniaxial Tensile Tests Campaign – Valuations and Results..71
  4.1. Evaluation of the material at Room Temperature..72
    4.1.1. 0° Samples..73
    4.1.2. 90° Samples..74
    4.1.3. Comparison of 0° and 90° Samples..75
  4.2. Evaluation of the Material at Sub-Zero Temperatures..76

  - 4.2.1. Smooth Samples ... 79
  - 4.2.2. Notched Samples ... 81
  - 4.2.3. Shear Samples ... 85
- 4.3. Behavior’s Analysis of -100°C Smooth Samples ... 86
- 4.4. Evaluation of UTS and Strain at UTS ... 89
- 4.5. Optical Microscope ... 95
- 4.6. Vickers Hardness Test ... 98
- 4.7. SEM ... 101
  - 4.7.1. Normal Direction and Induced Martensite ... 101
  - 4.7.2. Surface Fracture ... 103
- 4.8. XRD ... 105
- 4.9. Corrosion Tests ... 107
- 5. Outcome of the Simulations ... 111
  - 5.1. Contour Plots ... 112
  - 5.2. True Stress-Strain Curves ... 115
  - 5.3. Load to Run Length Graphs ... 116
- 6. Conclusions ... 120

Figures' and Tables' Index

Figure 1.2.1: Austenite Structure in AISI 304 14

Figure 1.2.2: Composition Differences of Stainless Steels [3] 15

Table 1.2.1: Composition of the most common Austenitic Stainless Steels [3] 17

Table 1.3.1: Physical Properties of AISI 316 [4] 18

Table 1.3.2: Mechanical Properties of AISI 316 [4] 19

Figure 1.3.3: Hip Prostheses made in AISI 316L 22

Figure 1.3.4: Osteosynthesis Plates made in AISI 316L 23

Figure 1.3.5: Biomedical Structures made in AISI 316L 23

Figure 1.3.6: Marine Bollard Made in AISI 316 [5] 24

Figure 1.4.1: Typical Stress-Strain Curve 26

Figure 1.5.1: Typical Structure of Martensite [16] 28

Figure 1.5.2: TRIP Steels in The Automotive Industry [20] 30

Figure 1.6.1: Intrinsic Stacking Fault Energy (ISF) as a Function of Temperature [21] 32

Figure 1.6.2: Stacking Fault Energy (SFE) as a Function of Temperatures below 0°C [22] 32

Figure 1.7.1: Necking in Uniaxial Tensile Test 34

Figure 1.7.2: Differences between True and Engineering Stress-Strain Curves 36

Figure 1.7.3: Sample cut from a Metal Sheets - Deformations on the three Dimensions 37

Figure 1.7.4: Geometries of the Samples used 38

Figure 2.1.1: MTS-322 Load Frame 44

Table 2.1.1: Specifics of MTS-322 44

Figure 2.2.1: Climate Chamber disconnected from the MTS-322 47

Figure 2.2.2: Climate Chamber Connected to the MTS-322 47

Figure 2.2.3: Dewar Full of Liquid Nitrogen 48

Figure 2.2.5: Front of the Electricity Generator 49

Figure 2.2.6: Extension Used 49

Figure 2.2.7: Time-Temperature Function used to heat the Samples 51

Figure 2.3.1: Directions Observed [2] 52

Figure 2.3.2: Example of embedded samples 53

Figure 2.4.1: Electrolytic Equipment 53

Figure 2.5.1: SEM Used 55

Figure 2.5.2: Insertion of the embedded sample with copper tape in the SEM 55

Figure 2.7.1: Standard Procedure for Vickers Hardness Test [8] 57

Figure 2.7.2: Distances Required by UNI EN ISO 6507-1-2018 [10] 58

Figure 3.1.1: Typical FEM Object [2] 62

Figure 3.2.1: Mesh of Smooth Sample 63

Figure 3.2.2: Mesh of R5 Notched Sample 64

Figure 3.2.3: Mesh of Shear Sample 64

Figure 3.2.4: All Samples Meshed 65

Figure 3.3.1: True Stress-Strain Curve used to Define the material 66

Figure 3.3.2: Highlighted nodes where Boundary Conditions are applied 67

Table 4.0.1: Geometry properties for each Sample 71

Table 4.0.2: Strain Rate of the test [s-1] for each Geometry 71

Figure 4.1.1: Engineering Stress-Strain at Room Temperature – 0° Samples 73

Figure 4.1.2: True Stress-Strain at Room Temperature – 0° Samples 73

Figure 4.1.4: Engineering Stress-Strain at Room Temperature - 90° Samples 74

Figure 4.1.5: True Stress-Strain at Room Temperature - 90° Samples 75

Figure 4.1.5: UTS [MPa] for 0° and 90° Samples 75

Figure 4.1. 6: Strain at UTS for 0° and 90° Samples 76

Table 4.2.1: Collected Data from Tensile Tests at different Temperatures 78

Figure 4.2.1: 0° Samples - Engineering Stress-Strain 79

Figure 4.2.2: 90° Samples - Engineering Stress-Strain 80

Table 4.2.2: Geometrical Properties of Notched Samples 81

Figure 1.2.4: 90° Samples - Notched R2 82

Figure 4.2.3: 0° Samples - Notched R2 82

Figure 4.2.6: 90° Samples - Notched R5 83

Figure 4.2.5: 0° Samples - Notched R5 83

Figure 2.2.8: 90° Samples - Notched R10 84

Figure 4.2.7: 0° Samples - Notched R10..84

Figure 4.2.10: 90° Samples - Shear Specimens..85

Figure 4.2.9: 0° Samples - Shear Specimens..85

Figure 4.3.1: Different Strain-Stress Curves at -100°C 86

Figure 4.3.2: Nominal Stress and Volume Fraction of martensite vs nominal Strain [1] 87

Figure 4.4.1: UTS [MPa] at Different Temperatures – 0° Samples...89

Figure 4.4.3: Strain at UTS at Different Temperatures – 0° Samples..90

Figure 4.4.2: UTS [MPa] at Different Temperatures – 90° Samples..90

Figure 4.4.4: Strain at UTS at Different Temperatures – 90° Samples..91

Figure 4.4.6: UTS values Normalized - 90° Samples..92

Figure 4.4.5: UTS values Normalized - 0° Samples..92

Figure 4.4.8: Strain at UTS normalized - 90° Samples..93

Figure 4.4.7: Strain at UTS normalized - 0° Samples..93

Figure 4.5.1: "As Delivered" AISI 316 Normal Direction - 10% Oxalic Acid - Magnification 32X....95

Figure 4.5.3: Rolling Direction, Samples deformed to UTS - Beraha Attack – 1000X Magnification - a) 700°C, b) 300°C, c) 25°C, d) -50°C, e) -100°C Martensite highlighted in each image...........96

Figure 4.5.2: Normal Direction, Samples deformed to UTS - Beraha Attack – 1000X Magnification - a) 700°C, b) 300°C, c) 25°C, d) -50°C, e) -100°C Martensite highlighted in each image...........96

Figure 4.5.4: Transverse Direction, Samples deformed to UTS - Beraha Attack – 1000X Magnification - a) 700°C, b) 300°C, c) 25°C, d) -50°C, e) -100°C Martensite highlighted in each image..........97

Figure 4.6.1: Indentations for the Vickers Test - 20X Magnification a) Normal Direction, b) Rolling Direction, c) Transverse Direction..98

Table 4.6.1: Average Data of the Vickers Hardness Test with Standard Deviation............................99

Figure 4.6.2: Average Vickers Hardness in Comparison...99

Figure 4.6.3: Normalized Vickers Hardness in correlation to the "As Delivered" condition.............100

Figure 4.7.1: SEM Samples deformed to UTS - 1000X Magnification - ETD Detector - Beraha Attack. a) 700°C, b) 300°C, c) 25°C, d) -50°C, e) -100°C Martensite highlighted in each image..........101

Figure 4.7.2: SEM Samples deformed to UTS - 1000X Magnification - BSED Detector - Beraha Attack. a) 700°C, b) 300°C, c) 25°C, d) -50°C, e) -100°C...102

Figure 4.7.3: Steps of the MATLAB Script. a) Original SEM image, b) Same image after High-Pass Filter and Median Filter, c) After OTSU's Threshold..103

Figure 4.7.4: Martensite's Percentage in correlation to the Temperature..103

Figure 4.7.8: Surface Fracture at 700°C – ETD Detector. Different Magnifications: a) 250X, b) 500C, c) 1000X, d) 2000X 104

Figure 4.7.7: Surface Fracture at 25°C – ETD Detector. Different Magnifications: a) 250X, b) 500C, c) 1000X, d) 2000X 104

Figure 4.7.6: Surface Fracture at 300°C – ETD Detector. Different Magnifications: a) 250X, b) 500C, c) 1000X, d) 2000X 104

Figure 4.7.5: Surface Fracture at 700°C – ETD Detector. Different Magnifications: a) 250X, b) 500C, c) 1000X, d) 2000X 104

Figure 4.7.9: Surface Fracture at -100°C – ETD Detector. Different Magnifications: a) 250X, b) 500C, c) 1000X, d) 2000X 105

Figure 4.8.1: XRD Analysis of the Smooth Samples 105

Table 4.9.1: Results from Corrosion Test 107

Figure 4.9.1: Results of the Corrosion Test on Smooth Samples at different Temperatures 108

Figure 5.1.1: Contour Plots of Y-Stress for each geometry 112

Figure 5.1.2: Contour Plot of Y-Stress for Shear Geometry 113

Figure 5.1.3: Focus on R2 Notched Sample........ 113

Table 5.1.1: UTS [MPa] Values 114

Figure 5.2.1: Simulations and Tensile Test True Stress-Strain Curves in relation. a) Smooth Sample, b) R2 notched, c) R5 Notched, d) R10 Notched 115

Figure 5.3.1: Load to Run-Length graphs for each geometry. a) Smooth, b) R2 Notched, c) R5 Notched, d) R10 Notched........ 116

Figure 5.3.2: Load to Run-Length graph for the Shear geometry 116

Table 5.3.1: Values of Maximum Load reached by the LS-DYNA model and by Tensile Test........ 117

1. State of the art – AISI 316

1.1. Austenitic Stainless Steel

Austenitic Stainless Steels, such as AISI 316, are one of the five classes of Stainless Steels which are Austenitic, Martensitic, Ferritic, Duplex, and precipitation hardened. Specifically, Austenitic steels are characterized by a face-centered cubic (FCC) microcrystalline structure. Being one of the most used Stainless Steel, grade 316 is famous for its exceptional resistance to heat and corrosion. [1]

Austenite, which characterizes the microstructure of the austenitic family of steels, is a primary solid interstitial solution of carbon in γ-Iron. Austenite is anti-magnetic and stable only at high temperatures (723°C to 1495°C). Once heated, the cooling processes can transform Austenite into either Pearlite, Bainite, or Martensite. The FCC structure typical of the steels discussed here is achieved by adding enough Austenite stabilizing elements (austenite is not stable at room temperature) such as Nickel, Nitrogen, and Manganese. [2]

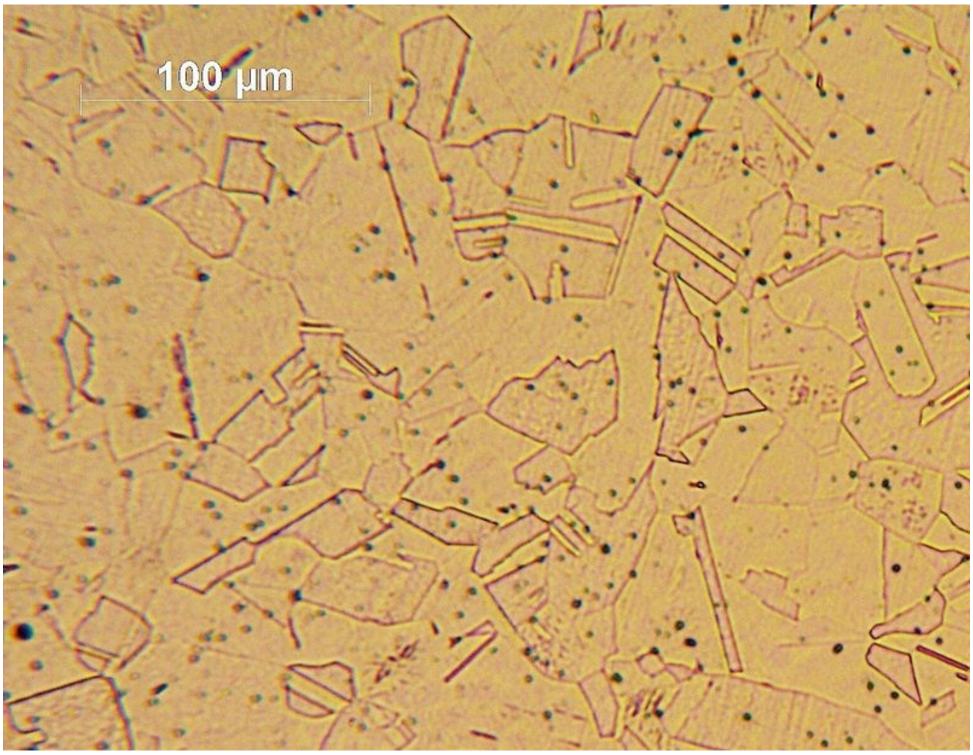

Figure 1.2.1: Austenite Structure in AISI 304

Stainless Steels can be grouped by either the AISI grade, which is defined by the American Iron and Steel Institute or the by European Standards, specifically by the Euronorm (EN) number. In this work, I will mainly refer to the AISI grade.

It's important to say that two families of austenitic stainless steels exist, the AISI 200 and 300 series. Specifically, the 300 series is characterized by the addition of mainly Nickel to stabilize Austenite, while the 200 series use Manganese and Nitrogen instead of Nickel, even though a small content of the latter can still be present. The 300 series is the one that is used the most in industrial settings. One particularity of this series is the possibility to characterize the stainless steel with a smaller content of Carbon, thus introducing the L variation, where L stands for "Low Carbon". For example, AISI 304 can become the AISI 304L, and AISI 316 can become the AISI 316L.

In the 300 series, a lot of different steels are present, such as the AISI 301, the AISI 304 (one of the most used), and the 304L, the AISI 303 where Sulphur is added to the alloy to improve machinability, the AISI 321 where small content of Titanium is added to increase corrosion resistance and AISI 316, the Austenitic stainless steel studied in the proposed analysis, in which a small amount of Molybdenum (2-3 %) is added, the AISI 316L (low carbon) and AISI 316Ti which has small content of Titanium.

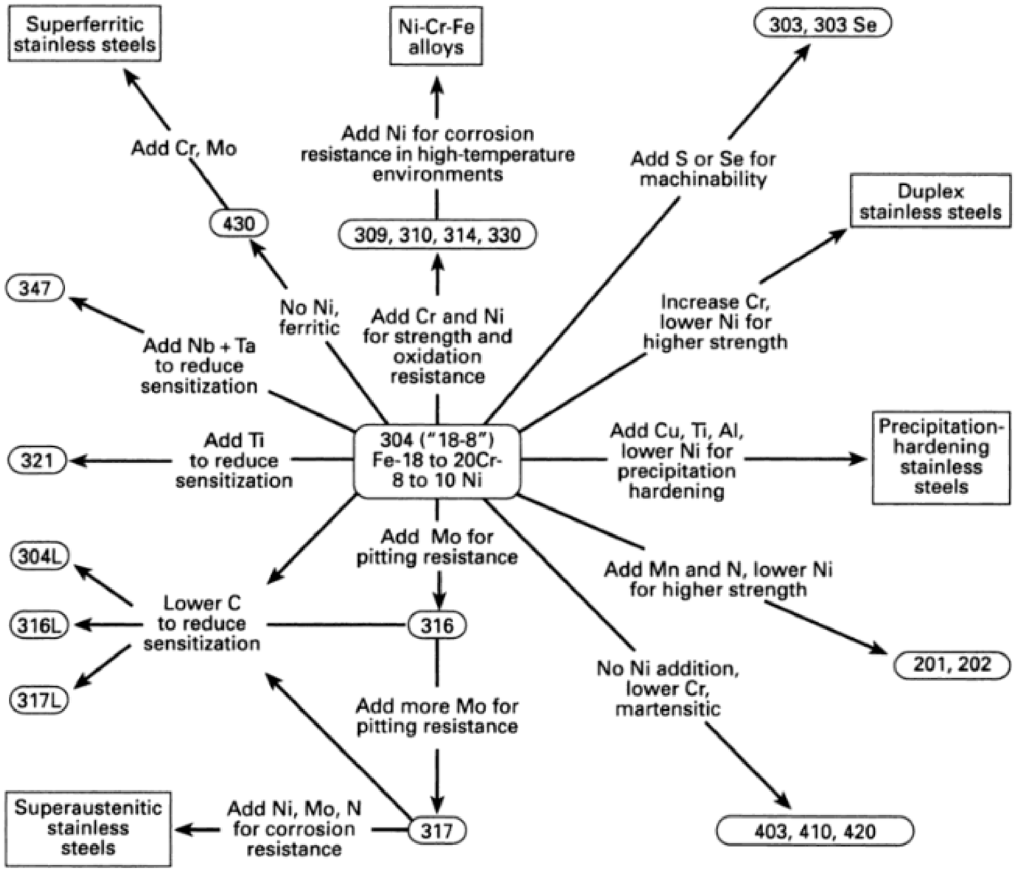

Figure 1.2.2: Composition Differences of Stainless Steels [3]

These types of steels are widely used in lots of industrial settings, for example:

- Medical Applications: Medical implants, hypodermic needles
- Automotive Applications: Fuel rails, deep drawn automotive parts, turbo parts
- Consumer Applications: Razor blade components, springs, cutters
- Aerospace Applications: Landing gears, helicopter applications, jet engine components
- Food Industry: Food preparation equipment
- Marine Applications: Coastal architectural paneling, railings, boat fittings
- Nuclear Applications: Cladding of fuel rods

This thesis focalizes on the 300 series, specifically on the AISI 316 Austenitic stainless steel.

UNS	**AISI**	**%C**	**%Cr**	**%Ni**	**%Mn**	**%Si**	**%P**	**%S**	**%N**
S20100	201	0.15	16-18	3.5-5.5	5.5-7.5	0.75-1	0.06	0.03	0.25
S20200	202	0.15	17-19	4-6	7.5-10.5	0.75-1	0.06	0.03	0.25
S20500	205	0.12-0.25	16.5-18	1-1.75	14-15.5	0.75-1	0.06	0.03	0.32-0.40
S30100	301	0.15	16-18	6-8	2	0.75-1	0.045	0.03	-
S30200	302	0.15	17-19	8-10	2	0.75	0.045	0.03	0.1
S30300	303	0.15	17-19	8-10	2	1	0.2	min 0.15	-
S30400	304	0.08	18-20	8-1.50	2	0.75	0.045	0.03	0.1
S30403	304L	0.03	18-20	8-12	2	0.75	0.045	0.03	0.1
S30500	305	0.12	17-19	10.5-13	2	0.75	0.045	0.03	-
S30800	308	0.08	19-21	10-12	2	1	0.045	0.03	-
S30900	309	0.2	22-24	12-15	2	1	0.045	0.03	-
S30908	309S	0.08	22-24	12-15	2	1	0.045	0.03	-
S31000	310	0.25	24-26	19-22	2	1.5	0.045	0.03	-
S31400	314	0.25	23-26	19-22	2	1.5-3.0	0.045	0.03	-
S31600	316	0.08	16-18	10-14	2	0.75	0.045	0.03	0.10
S31603	316L	0.03	16-18	10-14	2	0.75	0.045	0.03	0.10
S31651	316N	0.08	16-18	10-14	2	0.75	0.045	0.03	0.10-0.16
S31700	317	0.08	18-20	11-15	2	0.75	0.045	0.03	max 0.10
S31703	317L	0.03	18-20	11-15	2	0.75	0.045	0.03	max 0.10
S32100	321	0.08	17-19	9-12	2	0.75	0.045	0.03	max 0.10
S32900	329	0.08	23-28	2.5-5	2	0.75	0.04	0.03	-
S34700	347	0.08	17-19	9-13	2	0.75	0.045	0.03	-
S34800	348	0.08	17-19	9-13	2	0.75	0.045	0.03	-
S38400	384	0.08	15-17	17-19	2	1	0.045	0.03	-

Table 1.2.1: Composition of the most common Austenitic Stainless Steels [3]

1.2. AISI 316 – Properties & Applications

As stated before the austenitic stainless steel analyzed in this thesis is the AISI 316, also known by its Euronorm (EN) Number: 1.4401, by its EN designation: X5CrNiMo17-12-2 or by its Italian designation: Inox 18-8-3. It’s characterized by a low content of Carbon, generally 0,05%, with a fair amount of Chromium (16-18%), Nickel (11-14%), and Molybdenum (2-3%). It’s generally appreciated for its corrosion resistance, specifically to pitting.

The composition of grade 316 stainless steel is generally constituted of Iron, 16% to 18% of Chromium (Cr), 10% to 14% of Nickel (Ni), less than 0.08% of Carbon (C), 2% of Manganese (Mn), 0.75% of Silicon (Si), 0.045% of Phosphorus (P), 0.03% of Sulfur (S), 0.10% of Nitrogen (N), and 2% to 3% of Molybdenum (Mo) [4]. The presence of Molybdenum (Mo) makes the alloy stainless, particularly to the effects of NaCl or salt presents in seawater. Indeed, AISI 316 is also named “Marine Grade Stainless”, as it is widely used in the marine environment. Another characteristic of the AISI 316 is its nonmagnetic nature in its pristine form, which is valuable in those applications that require a non-magnetic metal such as in biomedical settings.

It’s important to underline that AISI 316 is usually known as “Surgical Grade Steel”, for its usability in the medical field. Its high content of chromium, which must be at least 13% of the composition, reacts with oxygen to form an oxide bond preventing the formation of rust. Grade 316 stainless steel presents also excellent weldability and good machinability.

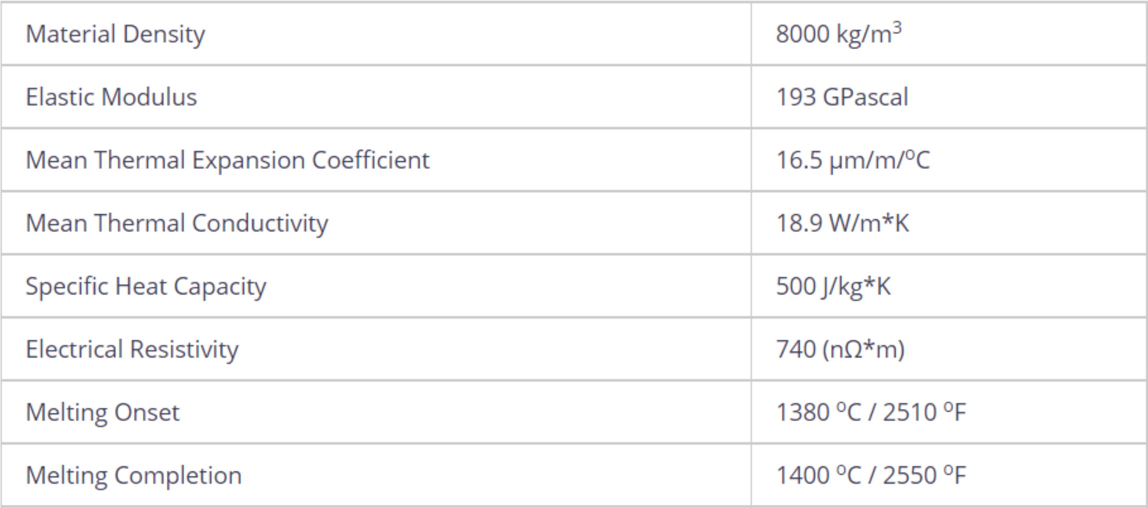

Material Density	8000 kg/m^3
Elastic Modulus	193 GPascal
Mean Thermal Expansion Coefficient	16.5 µm/m/^{o}C
Mean Thermal Conductivity	18.9 W/m*K
Specific Heat Capacity	500 J/kg*K
Electrical Resistivity	740 (nΩ*m)
Melting Onset	1380 ^{o}C / 2510 ^{o}F
Melting Completion	1400 ^{o}C / 2550 ^{o}F

Table 1.3.1: Physical Properties of AISI 316 [4]

AISI 316 has a material density of $8000 \frac{Kg}{m^3}$, a Young Modulus of 193 GPa, a max tensile strength of 580 MPa, and a Yield tensile strength of 290 MPa, which is the stress required to plastically deform the metal calculated at a plastic strain of 0.2%, with a melting temperature of 1400°C. These properties can drastically change in correlation to the temperature at which certain works are carried out. For example, the tensile strength values and the strain correlated to these strengths fall rapidly at temperatures above 400°C.

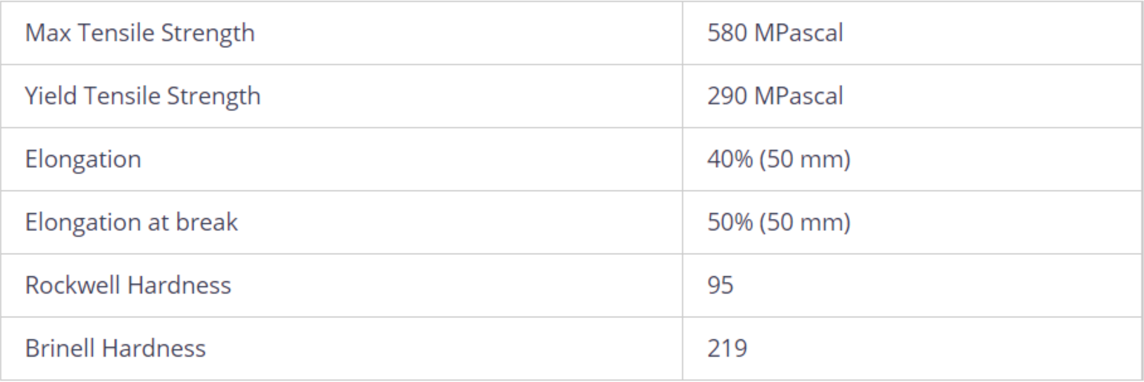

Max Tensile Strength	580 MPascal
Yield Tensile Strength	290 MPascal
Elongation	40% (50 mm)
Elongation at break	50% (50 mm)
Rockwell Hardness	95
Brinell Hardness	219

Table 1.3.2: Mechanical Properties of AISI 316 [4]

In order to enhance specific properties of this austenitic stainless steel a lot of differences in its composition can be implemented, specifically in the concentrations of its elements. A variety of different types of AISI 316 can be obtained, such as 316L, 316F, 316N, 316N, and 316Ti.

- 316L: Where the "L" stands for "Low Carbon". This type of 316 is characterized by a lower content of Carbon, usually less than 0.04%. The reduction in the content of Carbon is useful to reduce the precipitation of grain boundary carbide, which brings to sensitization and intergranular corrosion, thus increasing its corrosion resistance. It is used for handling paper pulp as well as in the production of rayon, rubber, textile bleaches, and in high-temperature industrial equipment. This particular type of AISI 316 is the most used in the biomedical field, but this aspect will be further analyzed in a following subchapter.

- 316F: where the "F" stands for "Free-Machining", it has a reduced content of Molybdenum, with an increased content of Phosphorus and Sulfur. It's used for parts of automated machines as well as surgical implants and pharmaceutical equipment.

- 316N: where the “N” stands for “High-Nitrogen”. This type of AISI 316 alloy has an increased content of Nitrogen, up to 0.16%, which enables the steel to have an increased resistance to corrosion and pitting, but also to achieve a higher strength. It is mainly used in accessories for chemical handling.

- 316Ti: this particular type of AISI 316 is stabilized by adding a certain amount of Titanium, from 5 times the content of carbon to a maximum of 0.7%, giving the stainless steel a better mechanical resistance to temperatures in the range of 600-900°C.

1.2.1. AISI 316 in the biomedical field

As previously said, the AISI 316 Stainless Steel is widely used in the biomedical field for a variety of applications. Its corrosion resistance and mechanical properties (high tensile strength for example) are useful in this particular setting [5,6,7]. Some of the applications for grade 316 include Medical Grade instruments such as scalpels and surgical forceps, pharmaceutical equipment, chemical processing and storage equipment, but also for some orthopedic implants even though as a temporary measure. It's important to say that in most developed countries more expensive materials such as Titanium alloy Ti6Al4V are preferred to AISI 316 for orthopedic implants, both for its greater mechanical properties and higher corrosion resistance. The main problem encountered in the biomedical field for grade 316 stainless steel is its high Nickel content, which compromises its biocompatibility. Biocompatibility, which is described as "*the ability of the material to perform with an appropriate host response in a specific application*" and "*Ability to be in contact with a living system without producing an adverse effect*" by IUPAC definition, it's one of the most important concepts in the study of new materials used in conjunction with biological structures.

The possibility of Nickel release from the material, due to both implant's wear and/or corrosion, can cause severe allergy issues and damages to the biological tissue near the implant, because Nickel (but also Chromium) is a carcinogen. In this meaning orthopedic implants made of AISI 316 steel are considered, in developed countries, more as a temporary measure to be replaced later with implants made of better materials or to be removed completely after healing, rather than a permanent implant. [8,9]

This grade of stainless steel is widely used as material for orthopedic implants in a lot of developing countries, where the costs associated with better materials both for corrosion resistance and mechanical properties cannot be adequately sustained. In this case, AISI 316 represents an adequate alternative.

As said before, even though grade 316 is commonly used and known as "surgical steel", it's the AISI 316L that is mostly used as a biomaterial. This type of AISI 316 is characterized by a smaller Carbon content usually smaller than 0.03%, to further increase its corrosion resistance by minimizing carbide precipitation. Its extremely high corrosion resistance makes it a better biomaterial than the grade 316 to be used in biomedical applications.

Specifically, the main uses of 316L in orthopedic implants are as hip prostheses, dental implant devices, osteosynthesis plates, and compression screws. [10]

Hip prostheses are used in hip replacement to relieve arthritis pain, or in some hip fractures. Hip replacement surgeries can be total or half replacement. A total hip replacement consists of replacing both the acetabulum, which is a part of the hip itself, and the femoral head. A variety of different biomaterials can be used for each different part of the hip articulation. For the femoral head stainless steels or titanium alloys can be used. In order to limit attrition and wear between the moving parts of the new articulation, ceramic and polymeric materials such as UHMWPE (ultra-height molecular weight polyethylene) can be used. This is because metallic on metallic interface can cause severe damages to the articulation itself due to the release of metallic ions.

Figure 1.3.3: Hip Prostheses made in AISI 316L

Osteosynthesis plates are used to reduce bone fractures, to re-align structures, and to bring together fractured parts of bones. Usually, they are used for long bones such as humeri, radii, ulnae, femora, tibiae, and fibulae. Different geometries can be used in order to adequately accommodate the plate most efficiently.

Different holes are made through the implant to make space for compression screws that hold the structures in place.

Figure 1.3.4: Osteosynthesis Plates made in AISI 316L

Even though titanium alloys are used for this kind of implants in developed countries, AISI 316L is widely used in developing countries as a less expensive material while maintaining both excellent mechanical properties and corrosion resistance.

Compressive screws are used in osteosynthesis to fixate and cement the implants in the right place. They are engineered to sustain high loads, thus needing a material with excellent mechanical properties such as AISI 316 and Titanium alloys.

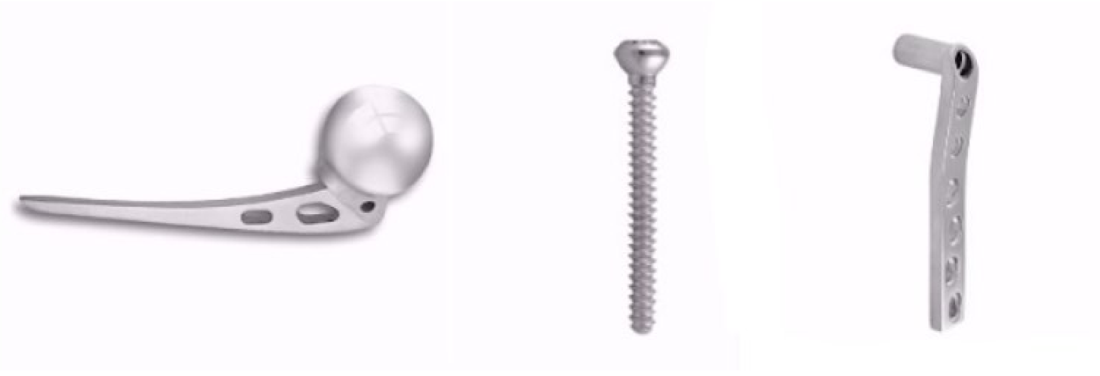

Figure 1.3.5: Biomedical Structures made in AISI 316L

1.2.2. AISI 316 – Other applications

Being one of the most common austenitic stainless steels in commerce, grade 316 stainless steel is not only used as a biomaterial or for biomedical applications, but it is also used in a lot of other different applications. Due to its high corrosion resistance also at high temperatures a lot of AISI 316 applications are set in high corrosive settings. For example, grade 316 is widely used in marine settings for coastal architectural paneling and coastal balustrading, but also for boat fittings and boat parts, marine bollards, nuts and bolts, where a chloride environment could cause severe damages to less corrosion resistance steels.

Figure 1.3.6: Marine Bollard Made in AISI 316 [5]

AISI 316 is also widely employed in the food industry to produce brewery, dairy, and food processing equipment, but also cutlery, flatware, and saucepans. Its applications span also for chemical and petrochemical equipment, laboratory benches, chemical transportation equipment, and heat exchangers, but also diaphragm pumps, tanks and storage vessels for corrosive liquids, and equipment for paper and mining applications. Furthermore, this austenitic stainless steel is also utilized in the automotive and aerospace industries, where AISI 316 is used for self-tapping screws, piston pumps, and fuel tanks, thanks also to its properties at high temperatures.

Grade 316 is also utilized in nuclear plants, where grade 316 steel is used to produce piping in BWR (Boiling Water Reactor) nuclear plants. [11]

1.3. Warm forming & Cold forming

With the term forming we refer to processes that aim to modify the shape of metallic components through mechanical deformation, specifically without removing or adding material, thus maintaining the mass of the deformed part unaffected. Forming processes can be categorized by the stresses applied to the component. For example compressive forming involves compressive loadings, while tensile forming involves, as the name suggests, tensile stresses. Examples of compressive forming can be rolling, extrusion, die forming, forging, and indenting. While examples of tensile forming can be stretching and expanding. Another possibility is to combine the two types of forming using both compressive and tensile loadings. Examples of these procedures are deep drawing, pulling through a die, and spinning. Besides compressive and tensile loadings, also different types of loads such as bending load and shearing load, can be induced in order to deform plastically metal parts, bending or shearing the components. One main aspect of forming processes is the fact that they can be carried out at different temperatures to enhance either formability, mechanical properties of the material itself or to maintain certain typical microcrystalline structures.

Three types of forming are considered regarding the temperature at which processes are carried out: hot, warm, and cold forming, deeply dependent on the recrystallization temperature of the material used. Specifically, hot working is carried out at temperatures above the recrystallization temperature of the metal, thus allowing the material to recrystallize during the deformation, preventing strain hardening, maintaining high ductility, low yield strength, and low hardness. Strain hardening is the strengthening of a metal induced by plastic deformation which occurs as a consequence of dislocation movements within the crystal structure of the deformed material. This effect can be either desired or undesired, depending on the final use of the workpiece. The effect of strain hardening can be seen by a stress-strain curve of the material.

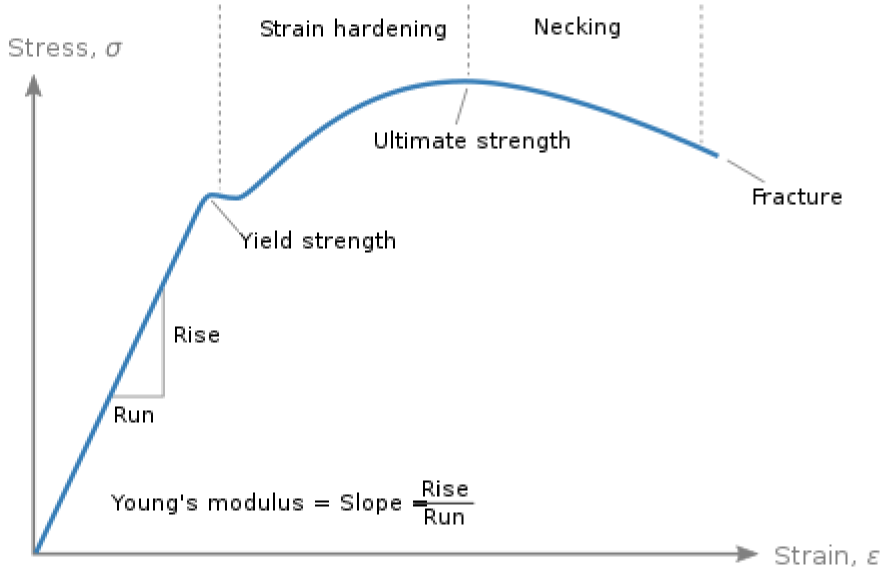

Figure 1.4.1: Typical Stress-Strain Curve

For a lot of metals hot forming is generally carried out at above at least 60% its melting temperature, with the upper limit that can vary from material to material. This type of forming has both advantages and disadvantages. The advantages can be decreasing the yield strength of the material increasing subsequently its formability, lowering energy and forces needed to deform it, reducing chemical inhomogeneities due to high temperatures and increasing ductility. Disadvantages can be the possibility of rapid oxidation due to reactions between the workpiece and atmosphere, less precise tolerances due to thermal contraction, modification in the grain structure and the high costs associated with heating.

Warm forming is characterized by temperatures that range from 30% to 60% of the melting temperature of the metal used. The upper temperature must however be always lower than the recrystallization temperature. The principal objective of warm working is to improve the plastic flow of the material while maintaining at the same time good formability and decreasing the possibility of spring back effect. The energy and force required to deform the workpiece appear to be higher than the ones used in hot forming but are generally lower than the ones needed in cold forming.

Cold forming consists of the processes carried out at temperatures lower than 30% of the melting one, generally at room temperature. This process allows the crystal grains to deform in the direction of the applied loads, provoking work hardening and anisotropic properties. The yield strength of the material increase, and so the force required to plastically deform the metal. Ductility consequently decreases, limiting the possibilities of achieving complex shapes and geometries. Cold working presents a lot of advantages, but also quite a few disadvantages. Some of the advantages found in cold forming are that no heating is required, limiting the costs and time of the process, the possibility to obtain a better surface finish and a better dimensional control, the fact that directional properties can be imparted into the material, better reproducibility, but also harder and stronger components are obtainable due to the strain hardening effect. Disadvantages are that the metal is harder to work, thus requiring higher forces, harder tools, heavier equipment, the limitation of deformation that can be obtained due to less ductility, the possibility of undesirable anisotropy and residual stresses in the final component.

One important aspect of forming, at every temperature, is the need for lubrication to limit friction between metal components. Even though a certain amount of friction is necessary to carry out the forming process, an excess of it could lead to a variety of problems. Lubricants used differs on the type of the material worked, the temperature at which the working occurs and the type of forming process. Lubricants can vary from oils (vegetable and mineral), soaps, graphite, water-based solutions, polymers, and wax. [12,13,14]

This thesis focuses on the possibility that cold forming at temperatures well below zero Celsius degrees can improve the formability and consequently the deformation at ultimate tensile strength, of the AISI 316.

1.4. TRIP effect

In order to properly evaluate the obtained results, a focus has to be done on the Transformation-Induced Plasticity effect (TRIP), which characterizes a lot of austenitic stainless steels such as AISI 316, also known as TRIP steels. These steels, capable of combining high strength and ductility, are characterized by a phase transformation in the material usually induced by an applied stress. Their microstructure consists of thermodynamically unstable Austenite that transforms into Martensite after plastic deformation. Specifically, the FCC γ Austenite transforms into BCC α' Martensite. This transformation enhances the strength of the stainless steel through the phenomenon of strain hardening, increasing its energy absorption capacity. [15]

It’s important to say that this transformation is highly dependent on temperature, stress, the composition of the material, strain rate, and deformation history. For example, the content of Carbon determines the strain at which the Austenite phase begins to transform into Martensite. The lower the content of Carbon, the lower the deformation needed to induce Austenite transformation. At higher Carbon levels the Austenite present in the steels is more stable, beginning to transform at higher strains.

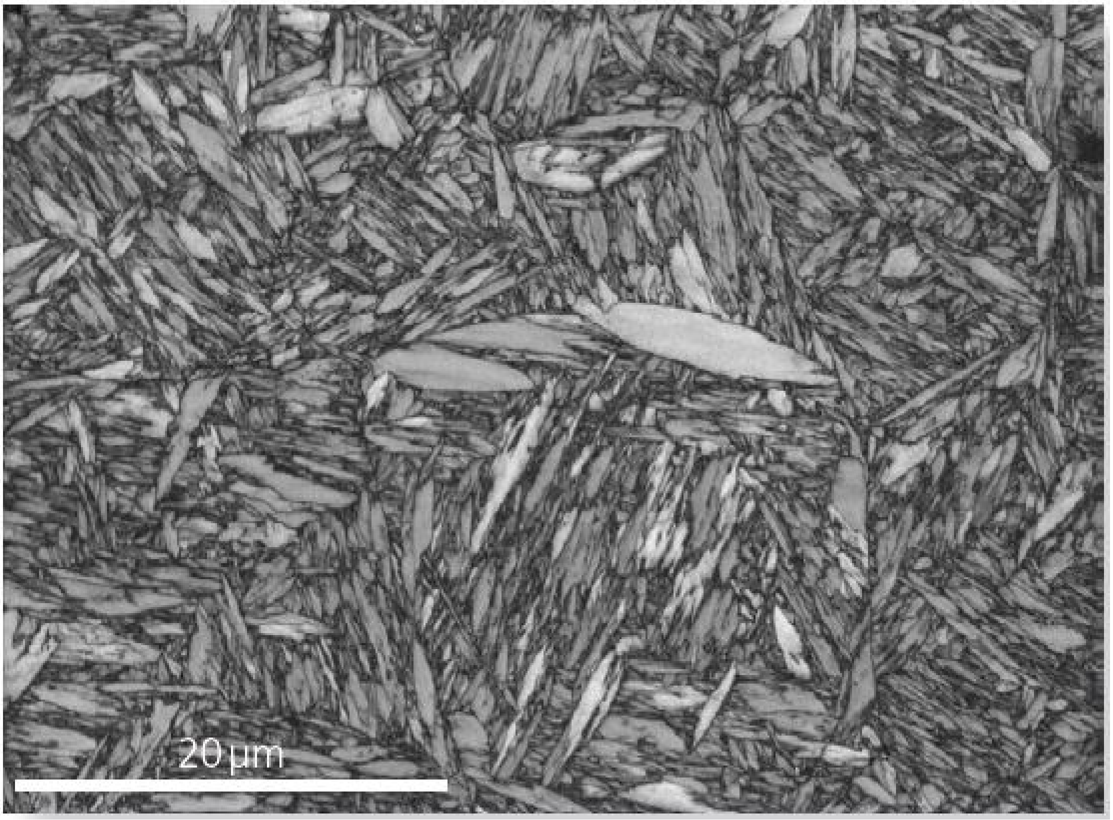

Figure 1.5.1: Typical Structure of Martensite [16]

Martensite is a steel crystalline structure, characterized by high hardness and a body-centered cubic structure. It's generally formed in carbon steels by rapid cooling (such as quenching) of Austenite structures in iron. Martensite has also a lower density than Austenite, causing a relative volume change, and it is characterized by needle-like microstructure. It is this particular microstructure that leads to a possible brittle behavior of the steel: too much Martensite creates brittle steels, too little creates soft materials.

The austenitic stability can be characterized by the Md_{30} Temperature, calculated by an empirical formula introduced by Angel et al. and extended by Nohara et al. [17,18], based on the chemical composition of the steel studied. Md_{30} Temperature is the temperature needed to gain 50% of induced martensite after 30% of elongation after tensile test. A high Md_{30} Temperature indicates a lower Austenite stability, thus indicating higher Martensite transformation. This empirical formula is used for a lot of different austenitic stainless steels, with differences in their compositions:

$Md_{30}(\mathrm{C}) = 551 - 462(\%\mathrm{C} \times \mathrm{N}\%) - 9.2\%\mathrm{Si} - 8.1\mathrm{Mn}\% - 13.7\mathrm{Cr}\% - 29.0(\mathrm{Ni}\% + \mathrm{Cu}\%) - 18.5\mathrm{Mo}\% - 68.0\mathrm{Nb}\%$

A modified version of the formula takes into consideration the grain size, expressed as:

$$Md_{30}{}^{GS} = Md_{30} - 1.42(\nu - 8.0)$$

where ν is ASTM grain size number, which is related to the number of grains that can be counted in 100X magnification. ASTM grain size number increases with the decrease of the grain size. Regarding AISI 316, the Md_{30} temperature was calculated as function of its composition. The Md_{30} Temperature was -105.7 °C, at which 50% of transformed Martensite is induced after 30% of elongation.

A quick way to evaluate the quantity and presence of Martensite in TRIP steels after deformation is by magnetic means, such as the Fischer Ferrite Test. As a matter of fact, Martensite is ferromagnetic. Another way to quantify the induced Martensite is by studying the microstructure via optical magnification or SEM.

TRIP steels have a lot of applications thanks to their high hardness and maintained ductility, high energy absorption capacity and fatigue strength. They are used in the automotive industry as structural and safety parts such as bumper cross members and B-pillar reinforcement. TRIP steels are also used for armor applications. Due to their uniform ductility they have high ballistic energy absorption, enhancing protection against projectiles while maintaining plate thickness. [19]

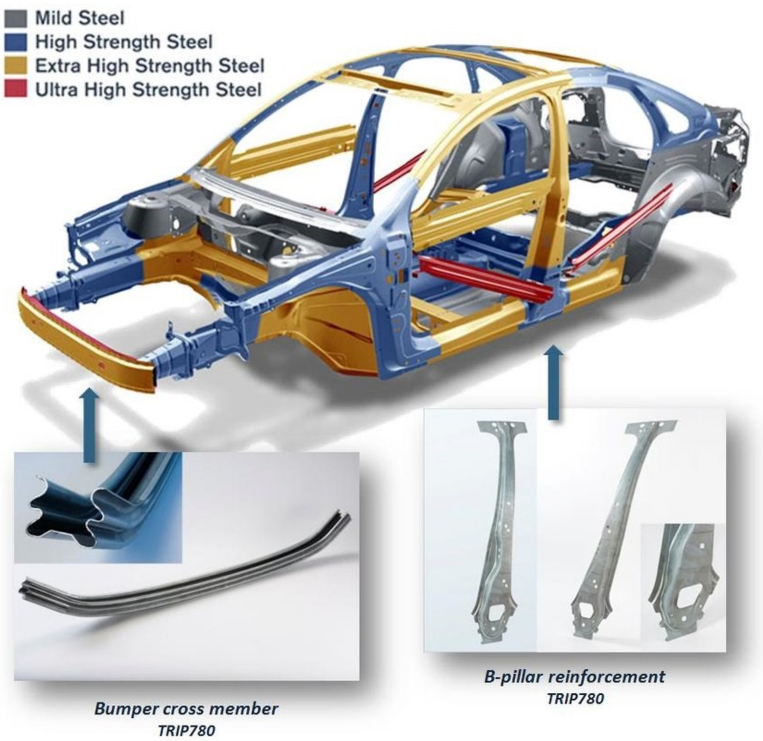

Figure 1.5.2: TRIP Steels in The Automotive Industry [20]

The TRIP effect appears to be influenced also by the Stacking Fault Energy (SFE) of the material, which will be discussed in the following subchapter.

1.5. Stacking Fault Energy and its Correlation with Austenitic Stainless Steels

The stacking fault energy is described as an intrinsic parameter depending on both composition and temperature, it is used usually to predict the deformation behavior of metals. A stacking fault is an irregularity, a planar defect, of the normal stacking sequence of atomic planes in a close-packed crystal structure. These interruptions in the crystalline planes carry energy, called stacking-fault energy. For example, in FCC metals the stacking sequence could be ABCABC, but if a planar defect is introduced it could create an irregularity such as ABCBCABC. These irregularities are the ones that carry energy, and this energy is called SFE.

It is important to say that in face-centered cubic (FCC) metals, SFE is used to calculate Martensitic transformation induced by plastic deformation. The influence that SFE has on temperature can be explained by the high stability of the FCC phase.

When the SFE is high the material can deform by dislocation glide or cross-slip, which is the process by which a dislocation moves from one slip plane to another due to stresses, allowing also non-planar movements. High SFE metals deform by glide of full dislocations, they do not need to change orientation to accommodate deformations. At high SFEs, because of small separation of partials, martensitic transformation and twin formation are difficult to obtain.

Lower SFE metals have difficulties with cross-slip because it requires the constriction of the wide Stacking Fault, which is not favorable energetically, thus decreasing the mobility of dislocations. Low SFE materials twin and create partial dislocations, their main mechanism of plastic deformation is by deformation twinning. Gliding and mechanical twinning increase the elongation to fracture, providing a high hardening rate. Low SFE indeed enhances exponential value of hardening, increasing at the same time the susceptibility to martensite formation due to plastic deformation. Molnàr et al. in "*Effect of temperature on the stacking fault energy and deformation behavior in 316L austenitic stainless steel*" found that the intrinsic Stacking Fault Energy of AISI 316L decreases linearly with the temperature, from 800°K (527°C) to 300K (27°C).

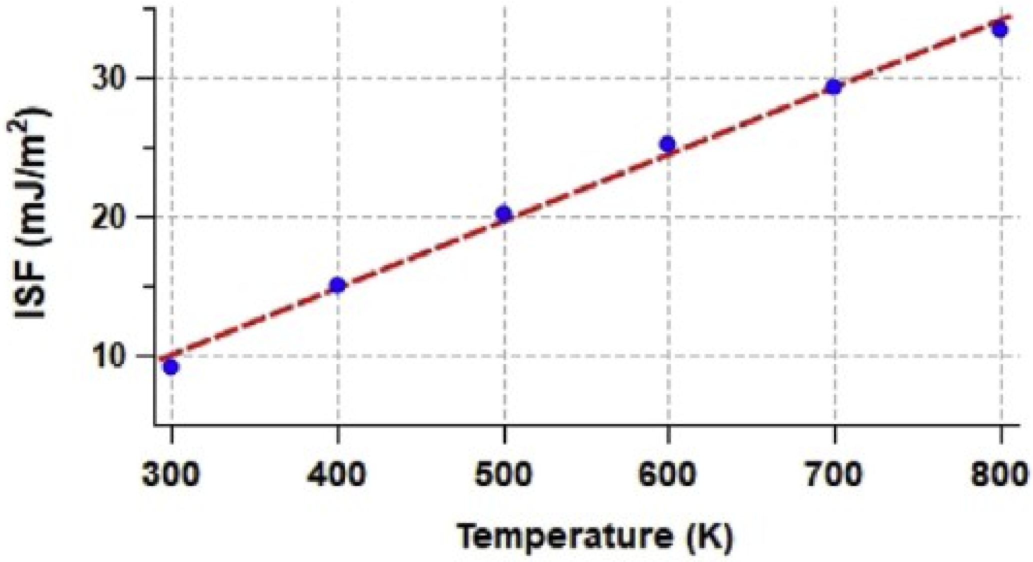

Figure 1.6.1: Intrinsic Stacking Fault Energy (ISF) as a Function of Temperature [21]

These results were also confirmed by S. Allain et al. in "*Correlations between the calculated stacking fault energy and the plasticity mechanisms in Fe–Mn–C alloys*", where Fe-Mn-C alloys were studied, composition correlated with austenitic Stainless steels. Also, the strain hardening component rapidly decreases at temperatures higher than 250°C (523 K). Similar results were also noticed in the outputs of the experimental processes carried out for this thesis. [21,22]

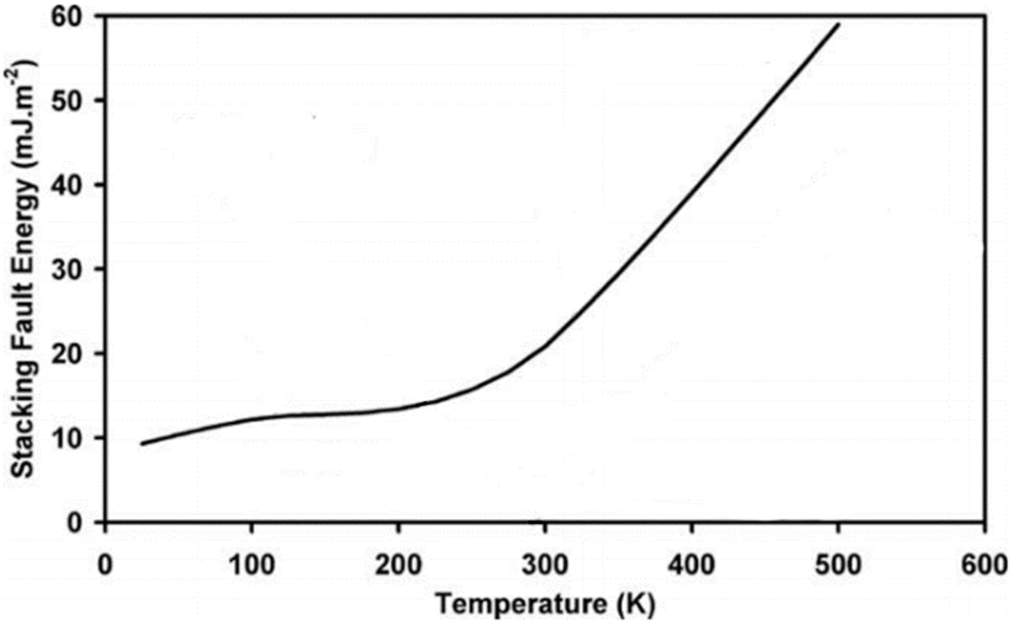

Figure 1.6.2: Stacking Fault Energy (SFE) as a Function of Temperatures below 0°C [22]

Stainless steels are characterized by a low Stacking-Fault Energy, less than 10 $\frac{mJ}{m^2}$ at room temperature.

Clearly there is a correlation between the TRIP effect seen in some austenitic stainless steels and their Stacking Fault Energy, which is deeply dependent on the temperature range at which processes are carried out.

1.6. Uniaxial Tensile Tests

In order to evaluate the mechanical properties at different temperatures of the AISI 316, uniaxial tensile tests were carried out. These types of tests have a lot of purposes, from predicting how a material will behave, to demonstrate whether a material is suited for a specific application, or just to provide data. A lot of different geometries can be used for the tensile tests, such as specimens with round cross-sections and threaded shoulders, or flat specimens designed for serrated grips. The main objective of tensile tests is to obtain a Stress-Strain curve, which can be important to evaluate a variety of mechanical properties such as the Yield Strength, Young's modulus, the ultimate tensile strength, the plastic strain at which failure of the sample is reached and so on.

The Stress and Strain are simply calculated by the initial and the final length of the specimen, by the tensile force applied, and by its nominal cross-section. Two types of stresses and strains can be calculated and acknowledged: an Engineering one and a True (or Real) one. The engineering Stress takes into consideration the nominal cross-section, which remains constant during the tests due to simplifications. The real Stress and Strain take in consideration the actual cross-section, which actually changes during the test due to the necking of the specimen. With the term Necking we refer to a deformation where the strains are localized in a region of the material tested by tensile load. This concentration of deformation results in a decrease of the cross-section area. This region is the one where also stress accumulates and where the sample will eventually break. [23]

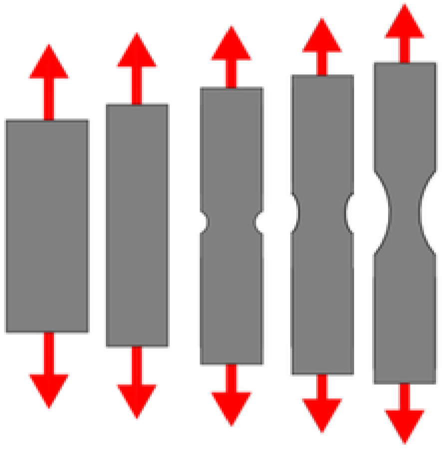

Figure 1.7.1: Necking in Uniaxial Tensile Test

The engineering Strain ε can be calculated as:

$$\varepsilon = \frac{L - L_0}{L_0}$$

where L is the final length of the specimen, while L_0 is the initial length. It's worth noting that the strain is characterized by being nondimensional, while the Engineering and Real Stresses are valued as pressures, commonly measured in Pascals.

The engineering Stress σ is calculated by:

$$\sigma = \frac{F_n}{A_0}$$

Where "F_n" is the force used to deform the specimen and "A_0" is the nominal cross-section, which is considered to remain constant throughout the test. This is actually a simplification: the nominal cross section varies during the tensile test due to necking.

As said before, True Stress and True Strain can be calculated too, taking into consideration the shrinking of the section of the specimen. Specifically, they are calculated by:

$$\sigma_t = \frac{F}{A}$$

$$\varepsilon_t = \int \frac{\delta L}{L}$$

Where "F" is the Force applied to the sample and "A" is the surface at a distinct instant of time.

The formula can become:

$$\varepsilon_t = \ln(1 + \varepsilon)$$

$$\sigma_t = \sigma\,(1 + \varepsilon)$$

Where ε and σ are the engineering Stress and Strain previously calculated.

It's important to say that in a tension test True Strain ε_t will be lower than its engineering counterpart ε, while true stress σ_t will be higher than the engineering one. [24]

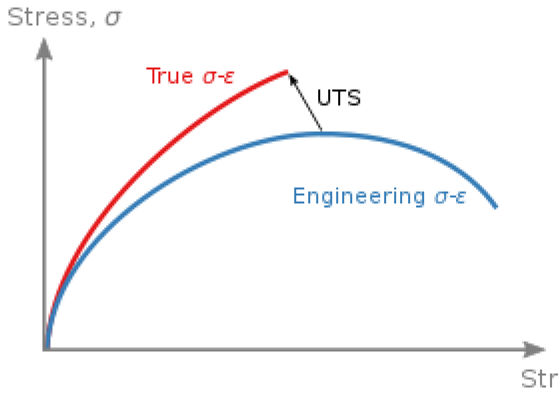

Figure 1.7.2: Differences between True and Engineering Stress-Strain Curves

This test can be carried out at different temperatures to evaluate the mechanical response of the material.

One way to evaluate the response is to bring the specimen to fracture, and obtain a complete stress-strain curve, which highlights the elastic and plastic phase of the metal until failure. From these tests, further evaluations can be done such as inspecting the fractured surface and its microstructure.

Another way to evaluate other aspects of the studied material is to bring the specimen to the highest point of the stress-strain curve, which is the point of Ultimate Tensile Strength. Once the material is carried to UTS, its microstructure can be evaluated by optical microscopy or by SEM.

The geometry of the specimens used for tensile tests can vary. For example, specimens can be cut with different angles from the same metal sheets, allowing to study the material more completely. Specimens can be cut by 0° to the Rolling Direction (RD) of the sheet, by 45°, and by 90°. Specimens can also have different geometries to evaluate the mechanical properties of the material itself. Workpieces used in tensile tests can be notched, having less amount of material in the middle part of the specimen, and the notch inserted can vary in radius.

The specimens used for this work were obtained by a sheet of AISI 316 Stainless Steel. Specimens with different geometries can be used in studying the material behavior with uniaxial tensile test, in order to evaluate different aspects. As said before, workpieces can be cut from the same metal sheets from different angles from the Rolling Direction (RD), also to study the anisotropy given to the material by the rolling of the sheet. Anisotropy is a property of materials that allows them to behave differently if solicited in different directions. The concept of Anisotropy is opposed to Isotropy, which describes materials that behave equally if solicited in different directions. Anisotropy can be induced in sheets of metals for example by cold rolling, where the sheets are passed through two or more rolls to decrease their thickness.

The Anisotropy Coefficient “R” is calculated by:

$$R = \frac{ln\,{}^{w_0}/_{w}}{ln\,{}^{t_0}/_{t}} = \frac{\varepsilon_w}{\varepsilon_t}$$

Where w_0 and t_0 are respectively the initial width and thickness of the specimen, so ε_w and ε_t represent the deformation in width and thickness. “R” can be calculated for each sample cut from the stainless sheet at three different angles from the Rolling direction. R_0 describes the anisotropy coefficient of the samples cut at 0° degrees, R_{45} is the coefficient for the specimens cut at 45°, and R_{90} for the specimens cut at 90°.

In order to rightly evaluate R, an average of the anisotropy coefficient is calculated as follows:

$$R_{avg} = \frac{R_0 + 2R_{45} + R_{90}}{4}$$

The R_{avg} for steels hot worked range from 0.8 to 1.0.

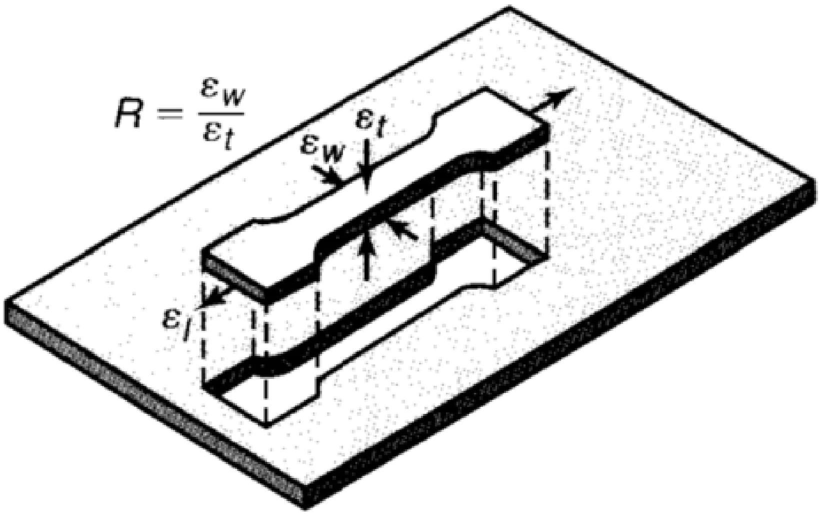

Figure 1.7.3: Sample cut from a Metal Sheets - Deformations on the three Dimensions

For this work 0°, 45° and 90° specimens were cut with different geometries from the same metal sheet. The direction and geometries used, as well as the tensile test itself, are standardized by the ASTM E8-04.

Smooth, Notched, and Shear specimens with 0° and 90° to the rolling direction were used. All the specimens have the same thickness of 1mm.

Smooth specimens are 165mm in length, 32mm in width, 65mm in actual length, and 12mm in actual width, characterized by wider parts at the extremities to facilitate the grip and by rectangular sections. They are designed to obtain uniform stresses in the central part.

Generally, the notch applied to samples can be U-Shaped, V-Shaped, or semi-circular. Notched specimens allow stress to concentrate in the notch itself, where cracks tend to appear. They are used to determine fracture mechanics and properties related to it such as fracture toughness. Three types of notched samples were used, respectively 2mm notch, 5mm notch, and 10mm notch of semi-circular shape. Even though the radius of the different notches is different, the actual width is maintained constant at 8mm. The total length and thickness are also maintained equal to the smooth specimen: respectively 165mm and 1mm. [25]

Ultimately, shear specimens were used characterized by a geometry studied to evaluate the simple shear that forms at the center of the specimen. This geometry is standardized by ASTM B83.

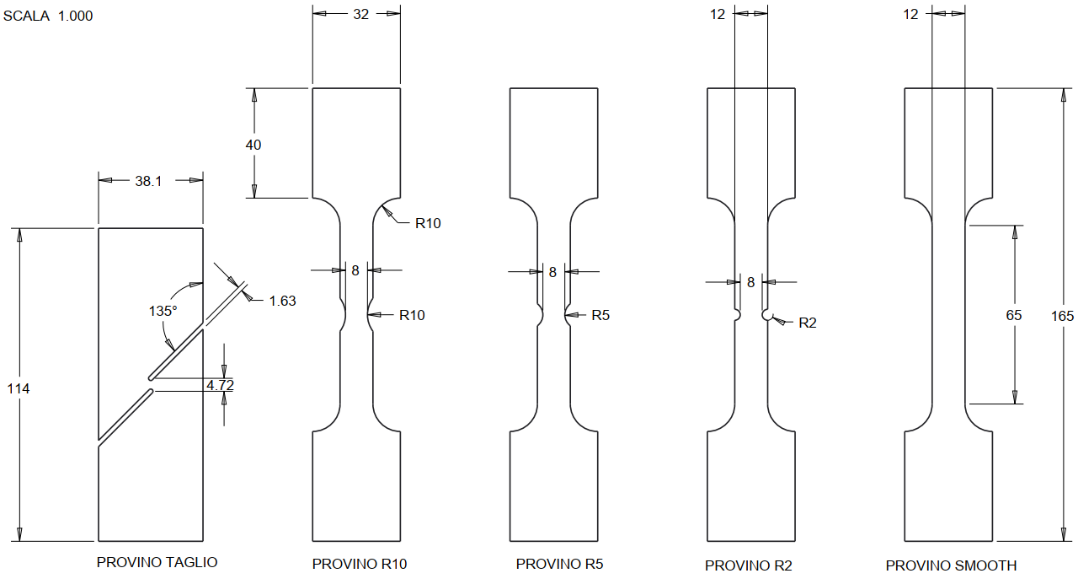

Figure 1.7.4: Geometries of the Samples used

1.7. Objectives of the Thesis

The main objective of this work was to study the improvement of formability of AISI 316 after cold forming, specifically at subzero temperatures. The improvement of formability was seen by studying the plastic deformation at the ultimate tensile strength, after uniaxial tensile tests were carried out at different temperatures on specimens with different geometries. A higher plastic strain at UTS was in fact seen in some of the specimens deformed at lower temperatures, specifically at -50°C and at -100°C, thus demonstrating that the formability of grade 316 steels can be enhanced by sub-zero working.

Subsequent studies were carried out in order to demonstrate the transformation of austenite in martensite due to the TRIP effect after plastic strain. The formation of the martensite phase was then correlated to the temperature at which the workpieces were deformed, thus creating a strong correlation between the TRIP effect and the working temperature. XRD tests were made to precisely quantify the amount of induced martensite, confirming the hypothesis introduced. Corrosion tests were carried in order to evaluate the corrosion resistance of the workpieces deformed at different temperatures. With all the information gathered, an evaluation on the possible applications for AISI 316 after cold forming at temperatures below zero were studied.

It’s important to say that also a numerical model of the uniaxial tensile tests was made with LS-DYNA software, which works with the finite element method (FEM), to facilitate the study of further tests. All the different geometries of the specimens used were introduced in the LS-DYNA, studying the differences between the reality and the numerical model.

Bibliography and Sitography

1. The International Nickel Company *"Standard Wrought Austenitic Stainless Steels*". Nickel Institute. (1974).
2. William F. Smith, "*Scienza e tecnologia dei materiali"*, 3ª ed., McGraw-Hill, (2008)
3. JOSEPH R. DAVIS, Stainless steels, ASM International, (1994)
4. *AISI 316 (1.4401, 1.4436, S31600) Stainless Steel:* https://www.makeitfrom.com/material-properties/AISI-316-S31600-Stainless-Steel
5. https://matmatch.com/learn/material/aisi-316-stainless-steel
6. https://bergsen.com/medical-surgical-stainless-steel
7. https://www.essentracomponents.com/en-gb/news/guides/what-is-surgical-steel-the-role-of-stainless-in-healthcare
8. Haudrechy, Pascale, et al. "*Nickel release from stainless steels.*" Contact Dermatitis 37.3 (1997): 113-117.
9. López DA, Durán A, Ceré SM. "*Electrochemical characterization of AISI 316L stainless steel in contact with simulated body fluid under infection conditions.*" J Mater Sci Mater Med. (2008)
10. Ali S, Irfan M, Niazi UM, Rani AMA, Rashedi A, Rahman S, Khan MKA, Alsaiari MA, Legutko S, Petrů J, Trefil A. "*Microstructure and Mechanical Properties of Modified 316L Stainless Steel Alloy for Biomedical Applications Using Powder Metallurgy.*" Materials (Basel). (2022)
11. Kowaka, Masamichi, Nagano, Hiroo, Yoshikawa, Kunihiko, Miura, Minoru, & Ota, Kunio. "*Development of nuclear grade type 316 stainless steel for BWR pipings."* Karyoku Genshiryoku Hatsuden, 32(12), 1303-1315. (1981).
12. *Reed-Hill R, Abbaschian R "Physical Metallurgy Principles (3rd ed.)". Boston: PWS-Kent Publishing. (1991). ISBN 978-0-534-92173-6*
13. Deringer-Ney, *"Cold Forming and Cold Heading Process*", (April 29, 2014)
14. https://thelibraryofmanufacturing.com/forming_basics
15. *"U. S. Steel - Automotive - TRIP Steels". Xnet3.uss.com. Archived from the original (2011*)
16. Oxford Instruments NanoAnalysis. "*Fast and Effective EBSD Mapping of Martensitic Stainless Steel." AZoM*. (2020, February 21). https://www.azom.com/article.aspx?ArticleID=13961.

17. Schneider, Matthias, and Mathias Liewald. "*Characterization of the austenitic stability of metastable austenitic stainless steel with regard to its formability.*" AIP Conference Proceedings. Vol. 1960. No. 1. AIP Publishing LLC, (2018).
18. Nohara, Kiyohiko, Yutaka Ono, and Nobuo Ohashi. "*Composition and grain size dependencies of strain-induced martensitic transformation in metastable austenitic stainless steels*." Tetsu-to-Hagané 63.5 (1977): 772-782.
19. Christodoulou, PETER I. "*Effect of retained austenite transformation on the fatigue behaviour of aluminum containing TRIP steels*." Doctoral dissertation, University of Thessaly, (2018).
20. Jo, Min Cheol, et al. "*Effect of tempering conditions on adiabatic shear banding during dynamic compression and ballistic impact tests of ultra-high-strength armor steel.*" Materials Science and Engineering*: A* 792 (2020): 139818.
21. Molnar, David, et al. "*Effect of temperature on the stacking fault energy and deformation behaviour in 316L austenitic stainless steel.*" Materials Science and Engineering*: A* 759 (2019): 490-497.
22. Allain, S., et al. "*Correlations between the calculated stacking fault energy and the plasticity mechanisms in Fe–Mn–C alloys.*" Materials Science and Engineering*: A* 387 (2004): 158-162.
23. Bridgman, Percy Williams. "*Studies in large plastic flow and fracture.*" Studies in Large Plastic Flow and Fracture. Harvard University Press, (2013).
24. Meyers, Marc André, and Krishan Kumar Chawla. "*Mechanical behavior of materials*." Cambridge university press, (2008).
25. Corten, Herbert Theodore, et al. "*Fracture Toughness, Proceedings of the 1971 National Symposium on Fracture Mechanics: Proceedings of the 1971 National Symposium on Fracture Mechanics",* University of Illinois, Urbana-Champaign, Ill., (1972).

2. Instrumental Equipment

In this Chapter, the equipment used will be analyzed. These apparatuses were used to determine both the mechanical behavior of AISI 316 at different temperatures and for post-deformation analysis.

2.1. MTS – 322

Figure 2.1.1: MTS-322 Load Frame

The MTS – 322 Load Frame is a servo-hydraulic press, produced by the MTS company. This hydraulic press is capable of both tensile and compressive tests at room temperature. It can achieve a nominal force of 50KN, with a run of 0-150 mm. The lower piston which is the part that moves and pulls or pushes the specimens can move at a velocity that spans from 0.01 mm/s to 150mm/s. Its frequency of acquisition is 6000Hz.

Nominal Force [KN]	Run Length [mm]	Piston's Speed [mm/s]	Acquisition's Rate [Hz]
50	0-150	0.01-150	6000

Table 2.1.1: Specifics of MTS-322

The software that runs the load frame can work in two different modes, “load” and “displacement” mode.

Displacement mode is the most common use: a certain movement is imposed on the lower piston, which moves at a velocity defined previously. When the lower piston has reached the defined displacement, it stops. This mode is efficiently used to do uniaxial tensile tests, both to bring the sample to failure but also to reach UTS.

Load mode requires imposition of a force, that can be tensile or compressive. When the imposed force is reached the lower piston maintains that force until required. This mode is useful when tensile tests at different temperatures are made. For example, when the specimen is heated by a climate chamber or by an electricity generator the heat expansion of the metal can push the pistons apart for the effects of tensile heat distortion. Similarly, for tests at sub-zero temperatures, the contraction of the material could bring the pistons together. For this kind of tests and others, load mode appears to be quite important. [1]

2.2. Climate Chamber

In order to do tensile tests in a certain range of temperatures the use of the climate chamber described in this subchapter is mandatory. This equipment, once connected to the electricity grid, is positioned inside and all around the load frame, permitting the application of two extensions firmly attached to the original grips of the MTS-322 that enter the climate chamber through holes situated on the bottom and the top of it. In this way, a thermally isolated environment is achieved. This chamber can be used for heating specimens with the same functionality as an oven, or for cooling by a freezing medium such as liquid nitrogen.

The climate chamber can reach temperatures as high as 300°C, and as low as -129°C. In order to know the temperature reached inside of it a thermostat is connected to the inside of the chamber. Once the climate chamber has reached the desired temperature is important to maintain that temperature for a certain amount of time, up to 10 or 15 minutes, to let the specimen applied to the grips to reach homogeneously the desired temperature. The first time that the chamber is turned on is advised to keep the temperature for a longer time to let the walls and ceilings inside to reach the desired temperature. This is important in order to lose minimum heat or Nitrogen when the door of the chamber opens for the change of the samples.

Figure 2.2.1: Climate Chamber disconnected from the MTS-322

Figure 2.2.2: Climate Chamber Connected to the MTS-322

2.2.1. Liquid Nitrogen

The medium used to cool down the specimen to sub-zero temperatures is liquid nitrogen. The temperatures required for the test were -50°C and -100°C. The boiling point of liquid nitrogen is -196°C, it is produced by fractional distillation of liquid air.

As a potentially dangerous fluid, thermal insulation is required when used. A Dewar flask is used to transport and for the usage of liquid nitrogen. A Dewar flask full of liquid nitrogen can be attached to the climate chamber. Once the temperature is defined on the control panel of the chamber, the liquid nitrogen begins to be pumped inside, thus refrigerating the enclosed environment. A full charge of liquid nitrogen is enough to carry out 9 to 10 uniaxial tensile tests at sub-zero temperatures.

Figure 2.2.3: Dewar Full of Liquid Nitrogen

.

2.2.2. Electricity Generator

One of the main objectives of this thesis was to evaluate the behavior of grade 316 Austenitic stainless steel at different temperatures. While the main focus was on the sub-zero temperatures and on the correlated formability, it was also important to investigate the performances of the steel at higher temperatures, higher than the ones reached by the climate chamber. For this reason an electricity generator was required to heat specimens through Joule effect. The electricity generator used can produce up to 6000 Ampere. Specifically, it's composed of 6 generators in series called modules, with the possibility to turn on each module singularly to control the current output. The number of modules used depends both on the material tested and on the temperature required. The temperature reached by the specimen is monitored by a pyrometer.

The electricity generator can work in two modes, with local control and with automatic control. The local control lets define the parameters desired (Voltage, Amperes etc.) directly from the generator, while automatic control allows to operate the generator from a computer. For the tests needed for this work automatic control was used.

Figure 2.2.5: Front of the Electricity Generator

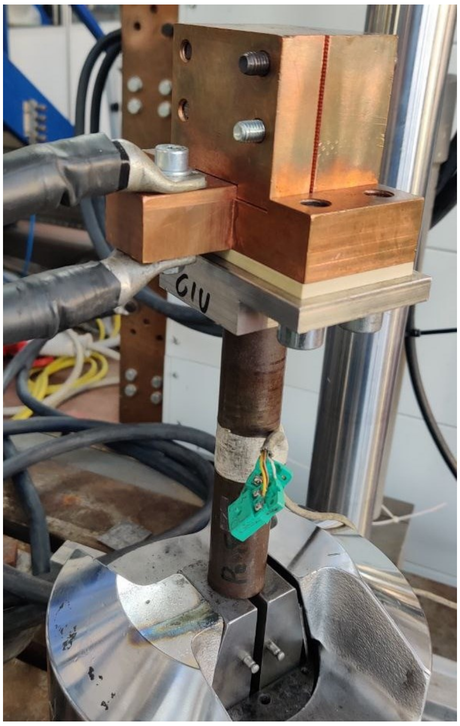

Figure 2.2.6: Extension Used

The automatic control is used to define a certain function (Time-Temperature) from the computer connected to the electricity generator which the generator follows to heat the specimen. The temperature reached is then maintained by the current generated for as long as the test requires, and then is slowly reduced to cool down the deformed or fractured sample.

The sample tested is heated by Joule Effect, also called Joule heating, which explains the process by which the passage of an electric current produces heat when it passes through a conductor. The electric field is produced by a potential difference, so by a voltage, supplied by the generator through the conductive specimen that creates an electric field that provides charged carriers of kinetic energy. The kinetic energy provided makes the ionized particles to collide, providing movement and oscillations, thus originating thermal energy. Joule Heating says that the power of the heating generated is equal to the resistance of the conductor multiplicated by the square of the current:

$$P = I^2 \times R$$

From this formulation, the current generated by the electricity generator successfully heat the specimen. In order to successfully let the current through the sample, specific extensions grips are used and applied to the MTS-332. These extensions are linked through two cables each, one positive and one negative, to the electricity generator. The extensions are characterized by an isolation element which separates the grips from the part actually attached to the load frame.

Because environmental differences (temperature, humidity, lights) can vary daily, the temperature of the sample and the current needed to heat the specimen, certain preparations are required. First of all the specimen is colored in the middle part in pitch black with a spray can. This is made in order to have a constant temperature monitored by the pyrometer which works on the base of a focused laser light. The laser of the pyrometer might be influenced by the reflective surface of the AISI 316 sample.

Because the output of the generator is measured in Volts, it is necessary to correlate the volts produced to the temperature assessed by the pyrometer. If the pyrometer is not used, it is not possible to define the temperature reached by the sample by just the volt output of the electricity generator. The pyrometer also gives input to the electricity generator itself. If the temperature seen by the pyrometer is less than the one required, the generator gives more current. On the contrary, if the pyrometer measures a higher temperature than the one required, the generator lows the output accordingly. This feedback permits to maintain a constant temperature when needed. As said before, a Time-Temperature function is imposed from a software to the electricity generator thanks to the automatic control. This function allows to raise the temperature of the sample, produced by Joule heating, gradually. Once the temperature required for the test is reached, it is maintained constant for a certain period of time, usually two minutes, to let the temperature of the sample to be homogenous. Then, the uniaxial tensile test is carried out. Once the specimen reaches fracture, the current produced by the generator can be closed.

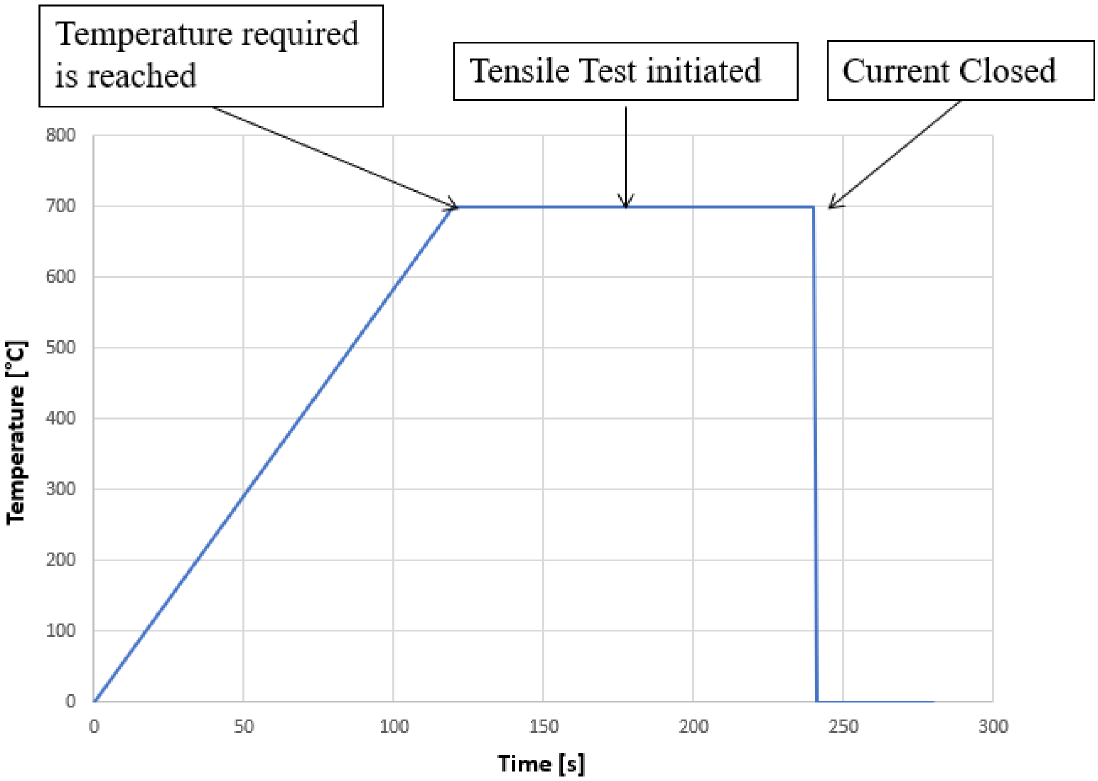

Figure 2.2.7: Time-Temperature Function used to heat the Samples

2.3. Optical Microscope

The optical microscope is a type of microscope that uses light and a series of lenses to magnify objects. In metallography it is used to see the microstructure of the metal. The microscope used for this thesis can obtain a magnification of 10X, 20X, 32X, 50X, 100X, and 200X. This type of magnification is enough to see clearly certain types of different phases typical of Austenitic Stainless Steels, present both before and after deformation.

Preparative steps need to be done to correctly see the microstructure of the material. First, small samples of the fractured or deformed specimen are cut. The specimen studied has 3 different directions that can be observed, a Normal Direction, a Transverse Direction, and a Rolling Direction, highlighted in Figure 2.3.1. Each direction has differences in the microstructure. From the specimen, three small parts are cut in order to be able to see at the same time all three different directions.

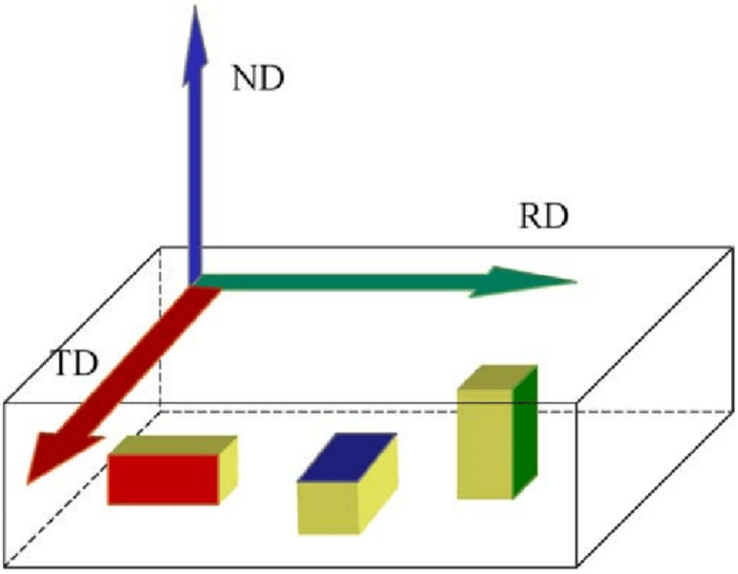

Figure 2.3.1: Directions Observed [2]

The cut samples are then incorporated into resin to facilitate the steps of smoothing and polishing the surface. The smoothed and polished pieces incorporated in resin are then attacked with chemical compounds to enhance their microstructure. Two chemical attacks were then performed on different samples in order to evaluate the Austenite and Martensite phases.

Figure 2.3.2: Example of embedded samples

The chemical solutions used were a solution of 10% of Oxalic Acid diluted in water, and Beraha. The second chemical attack, called Beraha, is used to enhance the martensitic phase of the AISI 316. The martensitic phase, as said before, is induced by plastic deformation, specifically at low temperatures. Beraha is a chemical solution composed of water, HCl, and potassium metabisulfate. [3]

2.4. Electrolytic Equipment

The electrolytic equipment is used to electrolytically attack the specimen. This type of etching requires a solution of an electrolyte, an anode, and a cathode. A source of electric current, in this case produced by the electrolytic equipment, is directly connected through the positive pole to the metal sample, which is submerged in the electrolyte solution. Depending on the electrolyte solution and the voltage used, the effect of the etching changes. [4]

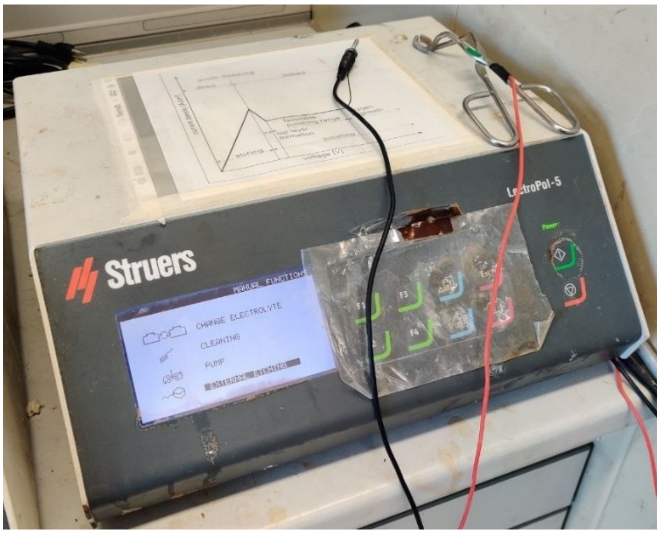

Figure 2.4.1: Electrolytic Equipment

The first chemical attack was made by electrolytically etching the surface for 50 seconds with 6 Volts. This attack enhances the austenitic structure of the AISI 316, it was used to evaluate the material in the “As Build” condition, so to study the material without previously applying any deformation or stresses to it.

2.5. SEM

While the optical microscope can obtain magnification to a maximum of 200X, it is not enough to see clearly specific phases and microstructure of stainless steel.

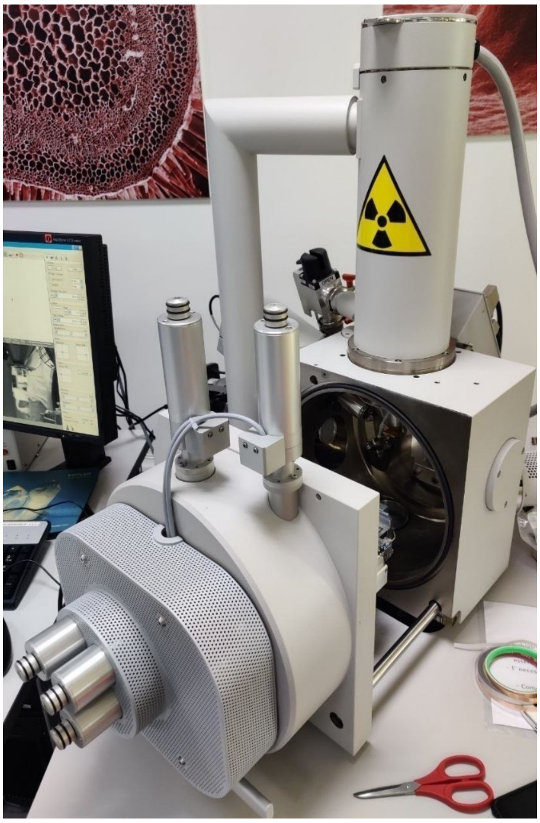

Figure 2.5.1: SEM Used

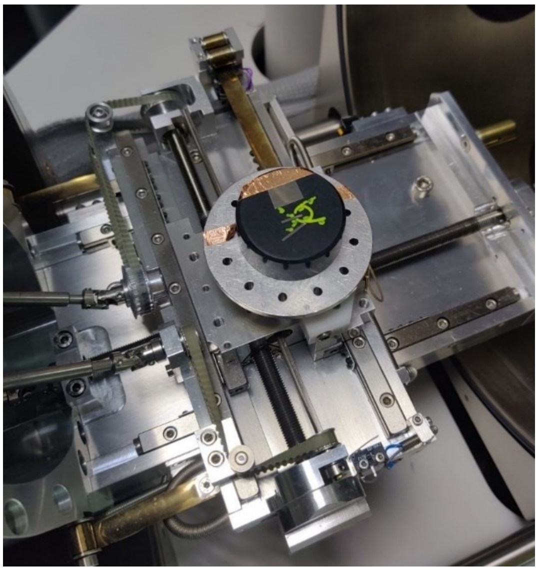

Figure 2.5.2: Insertion of the embedded sample with copper tape in the SEM

In order to see better certain structures, the Scanning Electron Microscope is used, which can create an image of the surface by scanning it with a focused beam of electrons, with a high magnification power, such as 2000X, 4000X, and 8000X. When the electrons interact with the surface, which must be conductive, send signals to the receiver. The SEM works in high vacuum conditions. Because the polymer used to incorporate the AISI 316 samples is nonconductive, a copper tape is applied onto the polymer slightly touching the metal, connecting it to the metal base of the SEM itself. The samples analyzed by the SEM must be conductive, in nonconductive specimens the charged electrons tend to deposit on the surface, causing scanning faults and image artifacts [5]. These signals, which include the number of emitted electrons, their energy, and their wavelength, can reconstitute the topography of the surface studied. The Scanning Electron Microscope is used in this thesis to study the microstructure in the Normal Direction of the specimens brought to UTS and the surface fracture of the specimen brought to failure. The study at SEM was done on specimens deformed at different temperatures.

The SEM used can utilize two different detectors of electrons, depending on what structure is being studied. The first detector is the ETD detector. ETD stands for Everhart – Thornley Detector, the name of its designers. This detector is used to study the morphology of the surface, which appears clearly. Different phases are not enhanced in color, so this detector is not used to study phases' differences in the microstructure. Specifically, this detector was used to study the surface fracture of the samples deformed at different temperatures, at different levels of magnification: 250X, 500X, 1000X, and 2000X [6]. The second detector is the BSED detector, which stands for Electron Backscatter diffraction, used to obtain information on structure, phase, and crystal orientation. This type of detector was used to study the presence and absence of the martensitic phase in the samples worked at different temperatures. [7]

2.6. XRD

X-Ray Diffraction is a non-destructive technique that gives information on the chemical composition of the studied material. The energy of the X-Rays diffracted by the surface is analyzed and the spectrum given can be confronted with the ones present in a database, to evaluate the chemical composition of the surface. The spectrum given by the XRD is characterized by peaks that describe the presence of certain phases. It's also possible to quantify the amount of the phases based on the height of the peaks. The height of the peak is directly proportional to the amount of the phase. In this thesis XRD analysis were done on the Normal surface of the samples brought to UTS to evaluate their composition and their crystalline phase discrepancies.

2.7. Vickers Hardness

In order to characterize the hardness of the material studied, Vickers Hardness Tests were made. A controlled plastic deformation is applied by a force repeatedly on the surface in different spots by an indenter of a specific surface and weight for a specific amount of time.

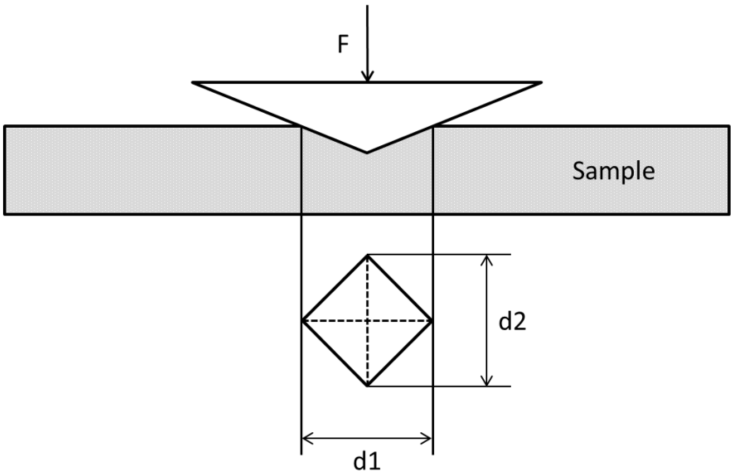

Figure 2.7.1: Standard Procedure for Vickers Hardness Test [8]

The indenter used has a pyramid shape, and 50 grams for 15 seconds load was used. This test was used to evaluate and quantify the Vickers Hardness in the three directions (Normal, Transverse, and Rolling Direction) of the samples brought to UTS at different temperatures.

In the Vickers test, the two diagonals of the indented pyramid are measured by an empirical formula, calculating the Vickers Hardness. The formula used is standardized by UNI EN ISO 6507-1-2018:

$$\mathrm{HV} = 1854.4 \times \frac{P}{d^2}$$

Where P is the Weight of the indenter (in this case 50 grams), d is the average diagonal of indentation (measured in micron):

$$d = \frac{d_1 + d_2}{2}$$

Different indentations are made for each direction to have a distribution of data, therefore an average of the results is made. The standard deviation of this data is calculated as well to evaluate their dispersion. [9]

The result of the Vickers Test is a number that describes the hardness of the material. the higher the number, the harder the material. The regulation UNI EN ISO 6507-1-2018 requires that each indentation is made at least at a minimum distance, which depends on the average diagonal of indentation. Specifically, it is required that the first indentation is made at least 2.5d of distance, where d is the average diagonal of indentation. Each indentation must be distanced from the others for at least 2.5d as well.

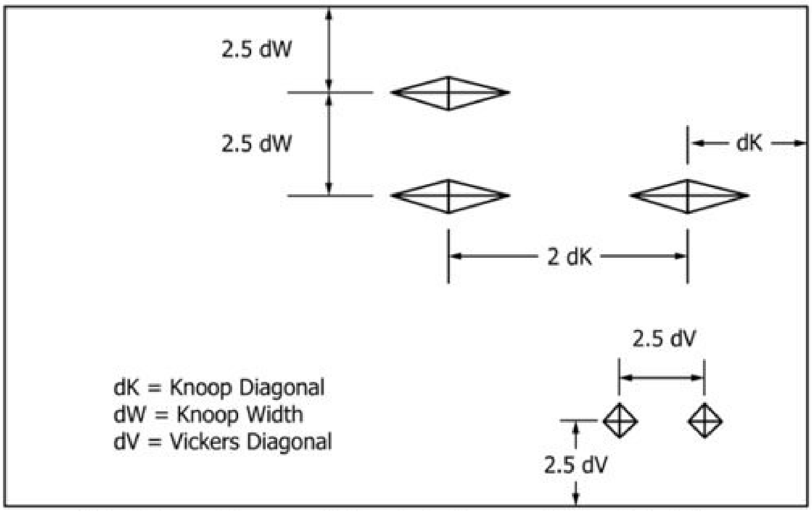

Figure 2.7.2: Distances Required by UNI EN ISO 6507-1-2018 [10]

Bibliography and Sitography

1. https://www.mts.com/en/products/materials/dynamic-materials-test-systems/series-322-test-systems
2. Castello, Branco GA. "*Effect of thermo-mechanical treatment on texture evolution of polycrystalline alpha titanium.*" (2006): 6227-6227.
3. https://www.metallography.com/etching/table.htm
4. Behr, Marion; Behr, Omri (1991). "*Environmentally safe Etching*". *Chemtech*. **21** (4): 210.
5. Stokes, Debbie. "*Principles and practice of variable pressure/environmental scanning electron microscopy (VP-ESEM)"*. John Wiley & Sons, (2008)
6. Goldstein, Joseph I., et al. "*Scanning electron microscopy and X-ray microanalysis*." Springer, (2017)
7. Schwartz, Adam J., et al., eds. "*Electron backscatter diffraction in materials science*." Vol. 2. New York: Springer, (2009)
8. https://swissproficiency.com/en/product/vickers/
9. Smith, Robert L., and G. E. Sandly. "*An accurate method of determining the hardness of metals, with particular reference to those of a high degree of hardness.*" *Proceedings of the Institution of Mechanical Engineers* 102.1 (1922): 623-641.
10. UNI EN ISO 6507-1-2018, "*Materiali Metallici – Prova di Durezza Vickers – Parte 1: Metodo di prova", (2018)*

3. Numerical Model

In this chapter, the structure of the numerical model is discussed. The main objective was to evaluate the real Stress-Strain curves calculated by the software for all the geometries of the samples, but also to evaluate the Load to Run Length graphs which is the main output of the uniaxial tensile test. Another aspect evaluated was the contour plot for each specimen, which indicates the stresses formed on the samples, quantifying where the main concentrated stresses locate and their peak values. From these data, also the True Stress-Strain curves were evaluated, correlating them to the Tensile Test carried out.

3.1. LS-DYNA Software

The software used for the development of the numerical model was LS-DYNA, a Multiphysics solver made by Ansys. LS-DYNA is a simulation program capable of simulating the response of different materials to different loads. This software can numerically replicate impacts, fractures, large plasticity, penetration, drop tests, biomedical and medical devices simulations, and vehicle crash. [1]

This software works on the theory of the Finite Element Method Analysis, which allows to solve partial differential equations where the geometry of the sample is subdivided into parts called finite elements. The finite elements introduced are created by space discretization of the geometry, which is implemented by the creation of a mesh of the specimen. It's using the mesh that the partial differential equations are simplified in a system of algebraic equations, which are solved by the software in question. The elements used are characterized by nodes, which connect every element with each other.

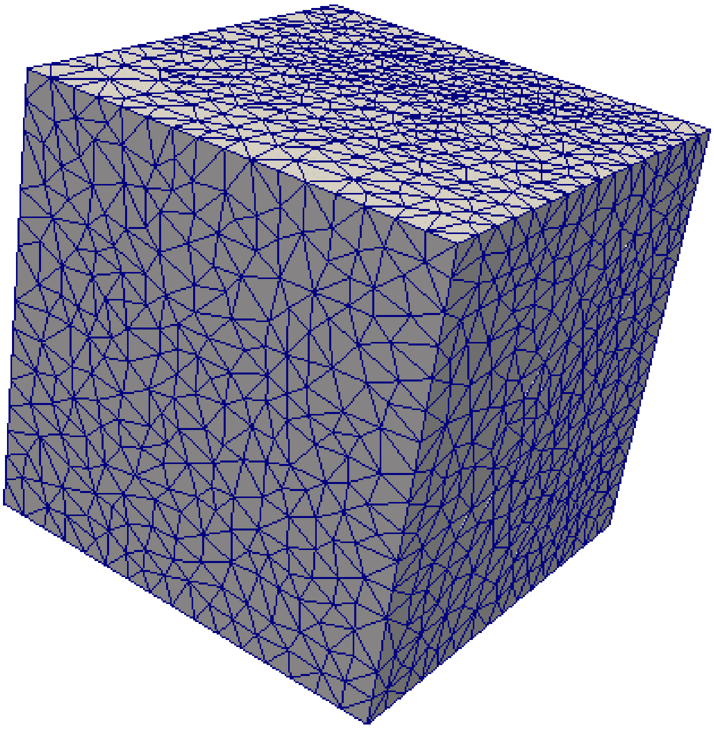

Figure 3.1.1: Typical FEM Object [2]

The subdivision of the object is one of the main aspects of FEM which can highly influence the quality of the results but also the time used to reach a solution. A mesh made of very small elements allows an accurate solution of the problem, requiring at the same time a high computational time and power. A less fitted mesh allows a less time-consuming but less accurate solution. In this way, it appears important to find the right balance between the mesh's size and the computational time and power required. Different geometries of the elements that form the mesh can be used, such as triangle, quadrangle, tetrahedron elements, and so on.

For this work, the LS-DYNA software was used to simulate uniaxial tensile tests for all the geometries.

3.2. Specimen's Geometry and Mesh

The geometry of the samples studied by uniaxial tensile test was incorporated into LS-DYNA using the 2D-mesher which allows to create a 2D geometry that can be meshed directly. This allows to create geometries by defining points of the geometries and connecting them to create a close shape, the object remains however in a two-dimensional form. The 2D-Mesher automatically creates Shell Elements, which are then given a defined thickness. It is then possible to increase the derivation points to increase the number of elements that form the depth of the samples. In the Finite Element Method, it is advised to increase the number of elements in the parts where the geometry of the object is more complex.

For the geometries used, the size of the mesh was defined on the number of elements desired on each edge of the specimen. In this way, the size and number of the elements could be easily tuned and modified to the accuracy required. In the parts where less accuracy was required 30 elements per edge were used. These parts were the wider extremities where the sample is gripped for the tensile test. A more accurate description of the mesh used is going to be analyzed thoroughly geometry per geometry.

- Smooth Sample: As said before, 30 Shell elements were used for each of the edges correlated to the wider parts. For the middle part, which is the one studied and where stresses mainly concentrate, 90 elements per edge were applied.

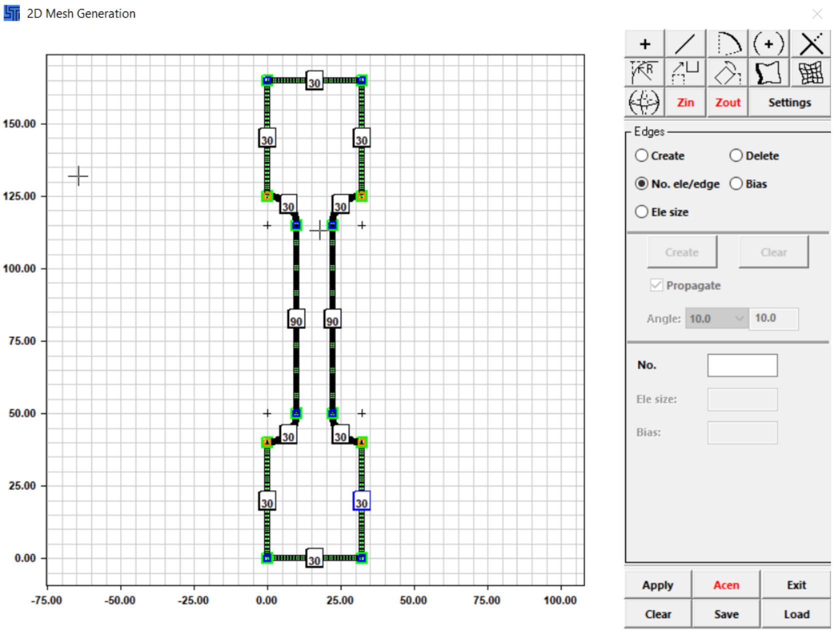

Figure 3.2.1: Mesh of Smooth Sample

- Notched Samples: for each notched sample, so for R2, R5, and R10, the same number of elements used for the wider parts of the smooth specimen were used, so 30 elements per edge. In the most critical part of the geometry, which is the notched region, 30 elements per notch were used.
- Shear Sample: The extremities have 30 elements per edge in the smaller parts and to have a homogeneous mesh geometry 60 elements were applied on the longer parts. The complex geometry of the shear samples required a highly fitted mesh in the central region, specifically where the small notches carved into the specimen came closer. On the edges hollowed out of the specimen, 30 elements per edge were applied. On the small notches, of near 1mm radius, 30 elements per notch were used. In this way, a highly fitted mesh was achieved in the central and more critical part of the sample.

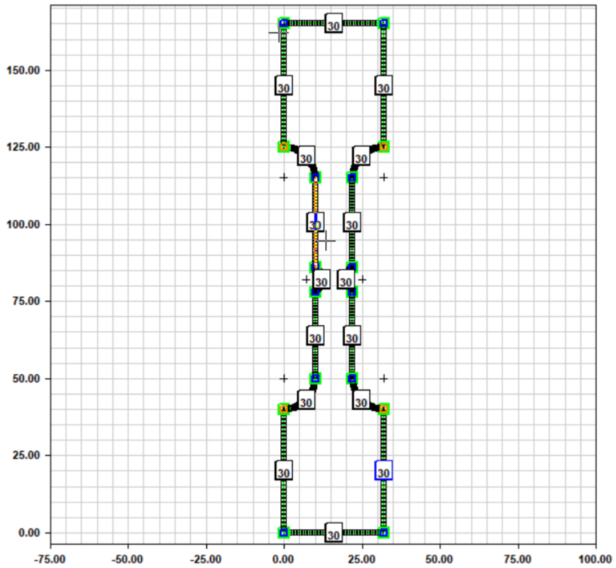

Figure 3.2.2: Mesh of R5 Notched Sample

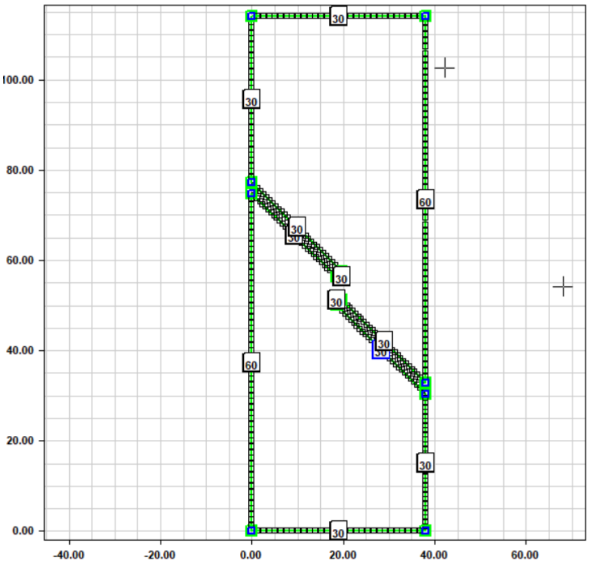

Figure 3.2.3: Mesh of Shear Sample

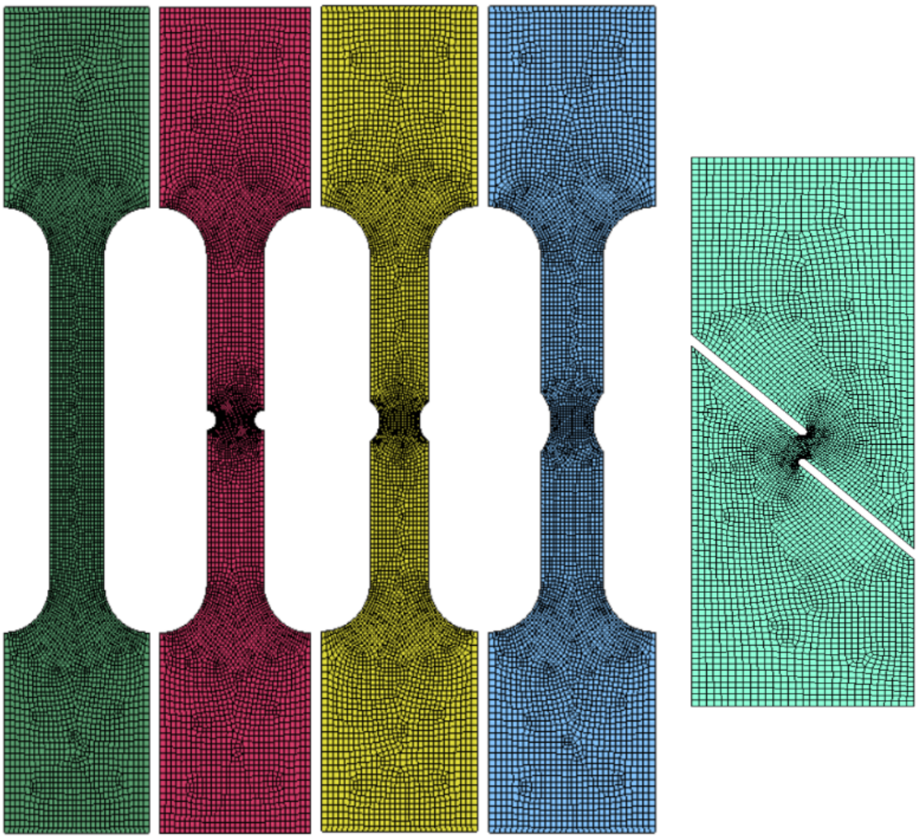

Figure 3.2.4: All Samples Meshed

3.3. Structure of the Numerical Model

Most Finite Element Method software such as LS-DYNA requires to define in advance the characteristics of the material used, which will be then connected through a section to the geometry of the sample. Boundary conditions, which can describe both constraints and imposed displacements are then applied to the required nodes. The main structure of the numerical model is discussed in this subchapter.

It's important to note that LS-DYNA software doesn't work with measurement units, it is up to the user to maintain consistency with the measures chosen preventively.

The measurement units used in LS-DYNA for this work are:

- Geometry units: [mm]
- Force/Load = [N]
- Young's Modulus E: [MPa]
- Stress σ: [MPa]
- Density ρ: $[{}^{Kg}/_{mm^3}]$

In the simulations developed the samples were brought to failure by inserting the value of strain at fracture in the description of the material used. From these simulations an evaluation of the Real Stress-Strain curves and peak values of Stress were done, as well as an analysis of the Load to Run Length graphs. Specifically, the outcome of the Load to Run Length graphs of LS-DYNA were normalized in order to successfully compare them with the real Load to Run Length curves of the tensile test, output of the load frame MTS-322.

3.3.1. Material Used

The material used for the numerical model is the *Piecewise Linear Plasticity* (024), which is one of the most common materials used for objects that requires a plastic behavior. The *Piecewise Linear Plasticity* material requires in input certain values, which for the Smooth specimen are:

- Density of the material ρ (RO): 7.830×10^{-6} $[{}^{Kg}/_{mm^3}]$
- Young's Modulus (E): 205×10^3 [MPa]
- Poisson's Ratio ν (PR): 0.29
- Yield Stress (SIGY): 352.66 [MPa]
- Strain at Fracture: 0.10433

The material defined also requires a true Stress-Strain curve as an input in order to characterize its behavior when deformed. The curve inserted into the specifics of the *Piecewise Linear Plasticity* was obtained by a uniaxial tensile test carried at room temperature of a Smooth specimen. The curve in question was polished and a moving average was applied to remove possible outlined data:

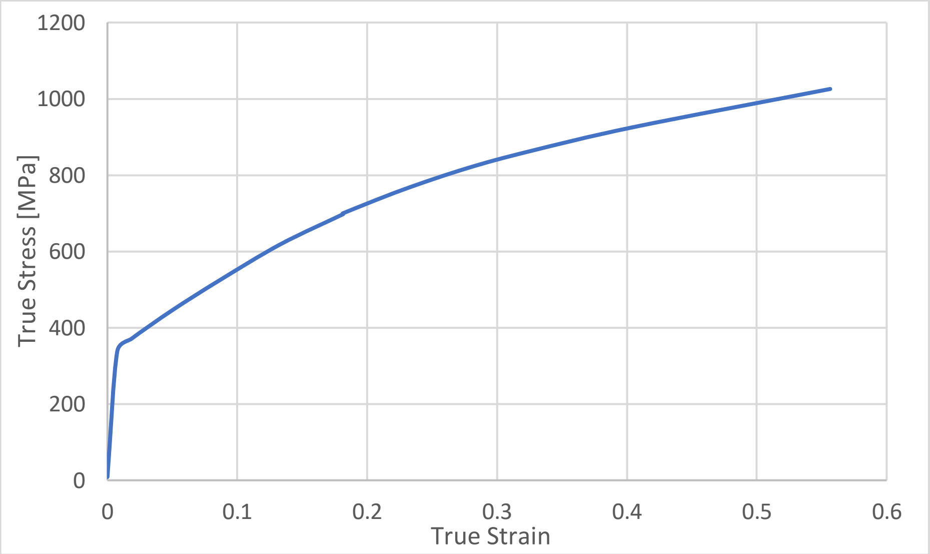

Figure 3.3.1: True Stress-Strain Curve used to Define the material

3.3.2. Boundary Conditions

In order to simulate a uniaxial tensile test in a Finite Element Method software, boundary conditions that describe the movement imposed by the MTS-322 to the samples must be defined, associating them to a group of well-defined nodes in advance. To simulate better the grips of the hydraulic press that carry the tensile test a larger portion of nodes was considered, not just the nodes on the upper and lower edge.

Two types of boundary conditions were applied:

- Displacement: A movement is imposed to the upper nodes of the sample. The movement is defined by a linear Time to Run Length graph defined previously. The nodes are moved synchronously with constant velocity, once they reached the distance required they stop even if failure is not reached. If the value of strain at failure is not inserted in the description of the material, the sample will elongate until the nodes reach the displacement required. These conditions describe the portion of the sample moved in the real tensile test.
- Constraint: The lower nodes are grouped together and fixed. Their axial movements are fixed, as are their rotational movements. These conditions describe the part of the sample gripped by the clamps of the MTS-322.

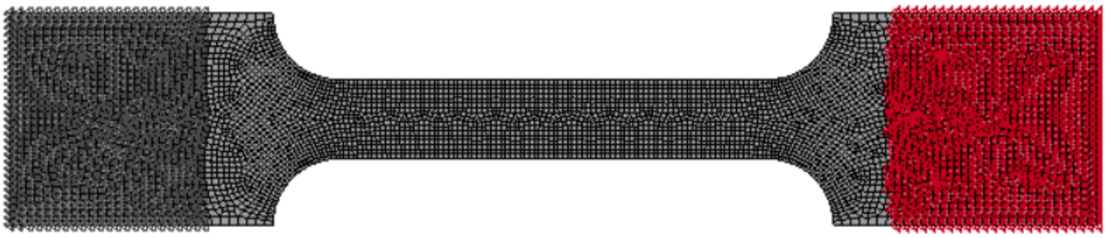

Figure 3.3.2: Highlighted nodes where Boundary Conditions are applied

3.4. Outputs

LS-DYNA lets the user choose different outputs to analyze after the simulation. The main focus was made on the True Stress values and where Stresses were concentrated, and the True Strain correlated to them, to obtain the True Stress-Strain Curves. One important aspect was to analyze the contour plot of each sample, which expresses the Stress values for each element of the mesh in order to evaluate peak and concentrated Stresses.

These outputs were recorded to evaluate the results of the simulation:

- Contour Plot of each sample
- Stress Values: Peak Stress, concentrated stresses in the middle part
- Strain Values in the most deformed parts
- Force required to deform the specimen, calculated by the sum of the force evaluated on each fixed node
- Displacement of the upper node

Bibliography and Sitography

1. https://www.ansys.com/it-it/products/structures/ansys-ls-dyna
2. Xing, Feng, Roland Masson, and Simon Lopez. *"Parallel numerical modeling of hybrid-dimensional compositional non-isothermal Darcy flows in fractured porous media*." Journal of Computational Physics 345 (2017): 637-664.

4. Uniaxial Tensile Tests Campaign – Valuations and Results

In this chapter all the results from the uniaxial tensile tests and the post-deformation analysis are discussed, as well as how the tensile tests were carried out for each temperature studied.

The Samples tested with tensile tests were cut at 0° and 90° from the Rolling Direction, samples cut at 45° were not investigated. For all the samples, tensile tests at 5 different temperatures were carried out in order to evaluate the change in behavior of the material. Five geometries which are Smooth, R2, R5, R10 notched, and Shear specimens, were examined at five different temperatures thus achieving 50 tensile tests.

The first investigation was done on the 0° and 90° cut samples to evaluate the behavior of the material worked at room temperature, and to lay the foundations for the numerical model discussed in the previous chapter. From these tests both the True Strain-Stress and Engineering Strain-Stress curves were achieved, with the help of the ARAMIS Software which can evaluate and quantify the True Strain of the deformed specimen thanks to a camera that record the tensile test.

	Smooth	**R2**	**R5**	**R10**	**Shear**
Actual Length [mm]	65	4	8	12	3
Nominal Surface [mm^2]	12	8	8	8	3

Table 4.0.1: Geometry properties for each Sample

	Smooth	**R2**	**R5**	**R10**	**Shear**
Strain Rate $[s^{-1}]$	0.05	0.75	0.38	0.25	1

Table 4.0.2: Strain Rate of the test $[s^{-1}]$ for each Geometry

A nondeformed, “As Delivered” Smooth sample was studied via optical micrography and Vickers Hardness Test in order to have a benchmark for further microstructure investigation. From this first campaign of tensile tests mechanical properties were collected such as the Yield Strength for each specimen, Ultimate tensile strength, peak Stress and its correlated strain, and Strain at fracture.

The second investigation was to evaluate the behavior of AISI 316 at the range of temperatures defined previously, with the aim of the climate chamber, liquid nitrogen, and the electricity generator. It’s important to say that the True Strain-Stress curves were not recorded for the tests where the climate chamber was used because of the impossibility to record the process of deformation of the sample inside the climate chamber. So, the evaluation of the strain at UTS was done regarding the Engineering Stress-Strain curves.

The third investigation was to take the values of Ultimate Tensile Strength for each Smooth specimen deformed at different temperatures to deform another Smooth sample in the same range of temperatures to UTS in order to later evaluate the effects that Strain and Temperature make on the microcrystalline structure with the Optical Microscope and SEM. The post-deformation and post-fracture evaluation is then carried out by analyzing the three directions (Rolling, Normal and Transverse Direction) by chemically etching the surface and by seeing the microstructure with the Optical Microscope and then SEM, evaluating also the surface fracture of the samples.

Other tests were then carried out, specifically the XRD test to quantify the crystalline phases of the structure of grade 316 once worked at different temperatures and how their concentration changes, and the corrosion test to evaluate how the temperature modify the corrosion resistance.

The results of the tests carried out will be thoroughly analyzed in this chapter.

4.1. Evaluation of the material at Room Temperature

The material in the form of samples with different geometries was evaluated at room temperature through uniaxial tensile tests to achieve True Stress-Strain curves necessary for the numerical model. In this phase the samples cut from the metal sheets at 0° and 90° to the Rolling Direction were tested. It was important to see whether there were differences and discrepancies between the results of the sample cut in orthogonal directions from the rolled metal sheet, so between the 0° and 90° samples.

4.1.1. 0° Samples

Tensile tests until fracture of the samples were done at room temperature for each geometry in order to achieve the True and Engineering Stress-Strain curve:

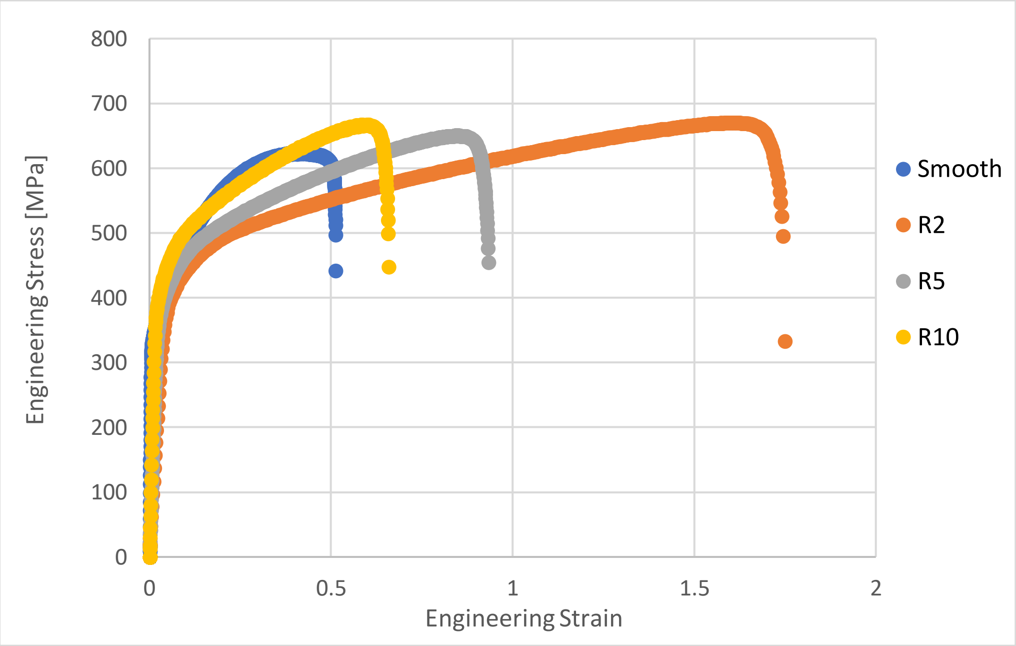

Figure 4.1.1: Engineering Stress-Strain at Room Temperature – 0° Samples

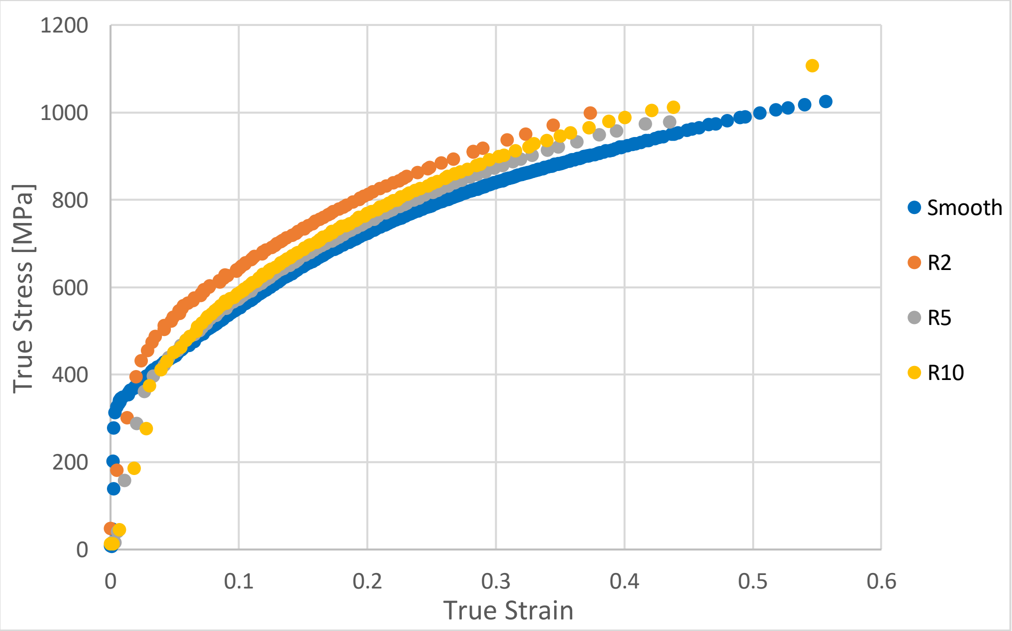

Figure 4.1.2: True Stress-Strain at Room Temperature – 0° Samples

It is worth noting that, as said previously, the True Stress is always higher than the Engineering one, while the True Strain is always lower than its Engineering counterpart. Also, it's easy to note that the values of the Engineering Strain for the notched sample are conditioned by the length of the notch, which affects the calculation of the

Engineering strain. This is because just the notched part, the portion of the sample which is deformed, is taken into consideration for the Engineering Strain. For example, for a sample with an R2 notch, the initial length taken into consideration is 2mm which is the effective portion that deforms in the uniaxial tensile test. This effect is way less important in evaluating the True Strain, as can be seen in Figure 4.1.2, where the strain is very similar to each sample studied.

It's the True Strain-Stress curve of the 0° smooth sample that is used in the numerical model, after being polished from outlined values related to errors in the ARAMIS software used to obtain the true Strain.

Due to the particular geometry of the Shear samples, their Engineering and True Stress-Strain curves were not inserted in the same graph as for the other specimens, but the curves of the shear samples deformed at different temperatures were united to evaluate their change in behavior.

4.1.2. 90° Samples

The same number of tests were done on the samples cut at a 90° angle from the rolling direction, achieving the engineering and true Strain-Stress curves.

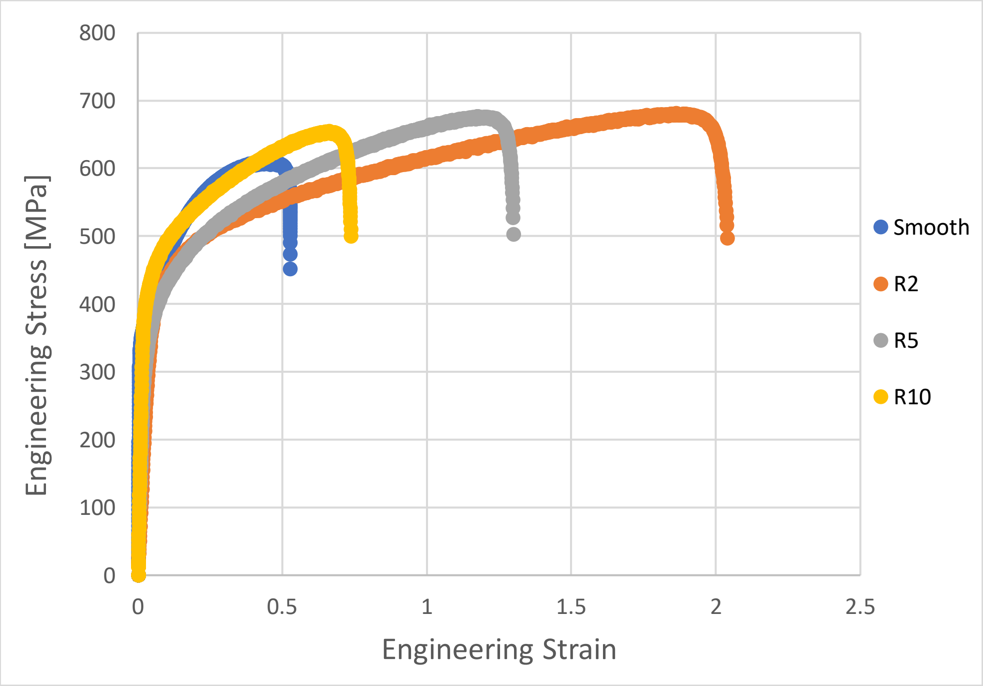

Figure 4.1.4: Engineering Stress-Strain at Room Temperature - 90° Samples

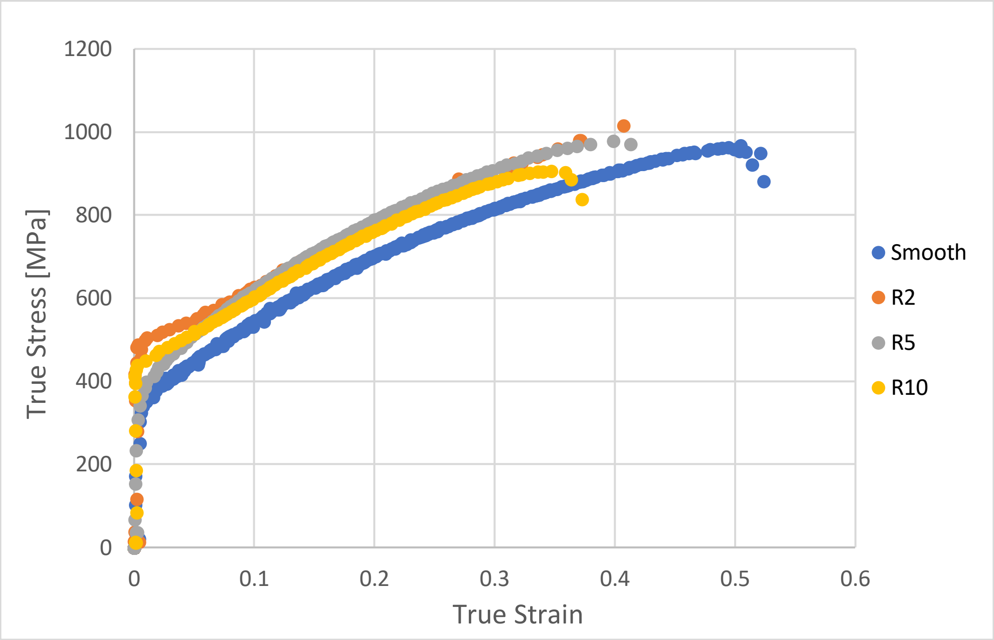

Figure 4.1.5: True Stress-Strain at Room Temperature - 90° Samples

As it can be seen from the graphs proposed, the mechanical behavior in response to a uniaxial tensile test is similar between the specimens cut at 0° and 90° to the Rolling Direction. The inspection at the defined range of temperatures will be done on the samples cut at the different angles proposed also to evaluate the discrepancies between the two.

4.1.3. Comparison of 0° and 90° Samples

To precisely evaluate the differences between the samples cut by 0° and 90° angles to the Rolling Direction, the values of Ultimate Tensile Strength, calculated from the Engineering Stress, and the correlated Engineering Strain are put in comparison:

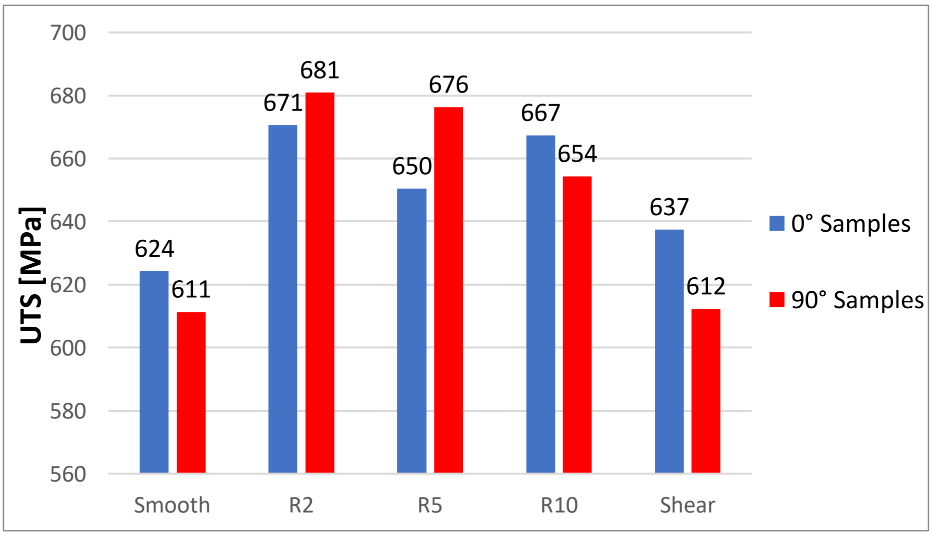

Figure 4.1.5: UTS [MPa] for 0° and 90° Samples

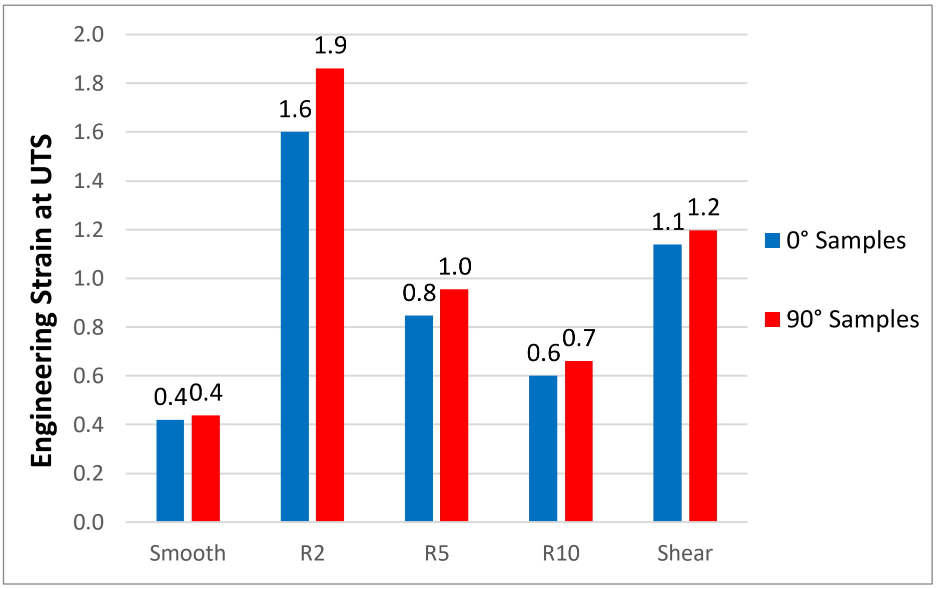

Figure 4.1. 6: Strain at UTS for 0° and 90° Samples

The Engineering values were taken into consideration because, as said before, it was not possible to clearly calculate the True Strain and Stress for the tests done in the climate chamber. Just the Engineering Stress and Strain were calculated and recorded for the tests done at temperatures higher and lower than room temperature. The values taken into consideration highlight a higher strain at UTS for the samples cut at 90° to the Rolling Direction, while the UTS calculated by the engineering stress is similar for each geometry. The small discrepancies in the values of deformation and UTS can be attributed to the anisotropy given by the rolling of the sheets, or by little variations caused by the load cells of the MTS-322.

4.2. Evaluation of the Material at Sub-Zero Temperatures

Once the evaluation of the material at room temperature was done and recorded, the study of the behavior of AISI 316 at sub-zero temperatures started. With the aid of the climate chamber and liquid nitrogen, temperatures of -50°C and -100°C were achieved and it was possible to carry uniaxial tensile test for each sample cut at 0° and 90° to the rolling direction. To achieve a more complete picture of the performances of the material, tests at 300°C and 700°C were accomplished.

The Engineering Stress-Strain curves were obtained, and from these the main focus was done on the values of UTS and the strain reached at UTS. If the strain at UTS for the samples tested at sub-zero temperatures was higher than the ones calculated at higher temperatures, it indicated that a formability improvement was achieved by sub-zero forming. This was considered because accomplishing a higher value of deformation without reaching fracture allows to further form or work the material. Subsequently, to evaluate in percentage the formability improvements a normalization of the values of UTS and strain at UTS was done.

The table proposed here collects all the important data used to analyze the behavior of AISI 316. Specifically, it was important to evaluate the maximum load reached, the length at which the specimen fractured, the Ultimate Tensile Strength calculated in MegaPascal and the Strain at which UTS was reached.

Specimen	**Temperature**	**Max Load**	**Run Length at Fracture**	**UTS**	**Strain at UTS**
	[°C]	[N]	[mm]	[MPa]	-
Smooth 0°	-100	10373.8	30.8	864.5	0.4
	-50	8991.3	35.5	749.3	0.5
	25	7490.5	32.9	624.2	0.4
	300	5684.5	25.3	451.3	0.3
	700	4009.6	13.2	334.1	0.1
Smooth 90°	-100	10501.6	32.1	864.5	0.4
	-50	9205.0	38.6	767.1	0.5
	25	7316.2	34.2	609.7	0.4
	300	5452.6	25.9	454.4	0.4
	700	3730.9	14.8	310.9	0.2
R2 0°	-100	7912.3	12.8	989.0	3.1
	-50	6766.8	10.5	845.8	2.5
	25	5364.2	7.0	670.5	1.6
	300	3638.8	5.1	454.8	1.2
	700	2898.6	3.5	362.3	0.8
R2 90°	-100	7836.8	11.5	979.6	2.7
	-50	6695.7	8.7	837.0	2.0
	25	5446.7	8.1	680.8	1.9
	300	3885.5	6.4	485.7	1.5
	700	3138.8	4.2	392.3	1.0
R5 0°	-100	7906.9	16.4	988.4	2.0

	-50	6543.9	8.8	818.0	1.0
	25	5203.1	7.5	650.4	0.8
	300	3701.2	5.5	462.7	0.7
	700	2912.7	3.7	364.1	0.4
R5 90°	-100	7651.6	9.9	956.4	1.2
	-50	6759.2	8.7	844.9	1.0
	25	5433.8	8.4	679.2	1.0
	300	3967.4	6.7	495.9	0.8
	700	2973.6	4.1	371.7	0.5
R10 0°	-100	7266.9	9.3	908.4	0.7
	-50	6455.7	8.8	807.0	0.7
	25	5338.5	7.9	667.3	0.6
	300	3708.2	5.9	463.5	0.5
	700	2942.5	4.1	367.8	0.3
R10 90°	-100	7759.4	11.1	969.9	0.8
	-50	6626.1	9.2	828.3	0.7
	25	5234.4	8.8	654.3	0.7
	300	3891.3	6.9	486.4	0.5
	700	3128.0	4.7	391.0	0.4
Shear 0°	-100	2512.4	3.4	837.5	1.0
	-50	2297.1	3.7	765.7	1.1
	25	1912.2	3.9	637.4	1.1
	300	1122.3	3.8	374.1	0.8
	700	781.4	2.1	260.5	0.4
Shear 90°	-100	2551.9	3.2	850.6	1.0
	-50	2327.0	3.7	775.7	1.1
	25	1836.9	4.4	612.3	1.2
	300	1152.2	3.3	384.1	0.8
	700	899.1	2.3	299.7	0.5

Table 4.2.1: Collected Data from Tensile Tests at different Temperatures

4.2.1. Smooth Samples

In this subchapter the results of the Smooth samples cut at 0° and 90° from the rolling direction will be discussed. The engineering Stress and Strain curves of the samples deformed at different temperatures are united in the same graph to evaluate the differences in behavior:

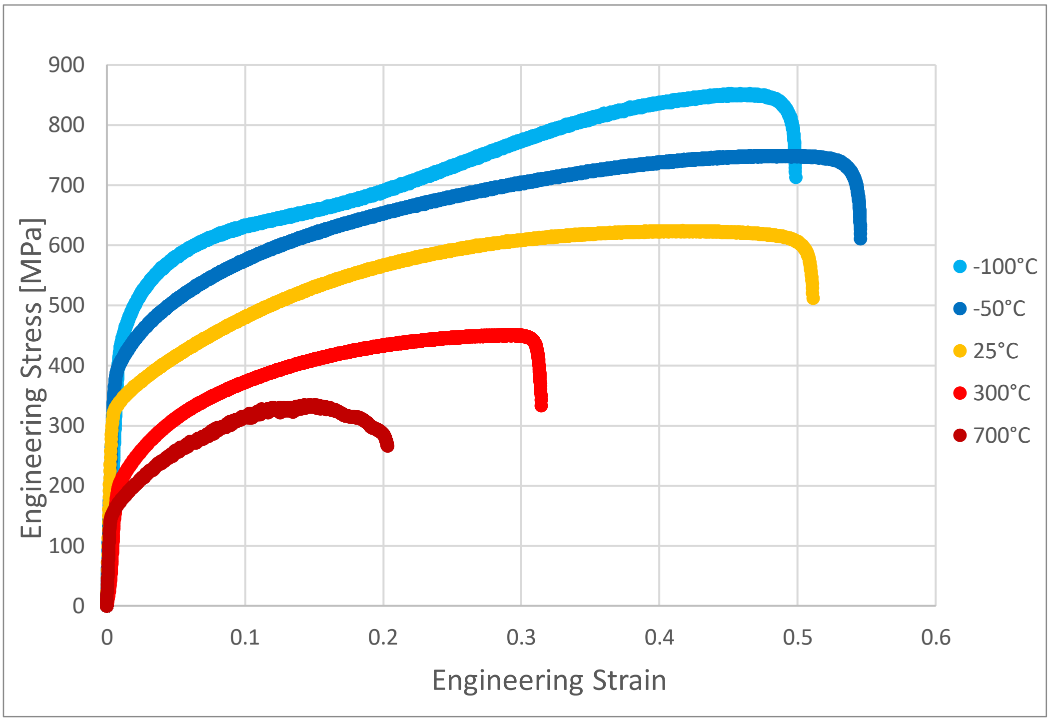

Figure 4.2.1: 0° Samples - Engineering Stress-Strain

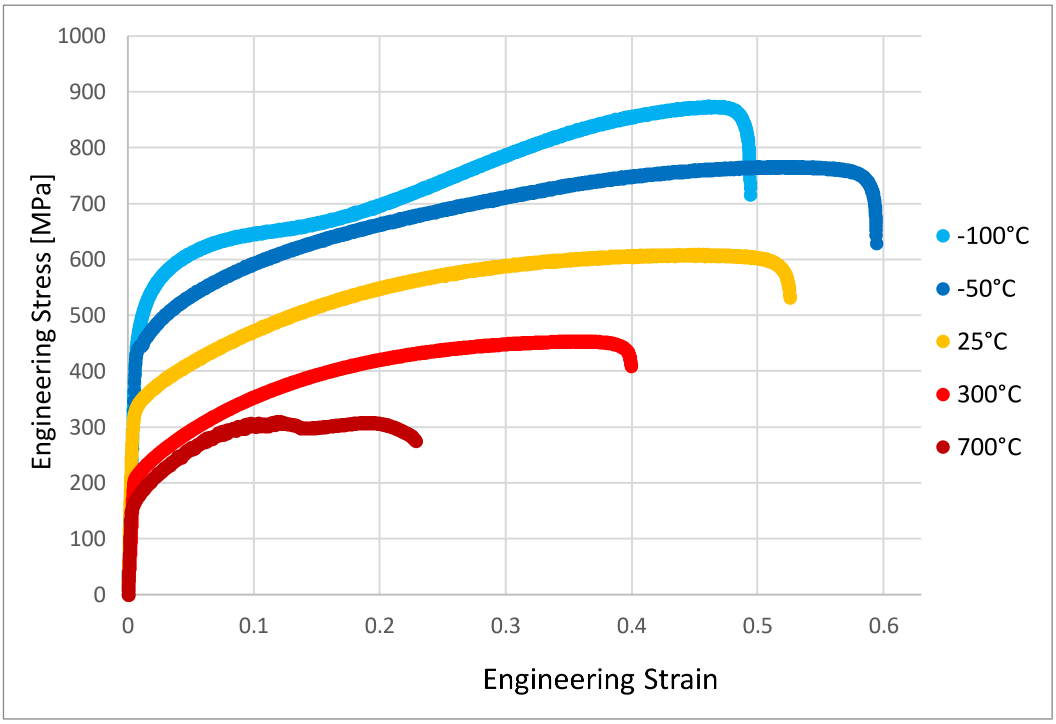

Figure 4.2.2: 90° Samples - Engineering Stress-Strain

As it can be seen from the graphs proposed in figures 4.2.1 and 4.2.2, a clear formability improvement is achieved at the -50°C temperature, where the strain calculated at UTS appears higher than the one reached at temperatures higher and lower than -50°C. It also appears that the deformation obtained raising temperatures gets increasingly lower. One important thing to note is that the behavior of the samples cut at different angles to the Rolling Direction appears to be very similar.

As seen by the graphs, by lowering the temperature at which the tensile test is carried out, the Yield strength rises, as well as UTS. One aspect seen in this study is also how the Force that the load cells of the MTS-322 and the Run Length required to fracture the sample clearly decreases as the temperature is raised.

Two particularities emerge from the graphs proposed: the behavior of AISI 316 at 700°C and -100°C. The first one can be easily explained by the heating implemented by the electricity generator, which is not able to maintain a perfect constant output of electricity, thus producing peaks and lows of electricity which influences the performance of the heated material. A high peak of current, which is necessary to raise the temperature of the sample studied, could influence locally the behavior of the material which is heated non-homogenously.

The second one, which is the behavior of AISI 316 at -100°C deserves to be described more accurately in a later subchapter once the performance of each geometry is evaluated.

4.2.2. Notched Samples

As said previously, the behavior of the notched samples evaluated by the Engineering Stress and Strain is highly affected by the notch itself. This is because the actual portion of the sample that deforms and that is taken into consideration is the notched part, which will be called from now on as "Actual Length". Because in each notched sample the actual width remains equal, the notched length changes due to the radius used to make the notch.

Notched Sample	**Actual Length**	**Actual Width**
R2	4	8
R5	8	8
R10	12	8

Table 4.2.2: Geometrical Properties of Notched Samples

As said before just the Engineering Stress-Strain curves were recorded due to the impossibility to obtain the True Stress and Strain through the climate chamber.

Notched R2

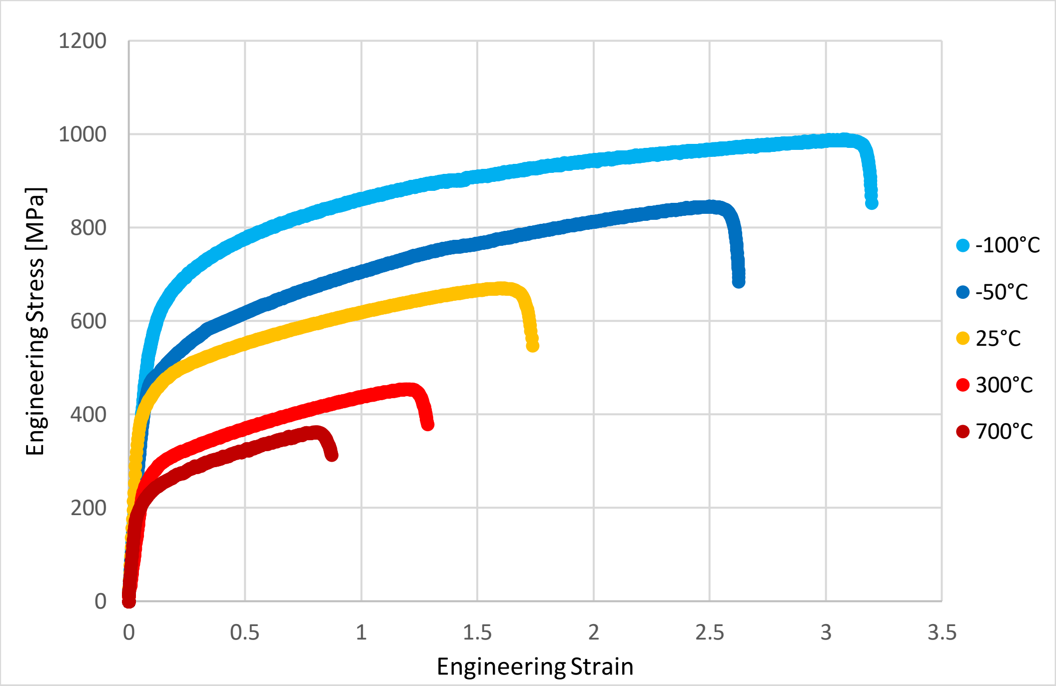

Figure 4.2.3: 0° Samples - Notched R2

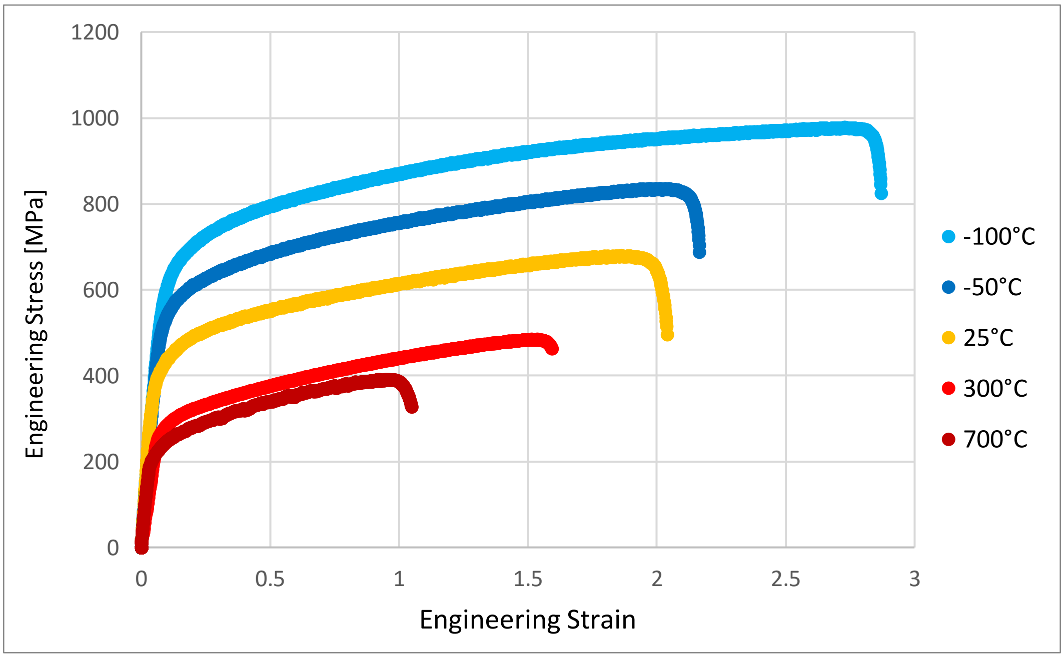

Figure 1.2.4: 90° Samples - Notched R2

The behavior of the Notched R2 cut at 0° and 90° appears similar. The Strain reached at UTS is higher in the samples deformed at sub-zero temperatures. The Strain decreases accordingly to the increase of temperature. The Deformation achieved at -50°C and -100C° appears to be higher in the 0° samples as compared to the 90° counterparts.

Notched R5

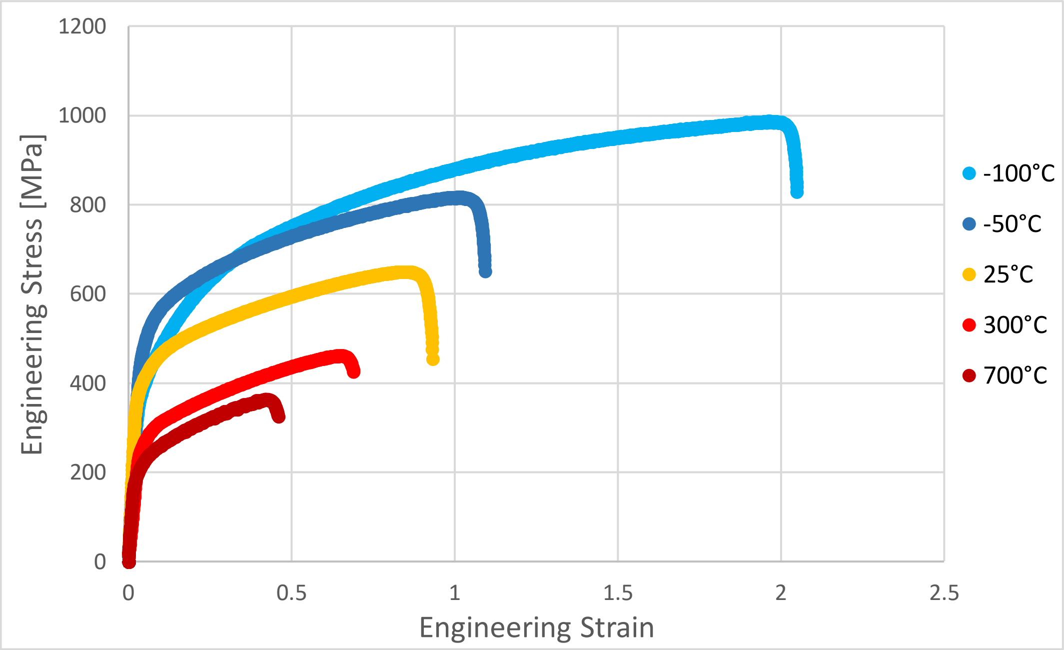

Figure 4.2.5: 0° Samples - Notched R5

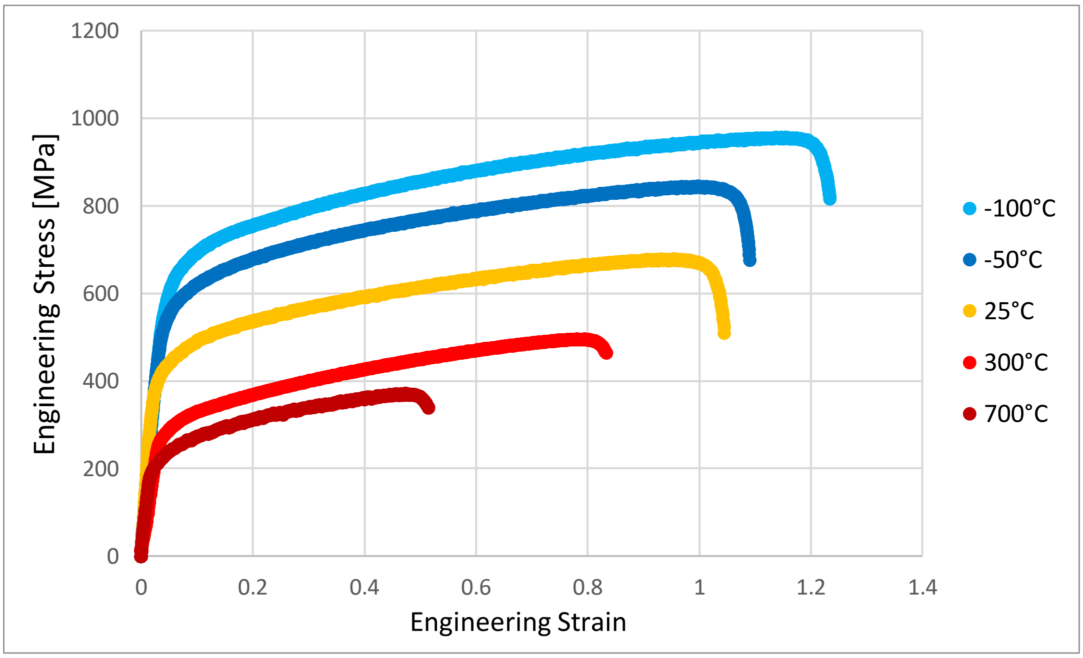

Figure 4.2.6: 90° Samples - Notched R5

The behavior of the notched R5 appears similar to the notched R2, but with lower Strains due to the size of the notched region. The performance of 0° and 90° notched R5 samples appears comparable between the specimens.

Notched R10

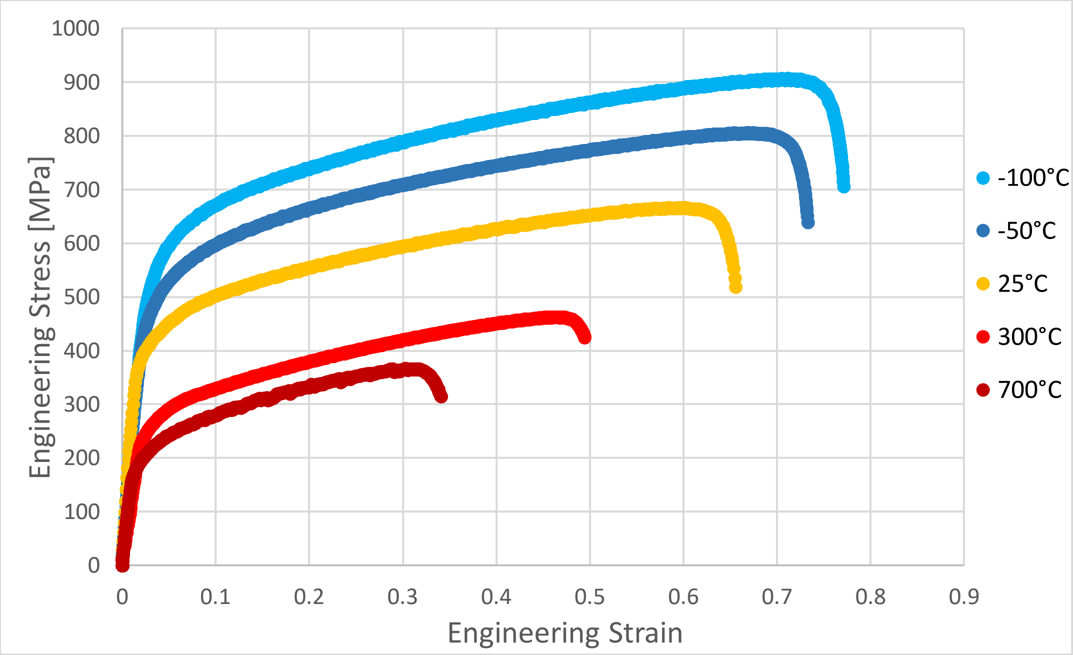

Figure 4.2.7: 0° Samples - Notched R10

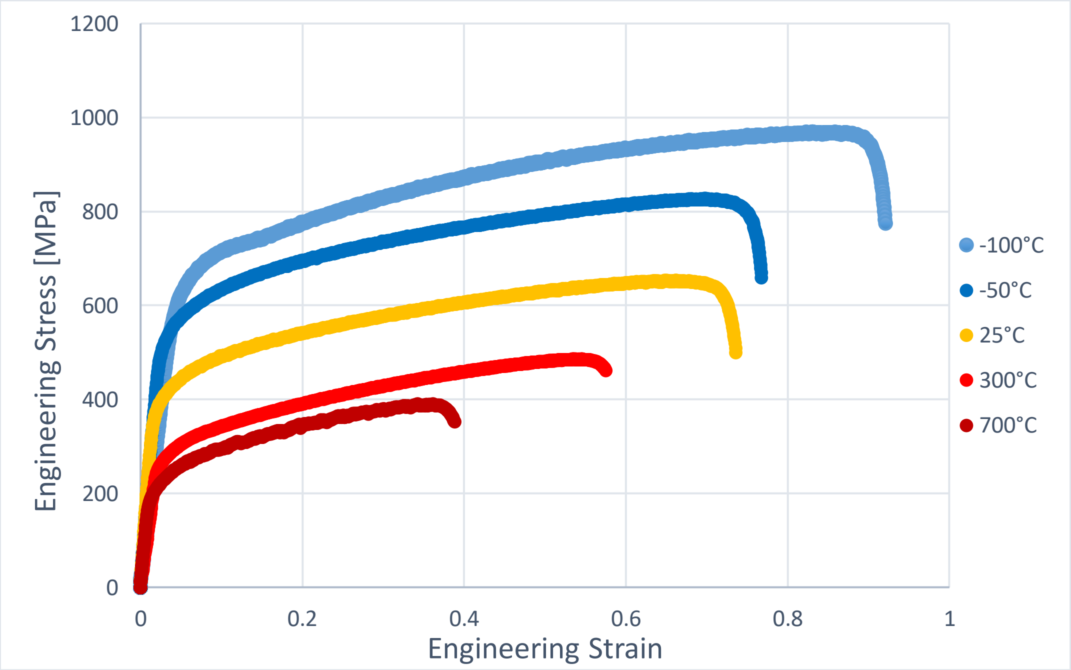

Figure 2.2.8: 90° Samples - Notched R10

With the graph of the notched R10, all the notched specimens are analyzed. It appears clearly that their behavior is similar. The Engineering Stress-Strain curves have all the same shape and the formability improvement can be seen for each geometry. The Strain calculated at UTS at different temperatures is higher at sub-zero temperatures. It's important to point out that the values of Engineering Strain are highly affected by the Actual Length considered in the calculations.

From the graphs proposed it's clear that a formability improvement is achieved for the notched specimens.

4.2.3. Shear Samples

In this subchapter the behavior of the Shear Sample is discussed. The Actual Length considered in the calculation was the central region of the sample, which was of 3mm, the Initial Area was $3mm^2$. Due to their geometry the engineering Stress-Strain curves appear different from the ones seen before:

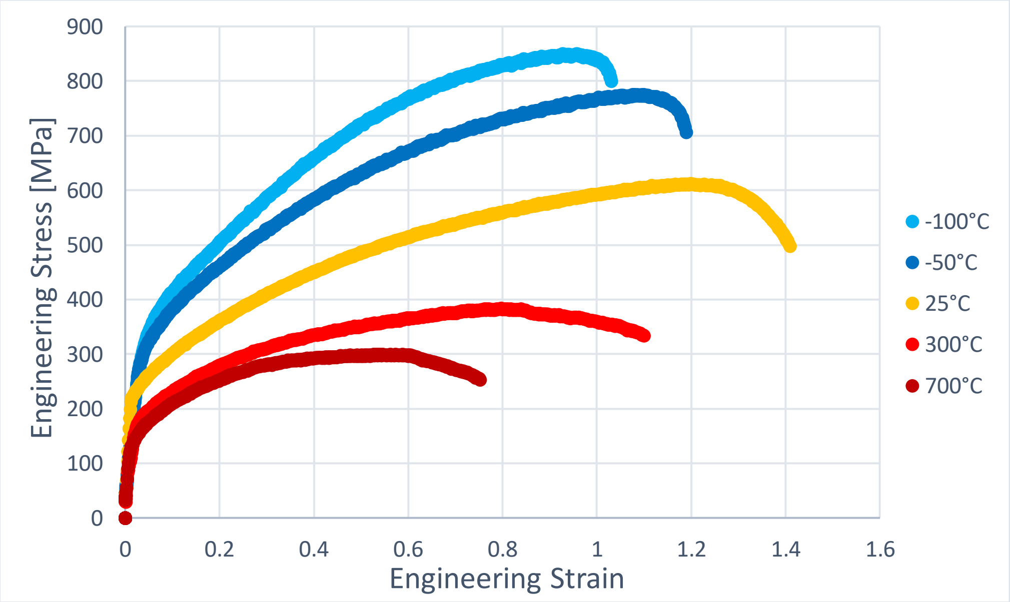

Figure 4.2.9: 0° Samples - Shear Specimens

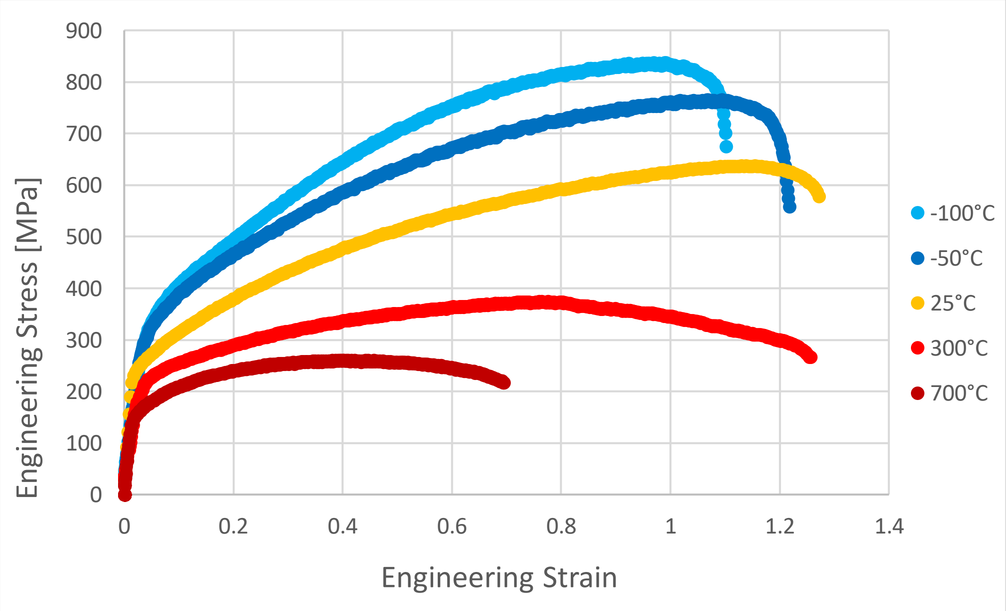

Figure 4.2.10: 90° Samples - Shear Specimens

It is clear that the performance of the Shear Samples cut orthogonally from the stainless steel sheet is similar. Discrepancies are recognized in comparison to the notched and smooth specimens, the biggest one is the absence of formability improvement at sub-zero temperatures.

4.3. Behavior's Analysis of -100°C Smooth Samples

As seen from the graphs proposed of the performance of the Smooth Sample, both at 0° and 90° from RD, the behavior at -100°C of these specimens is rather peculiar. The shape of the engineering Stress-Strain curves of the smooth samples is indeed different from every other curve recorded at higher temperatures, and also from the notched and shear samples deformed at -100°C. A lot of different tests were carried out at -100°C for the smooth specimens to be totally sure that the curves obtained were the ones typical of the AISI 316 deformed at such temperature. In this subchapter, I'll discuss this behavior and why it occurs only for the Smooth Specimen.

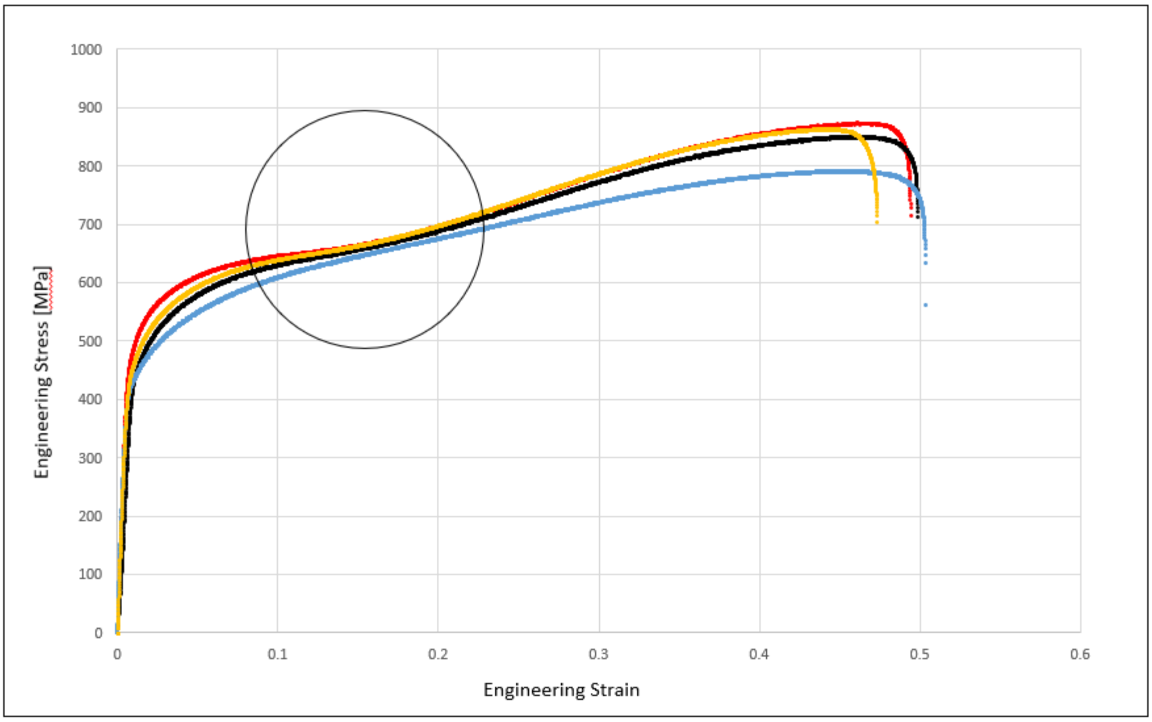

Figure 4.3.1: Different Strain-Stress Curves at -100°C

In the graph proposed in figure 4.3.1, a few Engineering Stress-Strain curves of Smooth samples deformed at -100°C are presented, both belonging to samples cut at 0° and 90° from RD. It is clear that at a Strain of 0.2 a peculiar slope in the behavior, highlighted in Figure 4.3.1, is recorded which strongly affects the Strain at fracture. This slope is caused by the TRIP effect described in the first chapter. A transformation of the Austenite phase into Martensite phase induced by plastic strain modifies the mechanical properties of the AISI 316. As seen before, the TRIP effect is highly affected by the Stacking Fault Energy of the metal, by the load used, and by the temperature at which the work is carried out. In this case the low SFE of AISI 316, combined with the very low temperatures and with the high loads required to deform the sample, induce the TRIP effect, thus increasing the strength of the material itself. It's the increase of the strength of the material that causes that peculiar slope, but once too much Martensite is formed the material behavior changes. Specifically, too much Martensite makes the material brittle. The loads required to deform the Smooth specimens at -100°C are easily higher than 10KN, sometimes higher than 10.5 KN. The high loads required, combined with very low temperatures, induce an increased transformation of the microcrystalline phase. The shape of the Stress-Strain curves is similar to the one obtained by T. Yoshimita and I. Takeshi in the study "*Constitutive modeling of TRIP Steel and its application to the improvement of Mechanical Properties*", where TRIP steels are investigated concerning the fraction of induced Martensite after deformation at different temperatures.

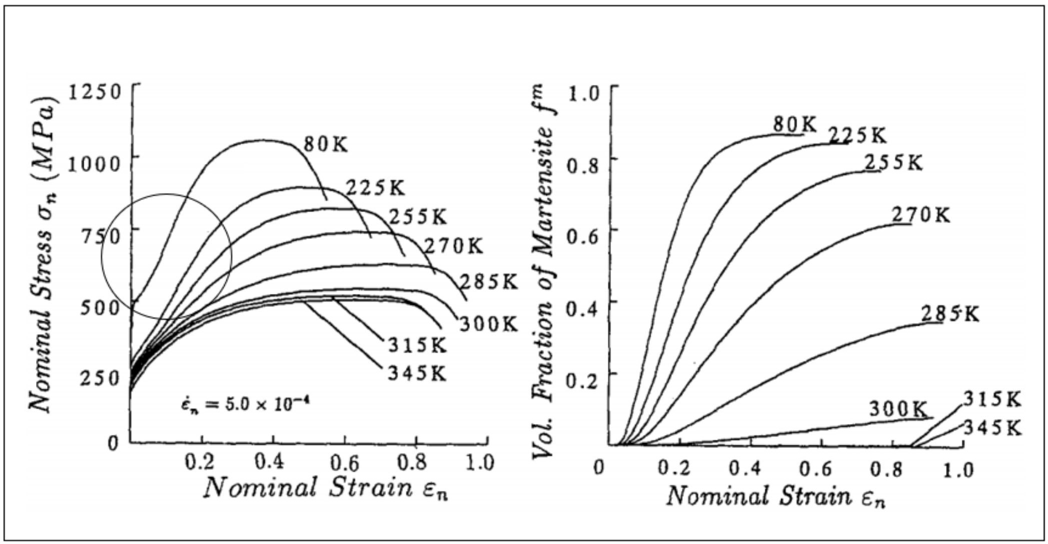

Figure 4.3.2: Nominal Stress and Volume Fraction of martensite vs nominal Strain [1]

The behavior of the TRIP steel studied between 225K (-50°C) and 80K (-193°C), highlighted in the Figure 4.3.2, presents a similar and recognizable slope as the ones seen in the AISI 316 deformed at -100°C. It's also important to highlight that the fraction of induced Martensite increases as the temperature of the test decreases.

This effect is not seen in the test carried out at -50°C because the temperature is not low enough to induce a high transformation of Austenite into Martensite. Just a small percentage of induced martensite is transformed from the Austenite phase. The induced Martensite clearly enhances the mechanical strength of the AISI 316, which can now deform more without reaching failure requiring at the same time a higher load to achieve such Strain.

This phenomenon is only recognizable in the Smooth Sample because the loads required to deform Notched and Shear Samples at -100°C is much lower. Certainly, a certain amount of martensite is induced by the TRIP effect also in the notched and shear specimen, but not enough to drastically change the behavior described by the shape of the Stress-Strain curves.

This effect is easily confirmed by studying the Smooth specimens deformed to UTS, to evaluate their microstructure at the optical microscope and SEM and by quantifying the volume of induced Martensite at different temperatures.

4.4. Evaluation of UTS and Strain at UTS

The main aspect of this thesis was to research if by sub-zero forming the formability of AISI 316 will increase or not. One way to evaluate an improvement of formability is by analyzing the UTS and the Strain correlated at each temperature.

This analysis was done for every sample, and in order to better evaluate the improvement of the formability a normalization of the collected data was done. The normalization was done considering the values collected at room temperature as normalizing constants.

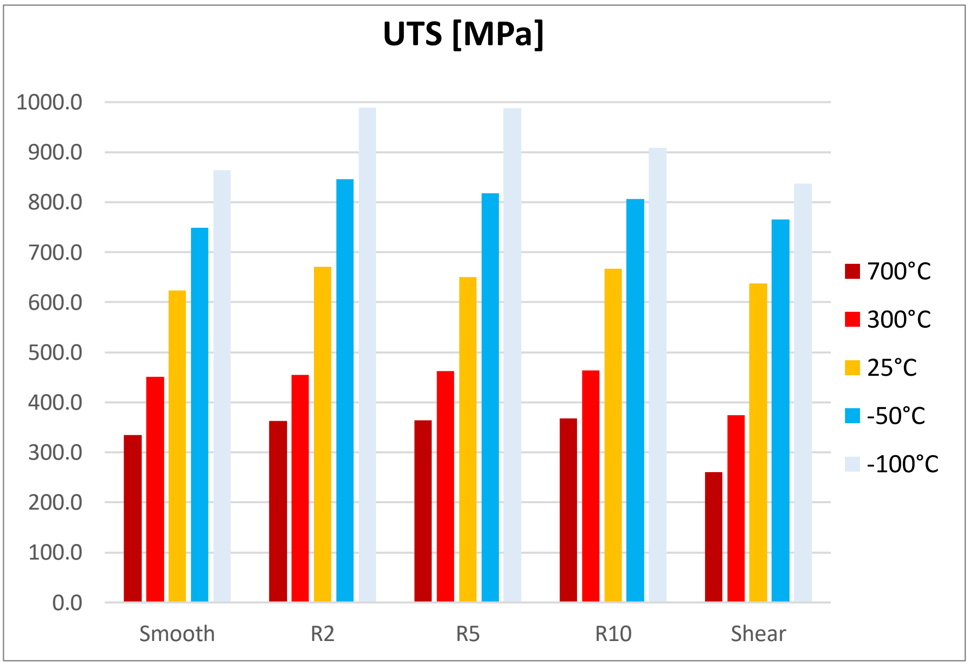

Figure 4.4.1: UTS [MPa] at Different Temperatures – 0° Samples

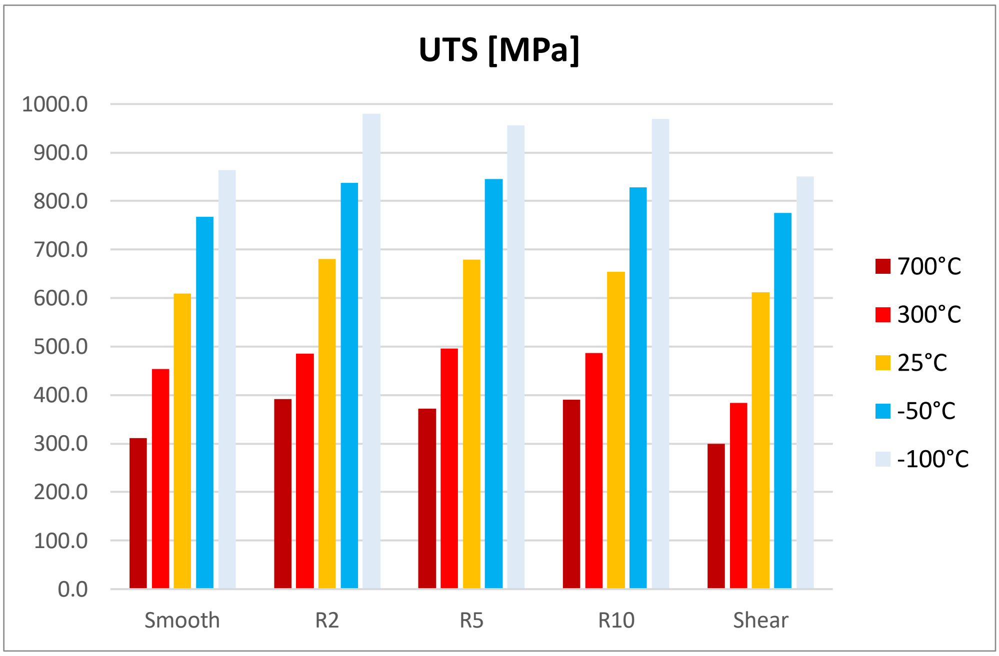

Figure 4.4.2: UTS [MPa] at Different Temperatures – 90° Samples

As can be seen in figures 4.4.1 and 4.4.2 a clear increase in the Ultimate Tensile Strength is obtained by sub-zero forming for each specimen's geometry. The increased UTS is not always correlated with an increased Strain at UTS, as can be seen from the graphs that highlight this specific aspect:

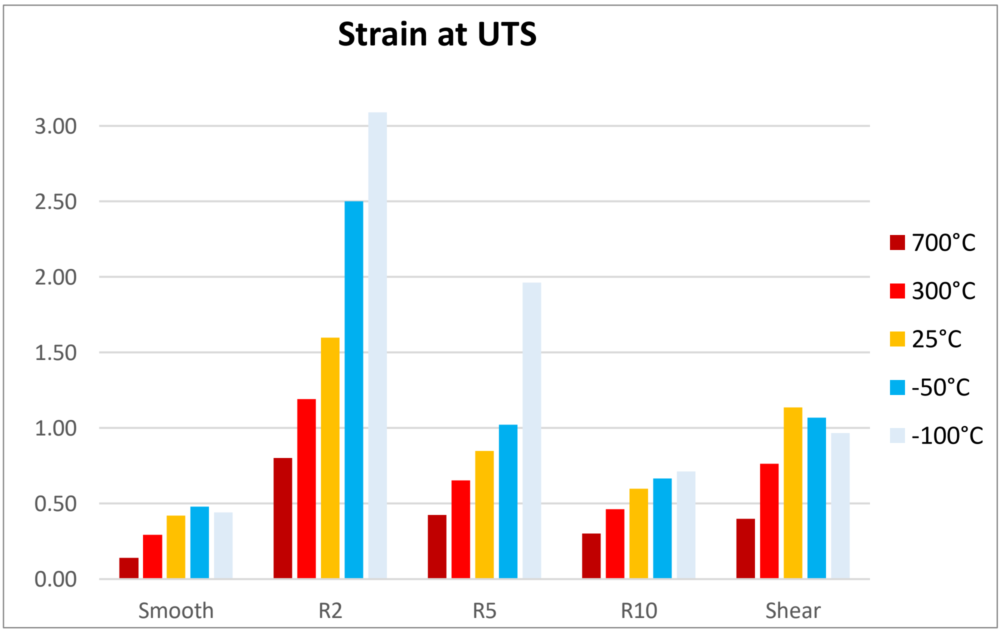

Figure 4.4.3: Strain at UTS at Different Temperatures – 0° Samples

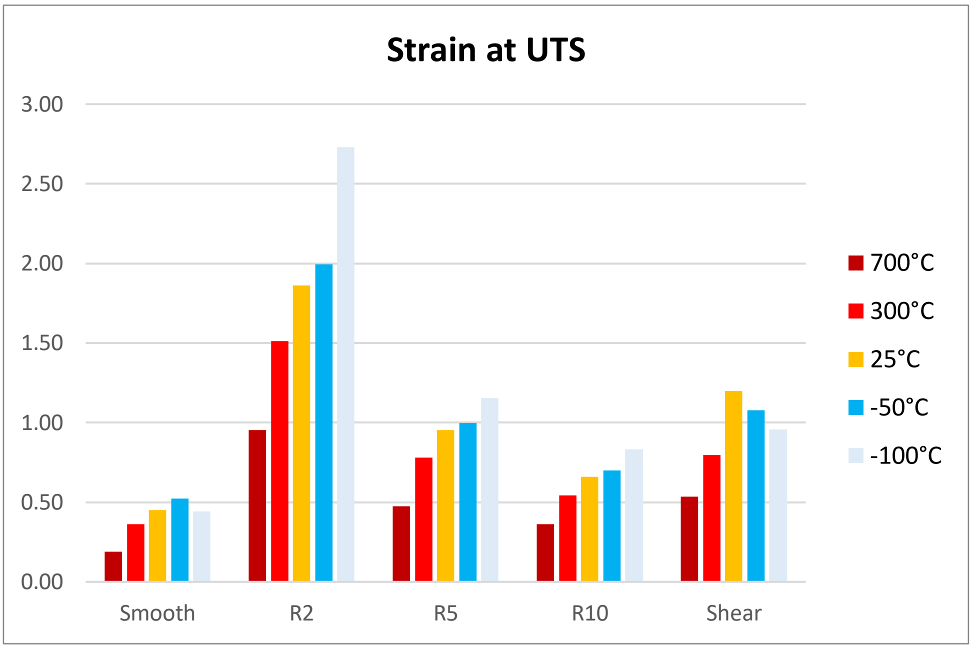

Figure 4.4.4: Strain at UTS at Different Temperatures – 90° Samples

In the histogram proposed, a higher strain at UTS is recorded at -100°C for the notched specimens, while for the shear specimens lower Strain are correlated with lower temperatures. Not considering the shear samples, which geometry highly affect the formability, it is clear that a formability improvement is achieved by forming the material at -50°C.

One aspect that each sample has in common is that by increasing the temperature, the UTS and Strain at UTS decrease. This behavior is known as “Hole of Formability”, where the formability decreases raising the forming temperature until a certain limit at which the formability starts to increase. For the AISI 316 and 316L, the hole of formability is defined in a range of temperatures that go from 300°C to 800°C [2].

The values of UTS and Strain at UTS obtained by sub-zero forming are more easily read by normalizing them:

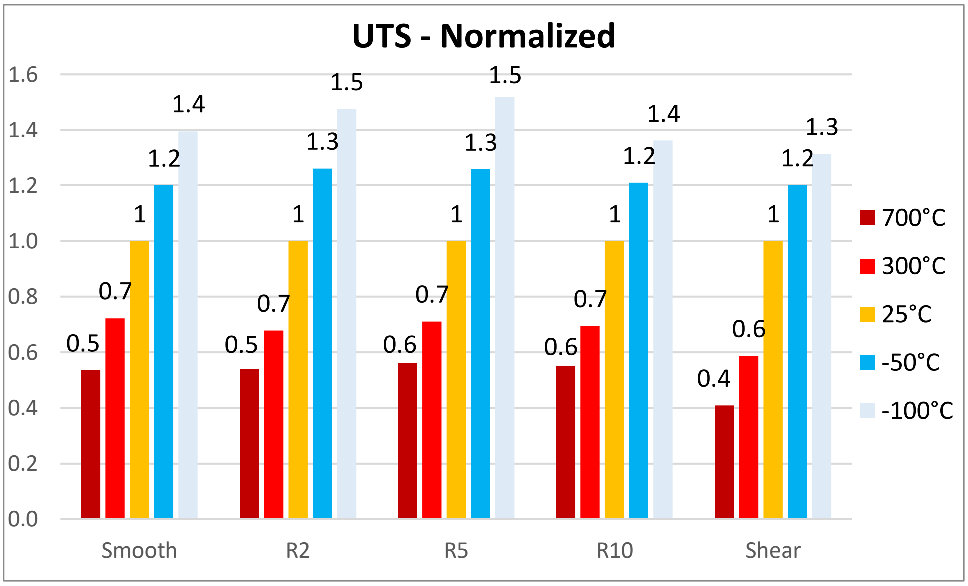

Figure 4.4.5: UTS values Normalized - 0° Samples

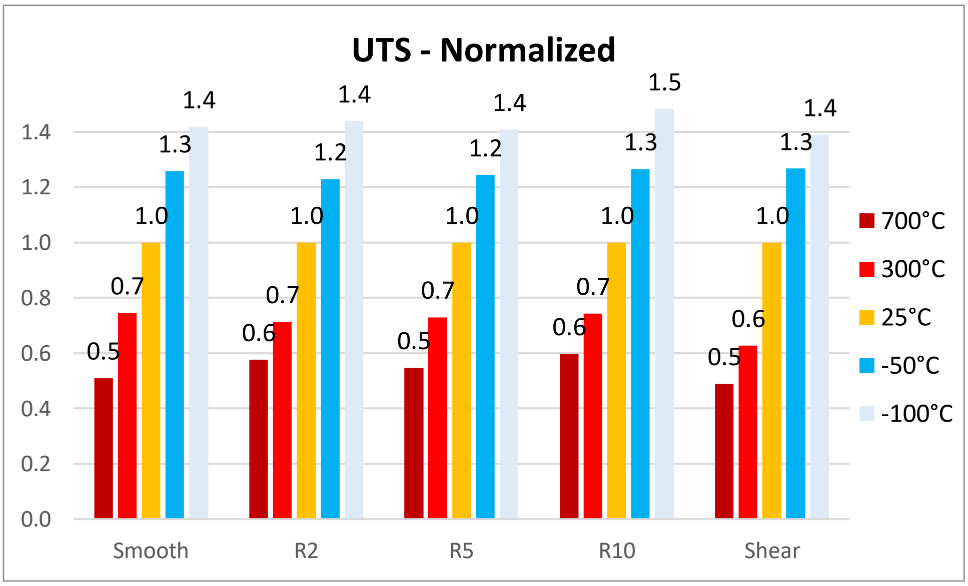

Figure 4.4.6: UTS values Normalized - 90° Samples

Where a percentage value can be obtained. Considering the UTS values at room temperature as the normalizing constant, a 20% to 30% increase in the ultimate tensile strength is seen by forming at -50°C, while a 30% to 50% increase is seen at -100°C. The same behavior is recognized in both the samples cut at different angles to the Rolling Direction.

The values of Strain recorded at UTS appears more interesting when normalized:

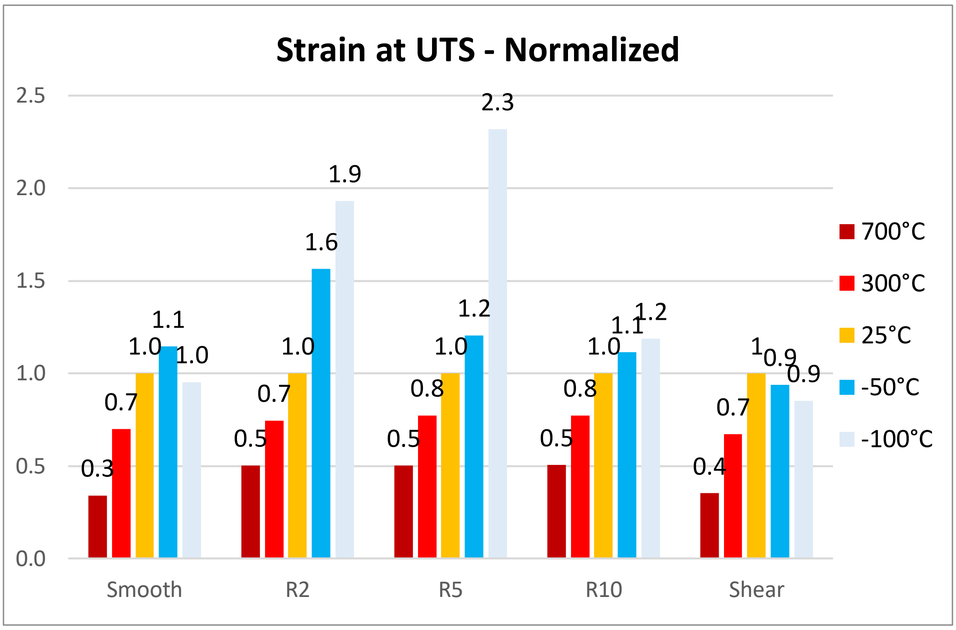

Figure 4.4.7: Strain at UTS normalized - 0° Samples

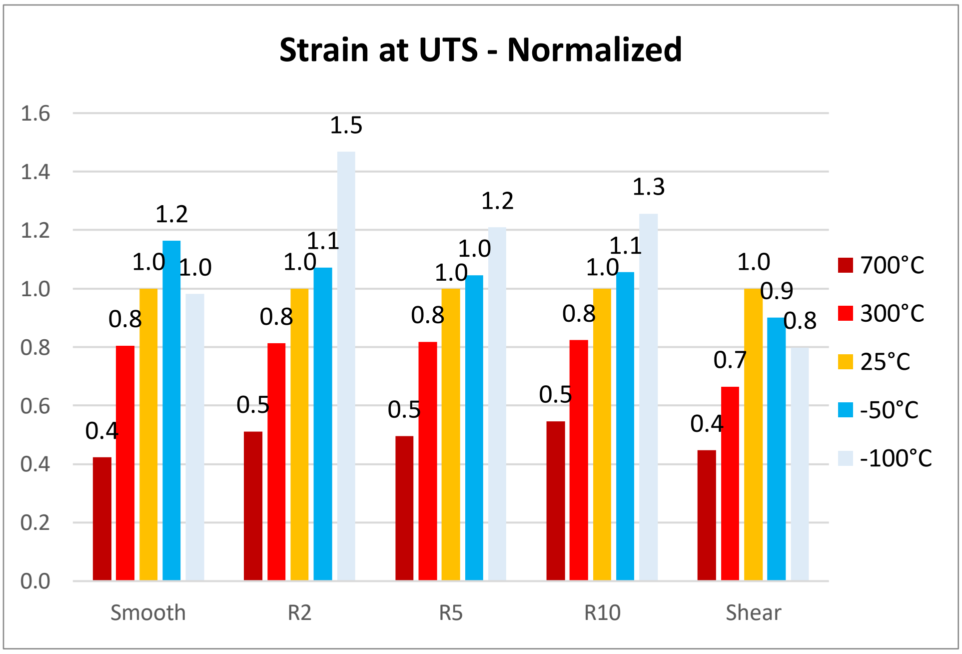

Figure 4.4.8: Strain at UTS normalized - 90° Samples

Where, as with the normalized UTS values, a percentage value is obtained. From the data proposed, sub-zero forming at -50°C can increase the formability of AISI 316 by 10% to 20% as can be seen for the Smooth samples. The behavior of the Smooth samples deformed at -100°C presents, as investigated before, a reduction in the formability that reaches up to 20% less Strain at UTS. For all the notched specimens, sub-zero forming appears to increase the formability. It's important to remember that the engineering Strain calculated is affected by the length of the notched portion.

As the results show, a decrease in formability is achieved by working AISI 316 at 300°C and 700°C, with a reduction in the strain achieved at UTS up to 60%.

4.5. Optical Microscope

Metallography is done to evaluate the microstructure and the different phases of the AISI 316 post-deformation. The samples, cut in order to evaluate the three different directions, are chemically etched to reveal the microstructure. Two different chemical attacks are applied. The first one consists in electrolytically etching the surface with a 10% oxalic acid solution in water which enhances the Austenite phase, used primarily for the "As Build" condition. The second attack consists in submerging the metal in Beraha solution used to enhance the Martensite phase presents in the deformed material.

First of all an evaluation on the "As Delivered" material is done, where an equiassic austenitic structure can be seen in the Normal Direction, as expected. No presence of Martensite phase is seen in the "As Delivered" condition.

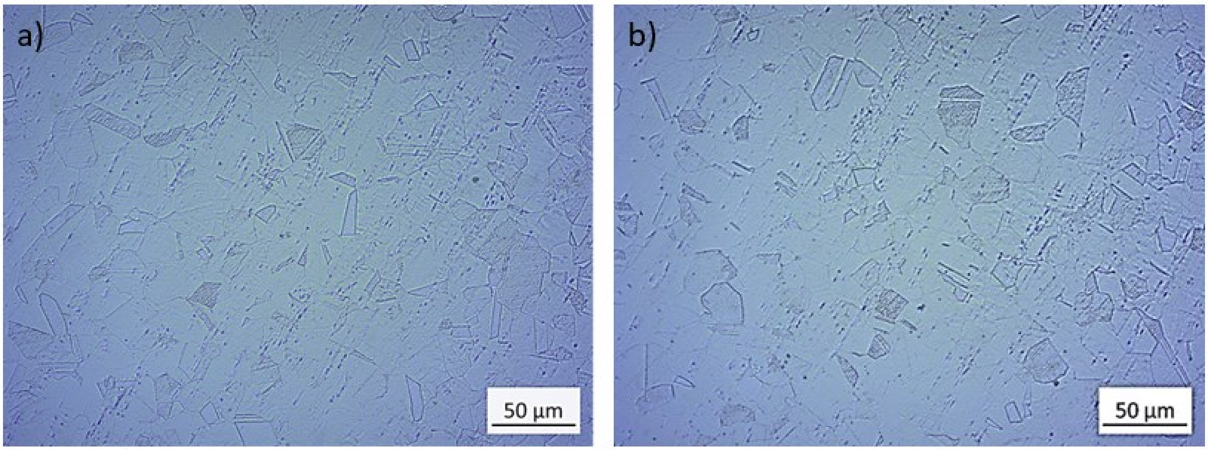

Figure 4.5.1: "As Built" AISI 316 Normal Direction - 10% Oxalic Acid - Magnification 32X

The material is then evaluated through optical metallography post-deformation mainly to evaluate the change in microstructure, using the Beraha Attack and a magnification of 100X. In the Normal Direction a high increase in the Martensite phase is seen in the samples deformed at -50°C and especially at -100°C where the Martensite appears to be the main phase of the steel. No needle-like structure of Martensite is highlighted by the chemical attack in the 300°C and 700°C specimens. In both the Rolling and Transverse Directions the bands caused by the rolling of the stainless steel sheets and by the tensile load, as well as the Martensite formation at sub-zero temperatures can be seen.

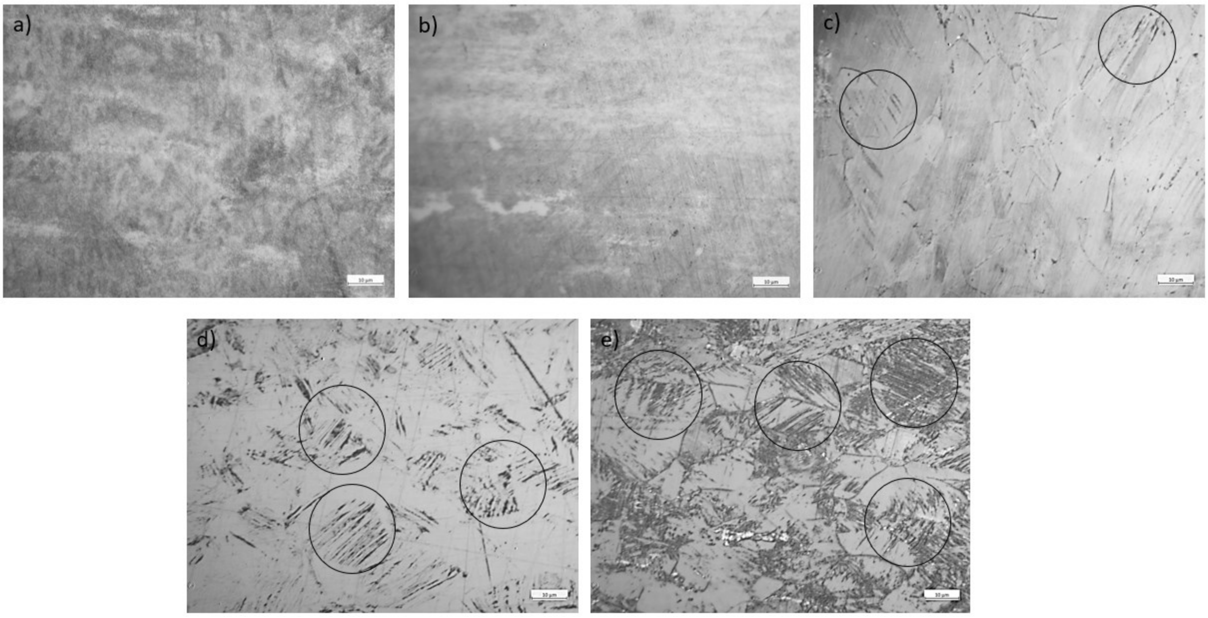

Figure 4.5.2: Normal Direction, Samples deformed to UTS -
Beraha Attack – 1000X Magnification - a) 700°C, b) 300°C, c) 25°C, d) -50°C, e) -100°C
Martensite highlighted in each image

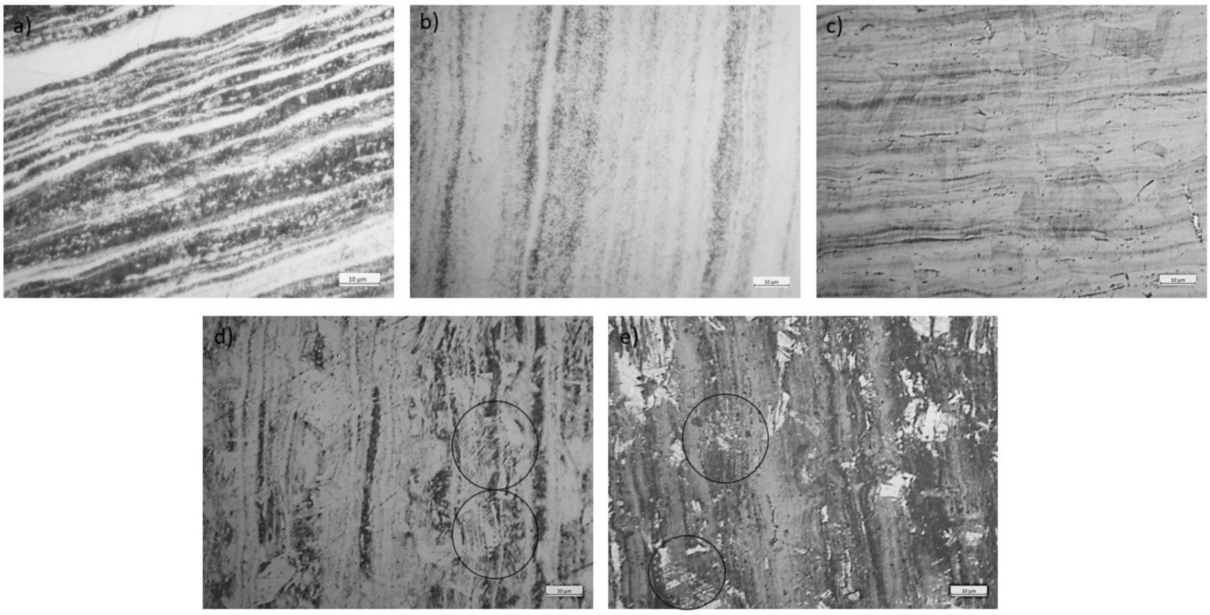

Figure 3.5.3: Rolling Direction, Samples deformed to UTS -
Beraha Attack – 1000X Magnification - a) 700°C, b) 300°C, c) 25°C, d) -50°C, e) -100°C
Martensite highlighted in each image

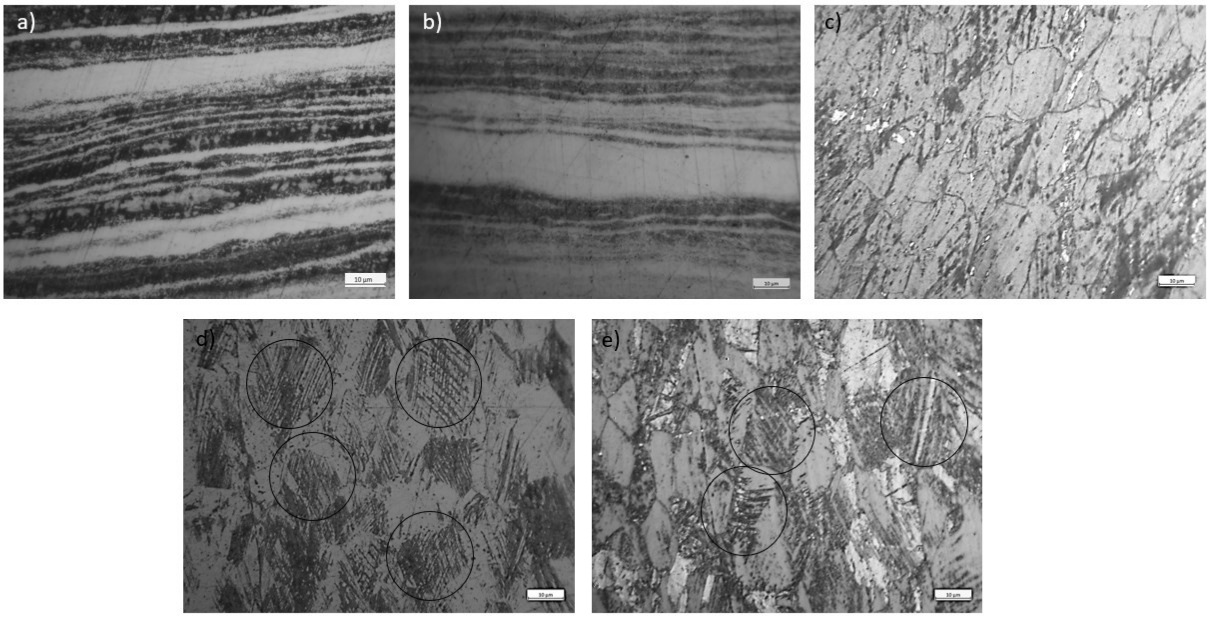

Figure 4.6.4: Transverse Direction, Samples deformed to UTS - Beraha Attack – 1000X Magnification - a) 700°C, b) 300°C, c) 25°C, d) -50°C, e) -100°C Martensite highlighted in each image

4.6. Vickers Hardness Test

The hardness of the AISI 316 was evaluated with Smooth samples, at first in the "As Delivered" condition, used to define the hardness of the material in its pristine form. Secondly, the material's hardness was quantified after deformation at different temperatures. The smooth samples were deformed until UTS at 700°C, 300°C, 25°C, -50°C, and -100°C. it's important to say that just the 0° samples were studied through Vickers Hardness test.

The Vickers test was performed using a 50 grams weight applied to the surface for 15 seconds. The output values of the test were calculated using the formula:

$$\mathrm{HV} = 1854.4 \times \frac{P}{d^2}$$

Where P is the Weight of the indenter (in this case 50 grams), d is the average diagonal of indentation (measured in micron):

$$d = \frac{d_1 + d_2}{2}$$

As said previously the test consists in creating indentures on the surface of the material through a pyramidal indenter. The mark that the indenter leaves on the surface describes the hardness of the material. The smaller the indentation the higher the hardness. To obtain a statistical distribution of the values, five indentations were taken in consideration on each surface. The average of the values obtained was calculated, as well as their standard deviation. The test was done on each surface of the samples deformed to UTS so on the Normal, Rolling and Transverse Direction.

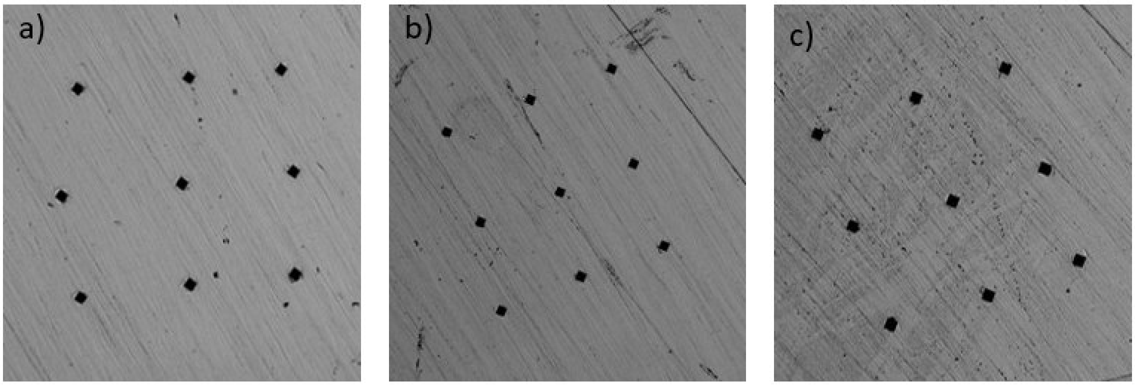

Figure 4.6.1: Indentations for the Vickers Test - 20X Magnification
a) Normal Direction, b) Rolling Direction, c) Transverse Direction

The average values with their standard deviation were inserted in a series of histograms in order to evaluate the differences between the hardness of AISI 316 calculated after deformation at different temperatures. A table with all the average values of hardness calculated after the Vickers Hardness test is presented below.

	As Delivered	**25°C UTS**	**-50°C UTS**	**-100°C UTS**	**300°C UTS**	**700°C UTS**
HV - **ND**	128.8	265.8	267.8	325.6	204.6	190.7
std HV	4.1	8.4	2.4	7.0	16.1	4.2
HV - **RD**	127.1	235.7	262.9	309.6	232.7	201.9
std HV	5.4	4.6	9.4	8.3	12.2	8.7
HV - **TD**	135.4	246.8	276.7	316.5	217.3	201.1
std HV	2.7	7.1	9.3	5.6	5.2	9.5

Table 4.6.1: Average Data of the Vickers Hardness Test with Standard Deviation

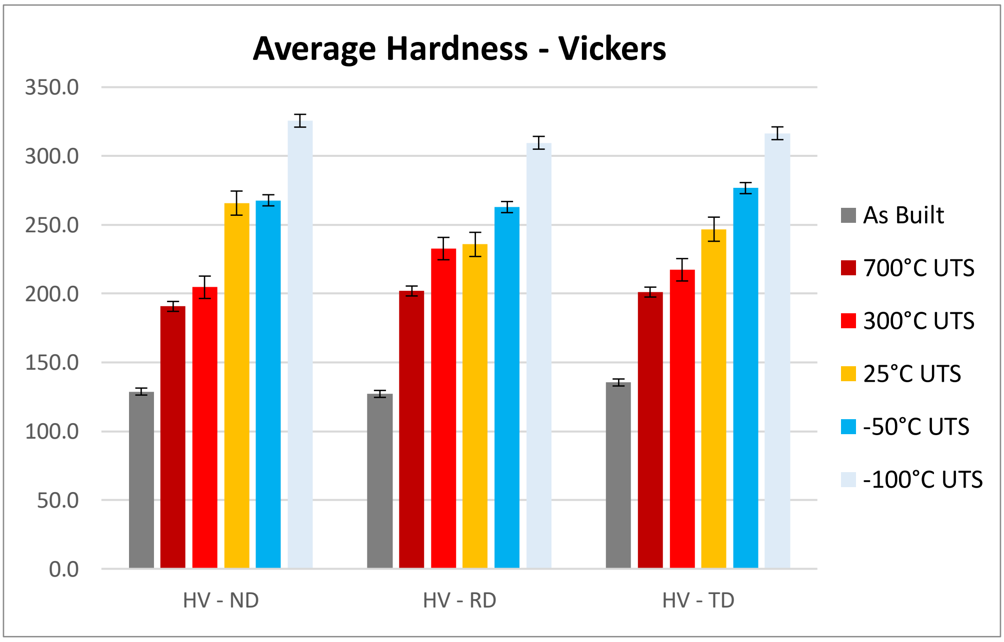

Figure 4.6.2: Average Vickers Hardness in Comparison

As it can be seen by the graph proposed the hardness of the material increases with the decreasing of the temperature at which the deformation is carried out. A normalization of the values was calculated to quantify the improvement of the hardness. The normalizing constant is the hardness value calculated in the "As Delivered" condition.

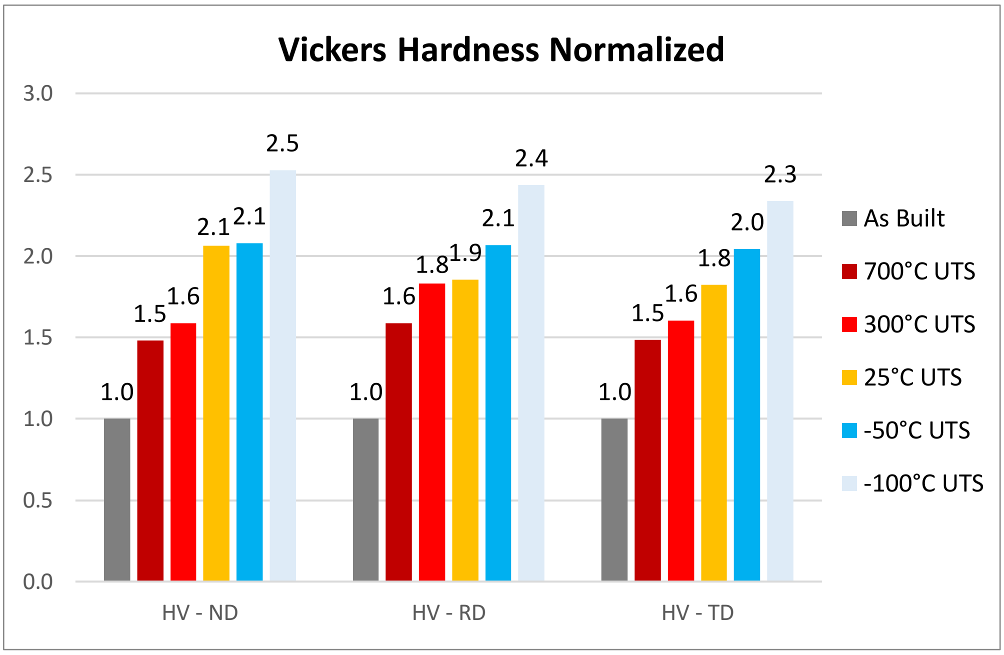

Figure 4.6.3: Normalized Vickers Hardness in correlation to the "As Built" condition

The increase in hardness is strictly correlated with the quantity of induced Martensite by plastic deformation. Increasing the temperature at which the tensile tests are carried out induces less Martensite formation due to TRIP effect. As said previously Martensite strongly increases the hardness of the material. Considering the “As Delivered” condition it is clear that an increase in hardness is due also to the strain hardening process introduced in Chapter one caused by the tensile load applied in the uniaxial tensile test. The normalization of the values of the Vickers Hardness highlights this aspect. A 130% to 150% increase in hardness is seen in the -100°C specimens, while a 100% to 110% increase is seen in the -50°C samples.

4.7. SEM

In this chapter the results and images acquired by the SEM are discussed. The samples brought to UTS are studied, once embedded in resin, polished, and etched with Beraha solution. Just the surface on the Normal Direction is studied due to the difficulty to apply the copper tape required for the SEM to the narrow surfaces of the Transverse and Rolling Directions.

4.7.1. Normal Direction and Induced Martensite

From the series of images proposed it can be clearly seen that a change in phase is induced in the samples deformed at sub-zero temperatures. The images taken of the Normal Direction of the smooth samples are taken with the ETD detector which enhances the topography of the metal at a magnification of 1000X. In the sub-zero deformed samples the presence of the Martensite phase is highlighted by the needle-like microstructure also described in Chapter one. This particular type of microstructure is not found in the samples deformed at higher temperatures.

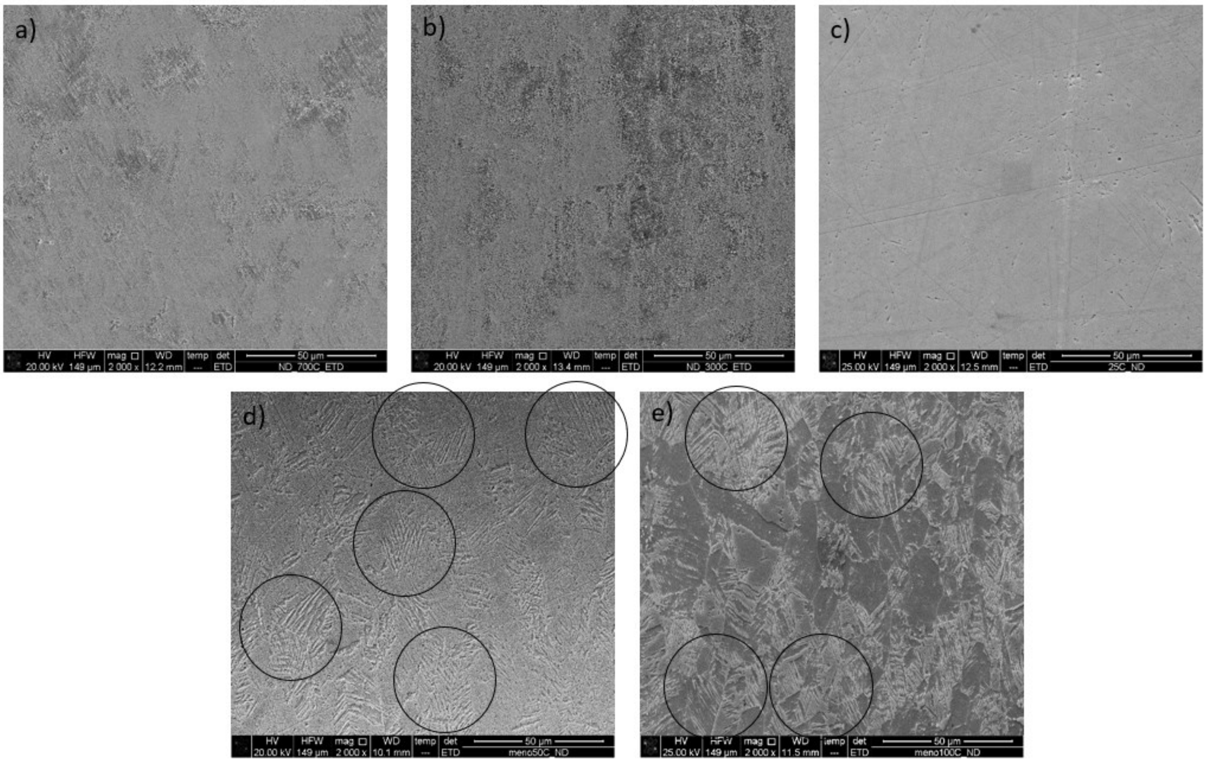

*Figure 4.7.1: SEM Samples deformed to UTS - 1000X Magnification - ETD Detector - Beraha Attack. a) 700°C, b) 300°C, c) 25°C, d) -50°C, e) -100°C
Martensite highlighted in each image*

This aspect of the material can better be seen with the BSED detector of the SEM, which highlight the differences in phases in the metal. With this detector it can be seen that for the samples deformed at 700°C and 300°C no Martensite phase is induced, whether for the specimens deformed at -50°C and -100°C more and more Martensite is induced by the TRIP effect.

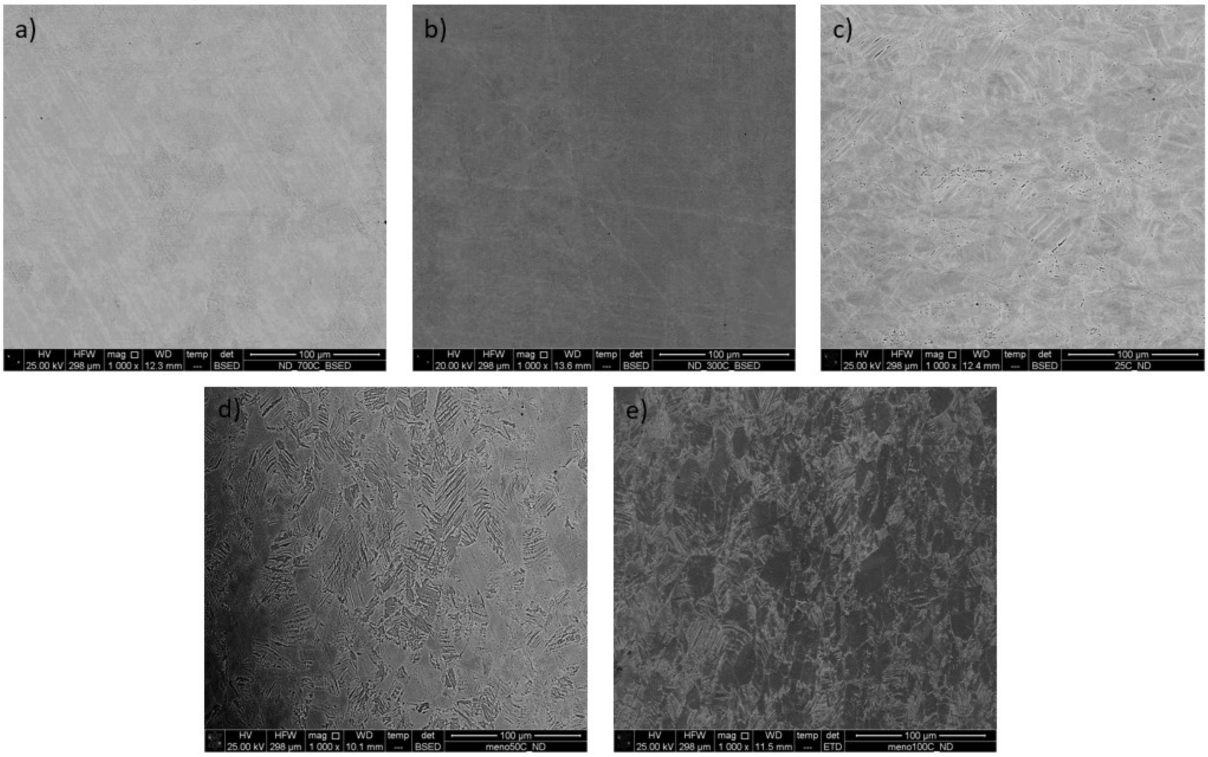

Figure 4.7.2: SEM Samples deformed to UTS - 1000X Magnification - BSED Detector - Beraha Attack. a) 700°C, b) 300°C, c) 25°C, d) -50°C, e) -100°C

To quantify the percentage of Martensite phase the SEM images of the samples deformed to UTS at different temperatures are analyzed. The SEM images are evaluated through a script developed in MATLAB. Specifically, the SEM image is passed through a high-pass filter in order to remove possible shadows created by the SEM itself, as it can be seen for example in the image 4.7.2 for the sample deformed at -50°C. Subsequently the image is passed through an Otsu's threshold to obtain a binary image characterized by only black and white pixels. A median filter is then applied to the black and white image obtained to remove possible image noise. The percentage of Martensite phase present in the sample is calculated by counting the black pixels. The more black pixels are present in the image the more Martensite is present in the deformed metal. The data are then put in a graph to evaluate the evolution in the Martensite phase.

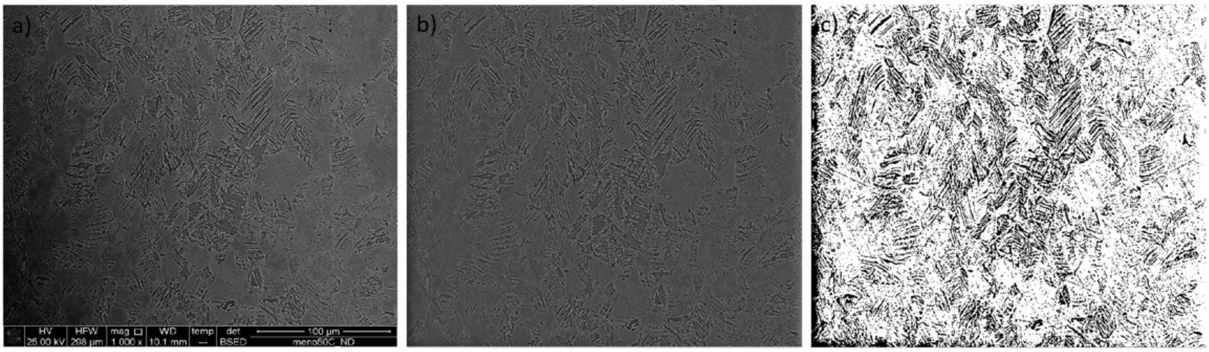

Figure 4.7.3: Steps of the MATLAB Script. a) Original SEM image, b) Same image after High-Pass Filter and Median Filter, c) After OTSU's Threshold

By the graph proposed an increase up to 50% in induced Martensite is found in the samples deformed at -100°C, while a 20% in Martensite is seen in the specimens deformed at -50°C. The TRIP effect does not come into effect for the samples deformed at higher temperatures, where the induced Martensite is near to 0%.

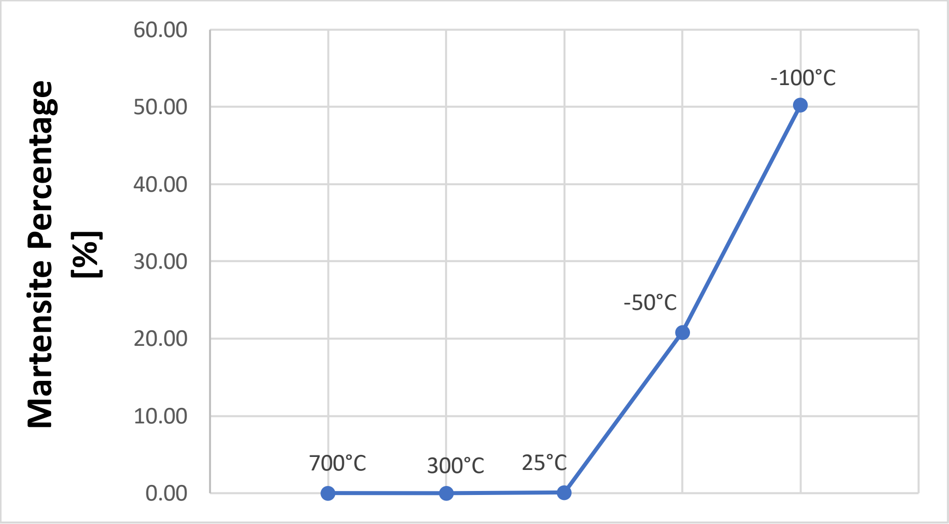

Figure 4.7.4: Martensite's Percentage in correlation to the Temperature

4.7.2. Surface Fracture

SEM was used also to evaluate the surface fracture of the samples brought to failure at the range of temperature studied. The ETD detector was used to enhance the topographical properties of the fractures whereas different magnifications, 250X, 500X, 1000X, 2000X, were used to better understand the fracture itself. Only the 0° Samples brought to failure were studied.

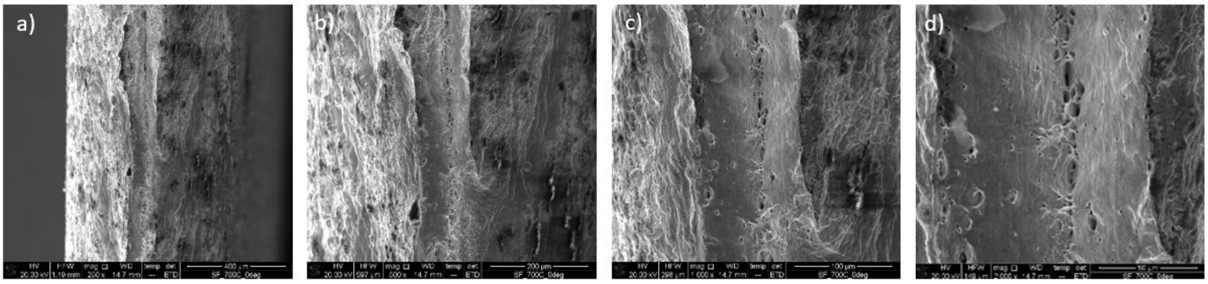

Figure 4.7.5: Surface Fracture at 700°C – ETD Detector. Different Magnifications: a) 250X, b) 500C, c) 1000X, d) 2000X

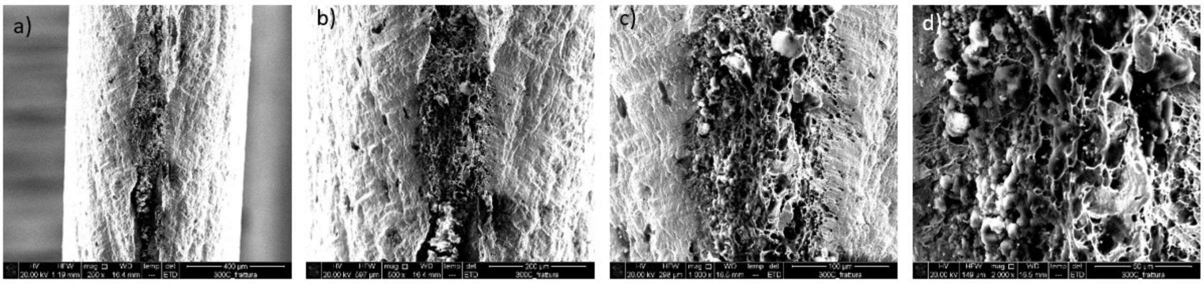

Figure 4.7.6: Surface Fracture at 300°C – ETD Detector. Different Magnifications: a) 250X, b) 500C, c) 1000X, d) 2000X

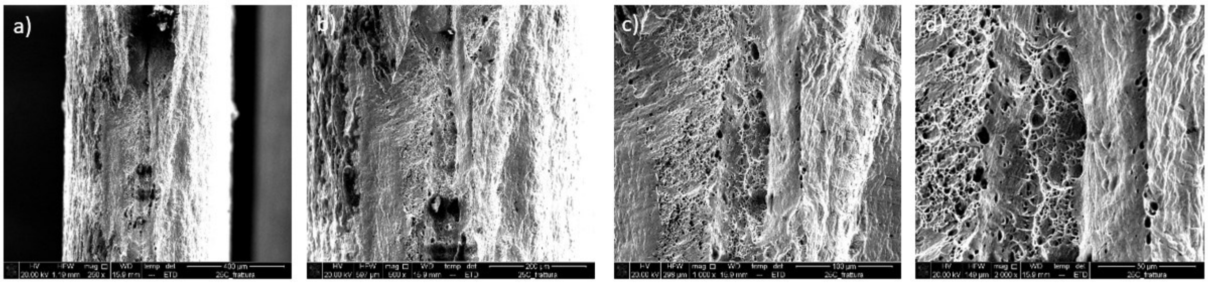

Figure 4.7.7: Surface Fracture at 25°C – ETD Detector. Different Magnifications: a) 250X, b) 500C, c) 1000X, d) 2000X

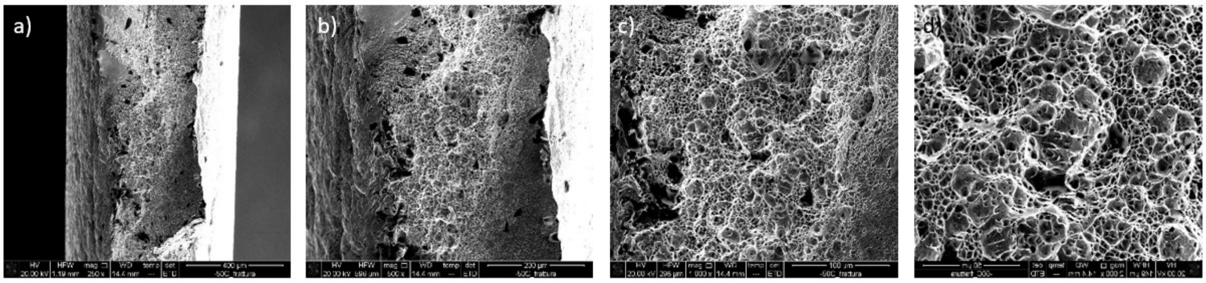

Figure 4.7.8: Surface Fracture at 700°C – ETD Detector. Different Magnifications: a) 250X, b) 500C, c) 1000X, d) 2000X

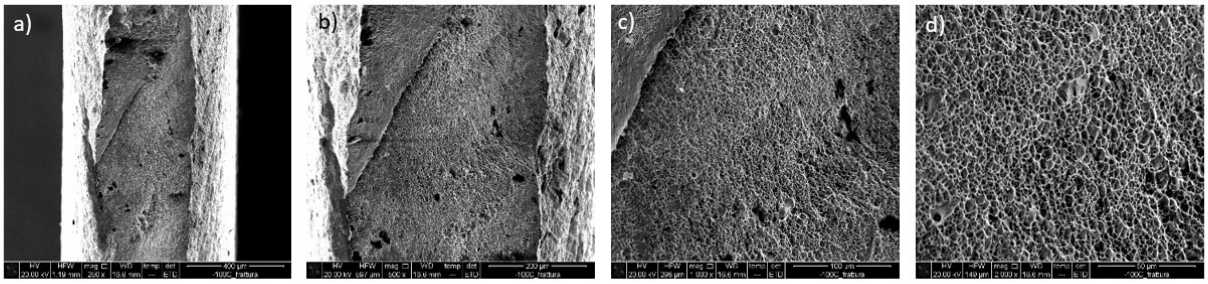

Figure 4.7.9: Surface Fracture at -100°C – ETD Detector. Different Magnifications: a) 250X, b) 500C, c) 1000X, d) 2000X

From the proposed images, an evolution of the surface fracture can be seen. For the samples deformed at 25°C, 300°C and 700°C a ductile behavior is seen in the shape of the fracture. At higher magnification (1000X and 2000X), specifically for the 300°C and 25°C samples, a high inhomogeneity in the surface can be seen. Dimple fracture is nonetheless found in every fractured samples. At sub-zero temperatures, the dimple-like microstructure is clearly highlighted in the 1000X and 2000X images, where also a better homogeneity in the overall structure is found. The dimples in question decrease in size as the temperature decreases below 0°C due also to the higher tensile loads required to fracture the samples. A ductile behavior can be found in the samples brought to failure at -50°C and -100°C.

4.8. XRD

X-Ray diffraction was done on the surfaces of the Smooth samples brought to UTS to

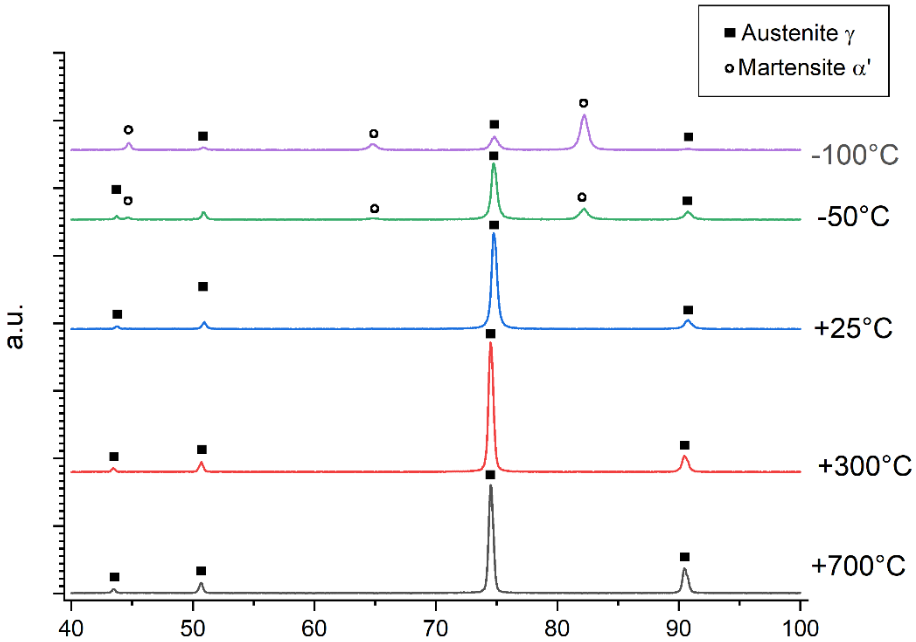

Figure 4.8.1: XRD Analysis of the Smooth Samples

evaluate the elements and phases characterizing them. The XRD evaluation highlighted an increase in the Martensite phase in the samples deformed at sub-zero temperatures, confirming the results achieved by optical microscopy and SEM. In the specimens deformed at 25°C, 300°C, and 700°C no Martensite is found by the XRD. This can be explained by the limit of detection of the XRD which ranges between 2% and 5%. From the evaluation of the Martensite volume presents in the samples deformed at 25°C and higher the Martensite phase appears however to be less than 1%.

4.9. Corrosion Tests

Finally, Corrosion tests were done on the samples brought to UTS at different temperatures to evaluate their corrosion resistance. Corrosion currents and potentials were graphically extrapolated with Tafel's method. As the graph and table proposed indicate, the corrosion resistance decreases in the samples deformed at sub-zero temperatures while a better corrosion resistance is found in the specimens deformed at room temperature and above. This behavior can be explained by the fact that Martensite has a worse corrosion resistance than its counterpart Austenite, which characterizes the metal specifically in the "As Delivered" condition. It's important to remember that AISI 316 has an excellent corrosion resistance, specifically to pitting. The presence of induced Martensite due to TRIP effect worsen the corrosion resistance of the metal. The more Martensite is present the worse its corrosion resistance. This behavior can be seen specifically by the graph proposed in Figure 4.9.1, where the passivation plateau is better for the 25°C and higher temperatures samples, because it requires lower current density to become stainless.

Temp at UTS	**E_{corr} (V)**	**I_{corr} (A/cm^2)**
-100°C	-0.45	$2x10^{-7}$
-50°C	-0.39	$7x10^{-7}$
25°C	-0.32	$2x10^{-8}$
300°C	-0.38	$9 x10^{-9}$
700°C	-0.35	$1x10^{-8}$

Table 4.9.1: Results from Corrosion Test

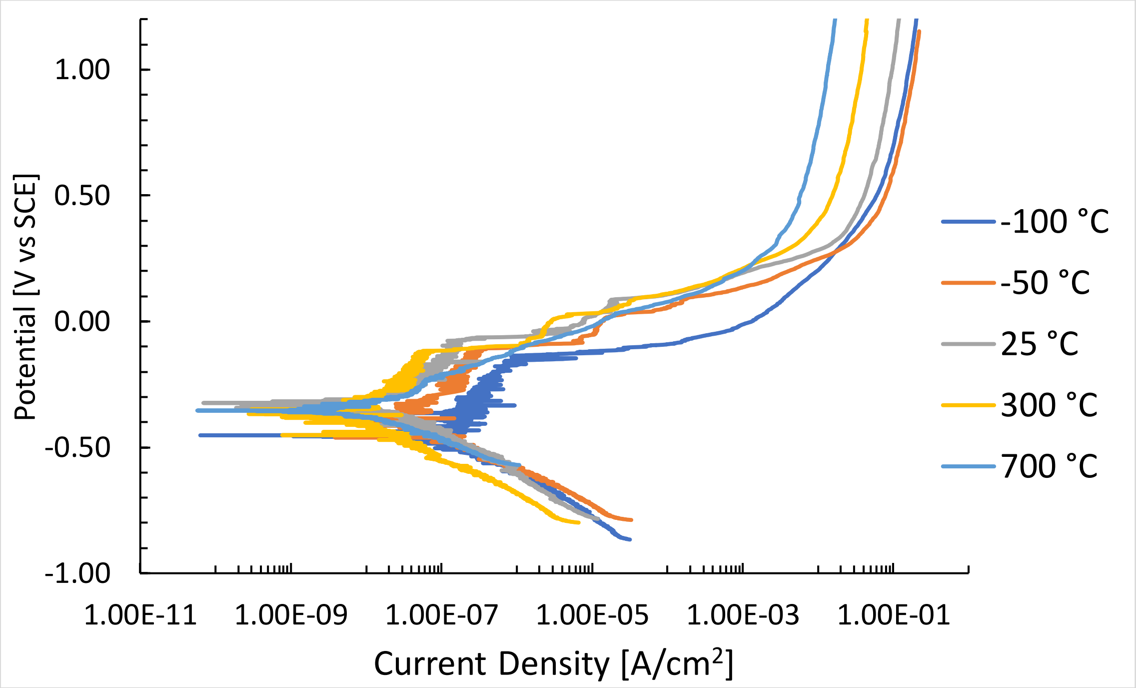

Figure 4.9.1: Results of the Corrosion Test on Smooth Samples at different Temperatures

Bibliography and Sitography

1. Tomita, Yoshihiro, and Takeshi Iwamoto. "*Constitutive modeling of TRIP steel and its application to the improvement of mechanical properties.*" International Journal of Mechanical Sciences 37.12 (1995): 1295-1305.
2. https://www.northamericanstainless.com/wp-content/uploads/2010/10/Grade-316-316L.pdf

5. Outcome of the Simulations

In this chapter I will discuss the main results of the numerical model developed in LS-DYNA. As said previously in Chapter 3 the main focus was done on three main aspects:

1. Contour plots of the Real Stress, highlighting where the main stresses concentrate for each sample's geometry;
2. True Stress – Strain curves and whether they reflect the real behavior of AISI 316 after tensile load;
3. Load to Run length graphs to evaluate the response of the simulation.

In the simulations developed the samples were brought to fracture by inserting the value of Strain at failure in the description of the material used. From these simulations an evaluation of the Real Stress-Strain curves and peak values of Stress were done, as well as an analysis of the Load to Run Length graphs. Specifically, the outcome of the Load to Run Length graphs of LS-DYNA were normalized in order to successfully compare them with the real Load to Run Length curves of the tensile test, output of the load frame MTS-322. For the True Stress-Strain curves the shear specimens are not taken into consideration.

5.1. Contour Plots

In this subchapter the contour plots for each geometry are taken into consideration, focusing on the peak Stresses calculated by the simulation. The contour plots are recorded just before failure of the specimen to obtain the maximum value of Real Stress reached for each geometry. As it can be seen by Figure 5.1.1, the Stresses are concentrated in the Smooth samples on all the linear region, while on the notched specimens the Stresses are concentrated in the notched part. From Figure 5.1.2 it can be seen that the Real Stresses in the shear specimen concentrates in the notched regions as well. Remembering that, it can be noted that the values calculated by the tensile test from the MTS-322 are similar to the outcome of the simulations.

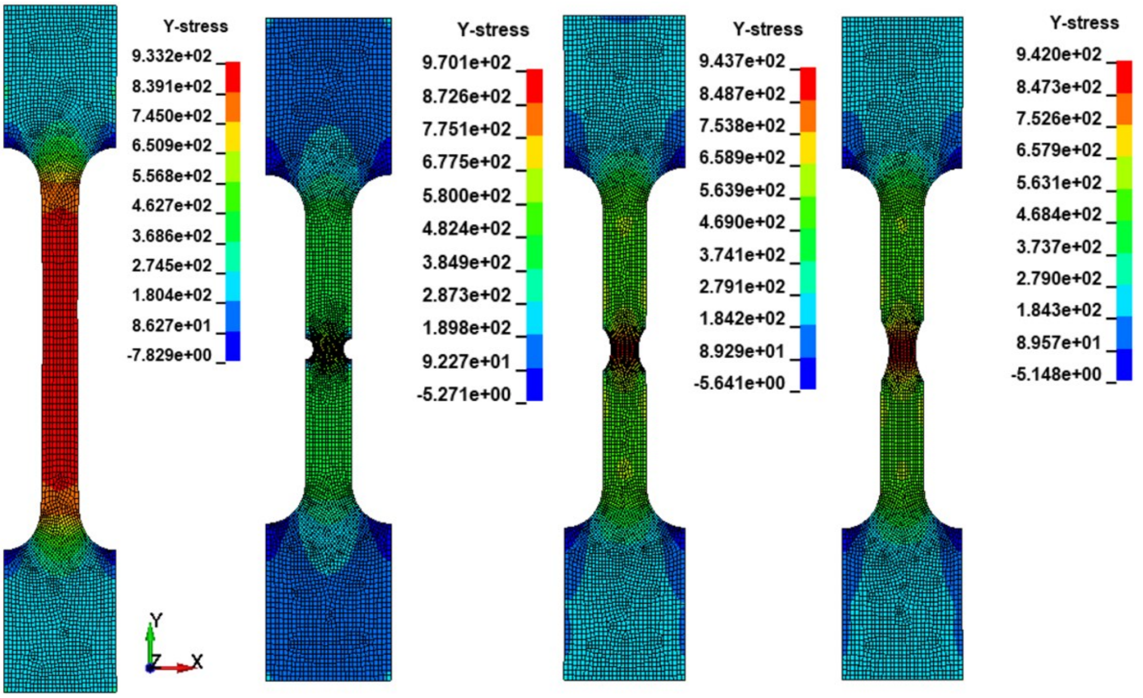

Figure 5.1.1: Contour Plots of Y-Stress for each geometry

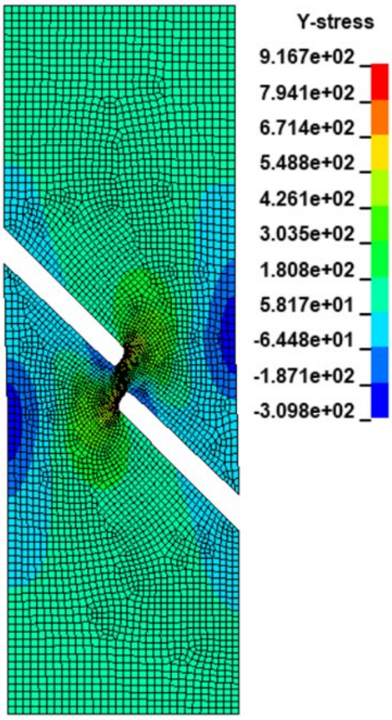

Figure 5.1.2: Contour Plot of Y-Stress for Shear Geometry

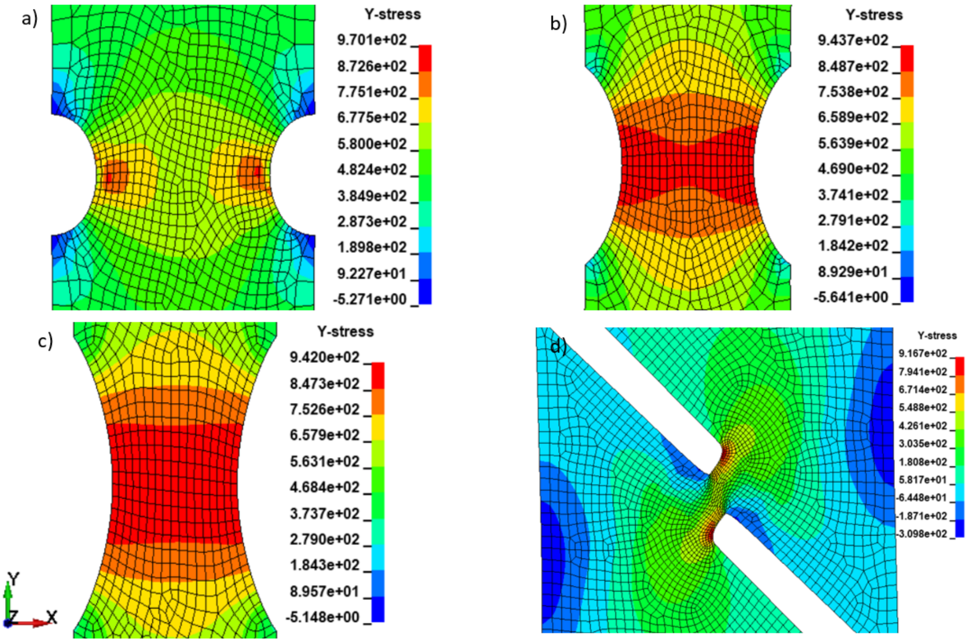

Figure 5.1.3: Focus on Stresses on Notched and Shear Samples.
a) R2 Notched, b) R5 Notched, c) R10 Notched, d) Shear

Geometry	UTS – **LS-DYNA Values** [MPa]	UTS – **Real Values** [MPa]
Smooth	933.2	1025.7
R2	970.1	998.7
R5	943.7	979
R10	942	1011.6
Shear	916.7	1095.6

Table 5.1.1: UTS [MPa] Values

5.2. True Stress-Strain Curves

The graphs proposed in Figure 5.2.1 highlight the similarity between the simulations and the tensile tests done with the MTS-322 frame load. As said in the previous subchapter the UTS reached in the simulations is similar to the one found in reality, as well as the strain at which the sample reaches failure. Both the elastic and plastic region of the True Stress-Strain curves are well described by the LS-DYNA model.

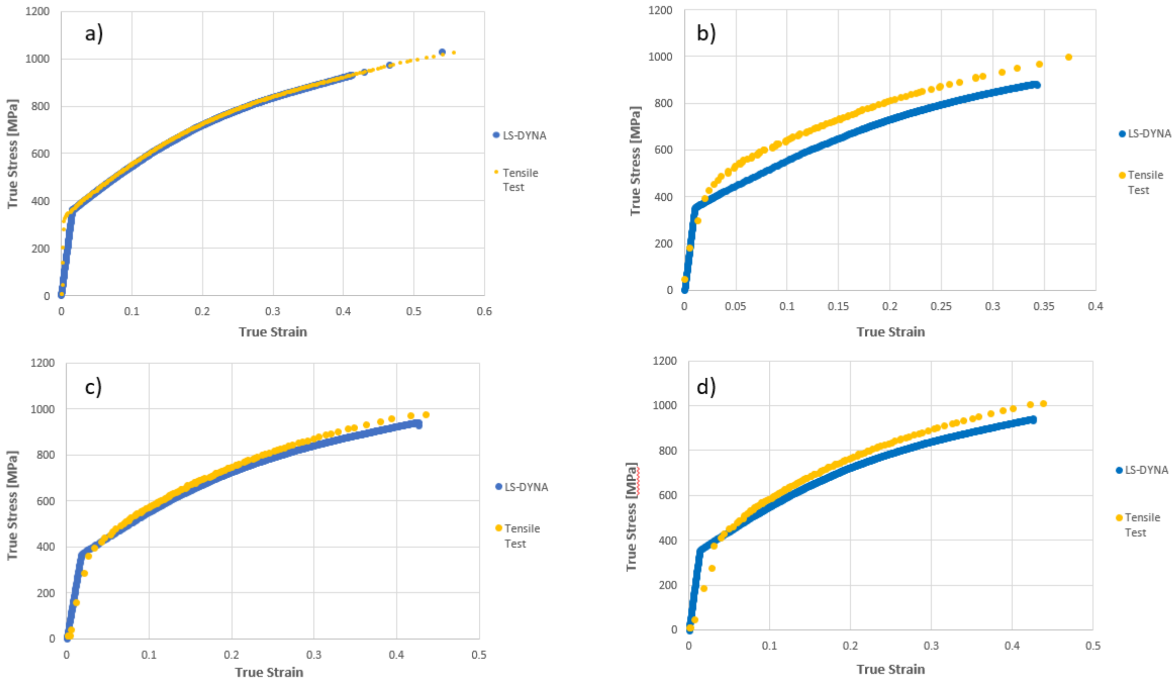

Figure 5.2.1: Simulations and Tensile Test True Stress-Strain Curves in relation. a) Smooth Sample, b) R2 notched, c) R5 Notched, d) R10 Notched

5.3. Load to Run Length Graphs

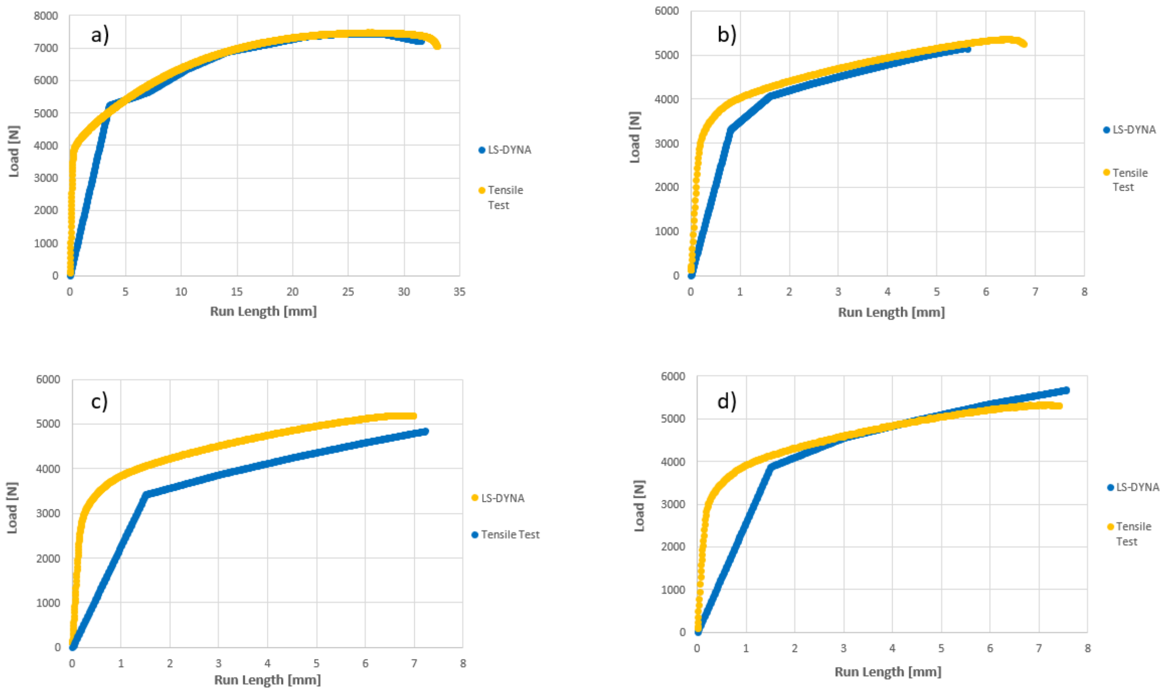

Figure 5.3.1: Load to Run-Length graphs for each geometry. a) Smooth, b) R2 Notched, c) R5 Notched, d) R10 Notched

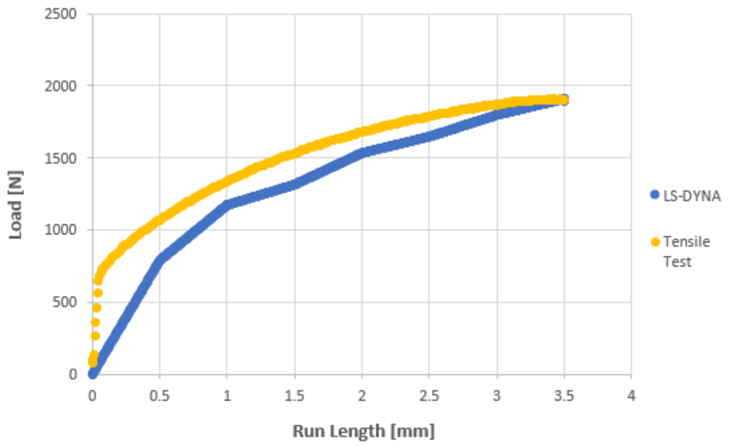

Figure 5.3.2: Load to Run-Length graph for the Shear geometry

As proposed by the graphs in Figure 5.3.1, the Load to Run Length curves, once the Run Length is normalized, appears to have similarities, specifically for the Smooth, R5 and R10 notched. The main similarity is the Load applied to deform the samples and the overall shape of the curves.

For the R2 Notched and the Shear sample the load applied by the LS-DYNA model appears however to be lower than their real counterpart.

Geometry	**Maximum Load** applied in **LS-DYNA** [N]	**Maximum Load** applied by **MTS-322**
Smooth	7453.8	7490.5
R2	5173.716	5364.2
R5	4956.9	5203.1
R10	5680	5338.5
Shear	1910.3	1912.2

Table 5.3.1: Values of Maximum Load reached by the LS-DYNA model and by Tensile Test

6. Conclusions

In this final chapter the results of all the analysis and evaluation done in this thesis for the AISI 316 stainless steel will be discussed.

From the uniaxial tensile tests carried out at different temperatures an improvement in formability is seen in the sample deformed at sub-zero temperatures. This improvement, strictly correlated with an increase in the mechanical properties of the material itself, is confirmed by the level of strain reached at UTS at -50°C and at -100°C. Another aspect correlated to the increase of the mechanical properties of AISI 316 was that the Stresses achieved were higher at sub-zero temperatures, as well as the Loads required to bring the specimen to failure. This improvement in formability is confirmed first of all for all the notched specimens, where an increase in strain reached at UTS is seen firstly in the -50°C samples and then in the -100°C ones. For the Smooth samples it is clear that a formability improvement is achieved in -50°C, whereas at -100°C the change in the predominant crystalline phase of the material strongly modify the behavior of the AISI 316 into a more fragile one. From these results the-50°C temperature is considered as an interesting forming temperature for this stainless steel in order to achieve a better formability correlated with better mechanical properties. At -100°C the change in crystalline phase induced by the TRIP effect deteriorates the ductile behavior of the AISI 316, decreasing at the same time its formability.

The analysis at optical microscope and at SEM done on the Smooth samples brought to UTS at different temperatures highlight a change in phase in the microstructure of the metal Specifically the formation of induced Martensite due to TRIP effect increases with the decreasing of the test's temperature. A high formation of induced Martensite, consisting of nearly 70% of the volume, is indeed observed in the samples deformed to UTS at -100°C. In the Specimens deformed to UTS at -50°C just 20% of induced Martensite is found. In the samples formed at higher temperatures (25°C, 300°C, and 700°C) little to no Martensite is noticed. From these analyses it clearly appears that it's the formation of induced Martensite that enhances the mechanical properties correlated to the formability behavior of AISI 316. A right amount of induced Martensite can indeed highly enhance the formability of the metal, whether too Martensite actually reduces it due to the fragile behavior of the Martensite itself.

The Hardness of the Smooth samples brought to UTS at different temperatures is then investigated through Vickers Hardness Test, highlighting a high increase of Hardness specifically in the sub-zero samples due to the induced Martensite evaluated previously. An increase in hardness is observed also in the samples worked at higher temperatures due predominantly to strain hardening.

Consequently, XRD analyses confirms what was observed through optical microscope and SEM, which was a change in phase in the crystalline structure of AISI 316 stainless steel once deformed at sub-zero temperatures. A formation of induced Martensite is clearly observed in the sub-zero specimens, while Martensite is absent in the samples worked at 25°C or higher.

Ultimately, Corrosion tests are done on the samples studied previously, highlighting a better corrosion resistance in the specimens where no induced Martensite is observed. This can be explained by the fact the Martensite has a worse corrosion resistance than its crystalline phase counterpart, which is Austenite. Austenite is the main phase of AISI 316 specifically in the "As Delivered" condition, and it remains the main phase in the sample deformed at temperatures higher than zero Celsius degrees.

The numerical model developed in LS-DYNA is then used to recreate the metal's behavior, focusing on the concentrated Stresses and their values, the possibility to study the AISI 316 stainless steel without implementing uniaxial tensile tests. The simulation was also able to recreate the True Stress-Strain graphs of the material deformed at room temperature, as well as the Load to Run Length curves which are the output of the MTS-322, load frame used for the tensile tests analyzed in this work.